Study on Resistive Switching Phenomenon in Metal Oxides for Nonvolatile Memory(Dissertation_全文)

AUTHOR(S):

Iwata, Tatsuya

Study on Resistive Switching Phenomenon in Metal Oxides for Nonvolatile Memory

February 2014

Tatsuya IWATA

Electronic Science and Engineering
Kyoto University

Abstract

Resistive random access memory (ReRAM) is a promising candidate for next-generation non-volatile memory, which can overcome the issues the current semiconductor memories are facing, such as scaling limit and speed gap in the layered structure of the present memories. ReRAM operation is based on a resistive switching (RS) phenomenon, which is reproducible and non-volatile transitions in the resistance of a cell between the low-resistance state (LRS) and the high-resistance state (HRS) by the application of voltage. In addition, an RS phenomenon is triggered by the resistance transition from the initial high-resistance state to the LRS, called the forming. An ReRAM cell (RS cell) consists of metal/oxide/metal stack structure. ReRAM has been demonstrated its promising potential such as 10×10 nm^2-cell area, sub-ns switching, and high endurance up to 10^{12} cycles. However, large variations in the RS cell characteristics including resistance (ratio) and switching voltage are one of serious problems. This is mainly because the mechanism of an RS phenomenon has not been completely understood. An RS phenomenon is qualitatively explained as the rupture and formation of conductive filaments generated inside of an oxide layer, where the forming is understood as the process of the initial formation of the filaments. Hence, the properties of the filaments play a key role in an RS phenomenon.

In this thesis, to understand the mechanism of an RS phenomenon, the properties of conductive filaments such as their physical origin and electrical properties were investigated. Influences of structural properties of nickel oxide (NiO) films on the forming characteristics, including the resistance in the initial state (R_{Ini}) and the forming voltage (V_{Form}), were also investigated to control the size and resistance of the filaments.

In Chapter 2, selection of an oxide material and an electrode material was discussed. NiO and platinum (Pt) were employed as an oxide and an electrode material, respectively. Reactive sputtering was adopted as a technique for NiO deposition. The fabrication procedure of RS cells is also described. RS cells were composed of Pt/NiO/Pt stack structure with diameters ranging from 50 to 300 μm. The thickness of NiO and Pt films was typically 100 nm.

In Chapter 3, effects of heat treatment on the RS characteristics of the RS cells were investigated. The initial state of the RS cells became equivalent to the LRS after heat treatment where significant oxygen desorption from the NiO films took place. The cells initially in the LRS is attributed to the formation of filaments from lattice defects created by the oxygen desorption, indicating that the origin of the filaments may be related to oxygen vacancies ($\mathrm{V_O}$). On the other hand, R_{Ini} significantly increased from about 3.5 kΩ to a maximum of 100 MΩ by the heat treat-

ment under which the chemical composition of NiO films was hardly changed. It was revealed that the increase in R_{Ini} is linked to the increase in the activation energy of the R_{Ini}, where the activation energy ranges from 250 to 450 meV.

In Chapter 4, direct observation and analyses of the electrical properties of conductive filaments were carried out by conductive-atomic force microscopy (C-AFM) after the removal of top electrodes (TEs). It was revealed that the variation in R_{LRS} in the range 10–220 Ω arises principally from the differences in the size and shape of filaments, where the areas of the filaments was about 10^5 nm^2 in the RS cell with R_{LRS} of 10 Ω. The resistivity of the filaments was estimated to be about 40 $\mu\Omega$cm. From the relationship between the areas of the filaments and the R_{LRS}, it was suggested that the cross-sectional areas of the filaments can vary along the thickness direction. The cross-sectional shape and chemical composition of the filaments dominating the R_{LRS} were revealed by cross-sectional transmission electron microscopy (XTEM) and energy-dispersive X-ray spectrometry (EDX). The filaments observed in this chapter consisted of reduced NiO, into which a TE material (Pt) was included owing to Joule heating induced by the current during the forming.

In Chapter 5, influences of microstructure and crystalline properties of NiO films on the R_{Ini} and the V_{Form} were investigated. Various NiO films were deposited by varying the flow rate of oxygen (O_2) during the sputtering ranging from 0.9 to 1.3 sccm. The R_{Ini} of RS cells with a diameter of 50 μm decreased by more than one order of magnitude from about 300 kΩ to 10 kΩ, when the O_2-flow rate during NiO deposition was decreased from 1.1 to 1.0 sccm, while R_{Ini} was nearly constant for the O_2-flow rate of 1.1 sccm and above. TEM observation revealed that the NiO films were composed of a number of grains with a diameter of tens of nm. Furthermore, it was revealed that Ni segregation is formed at grain boundaries (GBs) when NiO films are deposited under O_2-flow rate of 1.0 sccm or below, while NiO grains have O-rich compositions. It was demonstrated by C-AFM measurements that the Ni segregation at GBs acts as electrical leakage paths in the initial state, giving rise to the decrease in R_{Ini}. On the other hand, V_{Form} significantly varied in the range 2.2–16 V depending on the O_2-flow rate during NiO deposition, and the minimum V_{Form} of 2.2 V was obtained for O_2 flow rate of 1.1 sccm. It was revealed that the NiO films had residual compressive stress, and that the V_{Form} monotonically increased with the increase in the residual compressive stress. The V_{Form} turned out to become smaller as the amount of V_O in the NiO films in the initial state became larger from the discussion on lattice defects in the NiO films. Effects of post-deposition annealing in an argon atmosphere on the forming characteristics are also described. It was revealed that the Ni segregation was oxidized during the annealing. RS cells with such annealed NiO films exhibited forming-free behavior, probably due to the generation of a large amount of V_O by the incomplete oxidation of the Ni segregation. As a consequence, RS cells exhibiting low V_{Form} (2.2 V) and sufficiently large R_{Ini} (300 kΩ) was obtained, when NiO films deposited with O_2-flow of 1.1 sccm were used. Those RS cells exhibited R_{LRS} more than 10 kΩ, and low I_{Reset} about tens of μA. Compared with the RS cells in Chapter 3 and 4, where the V_{Form} was about 6 V, the R_{LRS} was more than two orders of magnitude larger and the I_{Reset} was more than two orders of magnitude smaller.

In Chapter 6, temperature dependences of DC and AC conduction characteristics were analyzed in the initial state, the HRS, and the LRS. The DC resistance of the RS cells in the initial state exhibited an Arrhenius-type temperature dependence with an E_a of about 330 meV above 170 K, dominated by band conduction. Below 170 K, NiO films containing large amount of V_O exhibited conduction with a low E_a of 3.1 meV, which originated from hopping conduction via acceptors of nickel vacancies (V_{Ni}) compensated by V_O. Furthermore, it was revealed that conduction in both the HRS and the LRS was dominated by the conduction of filaments. The different temperature dependence of the DC resistance between the HRS and the LRS can be ascribed to the changes in the conduction characteristics of the filaments. In conclusion, the difference in the resistance states is attributed to the difference in the conduction characteristics of the filaments, modifying the previous interpretation on the resistance change. The origin of the changes in the conduction characteristics of the filaments may be understood as the changes in the density of V_O composing them.

In Chapter 7, conclusions of this study and suggestions for future work are presented.

Acknowledgements

First, I would like to express my deepest gratitude to Professor Tsunenobu Kimoto for his supervision, continuous guidance, and kind encouragement through fruitful discussions. I would like to my hearty appreciation to Research Associate Yusuke Nishi for his continuous guidance concerning experimental details, valuable suggestions, and constructive discussions throughout this work. I would also like to thank for his maintenance management of whole experimental system.

I would like to thank Professor Shizuo Fujita for his providing the opportunity to accomplish this work and for his valuable suggestions. I acknowledge Associate Professor Itsuhiro Kakeya for his helpful advice and stimulating comments on this dissertation.

I would like to appreciate Associate Professor Jun Suda for his instructions for experimental equipments, valuable comments, constructive discussions. I am also very indebted to Emeritus Professor Hiroyuki Matsunami for his profound comments and suggestions.

I am very much obliged to Mr. Daisuke Horie, Mr. Naoki Okimoto, and Mr. Hiroki Sasakura for maintenance of sputtering system as well as experimental supports. I am grateful to Mr. Naoya Morioka for his valuable comments on Si-device process such as wafer cleaning and RIE. I am indebted to Mr. Hiroki Niwa for his kind technical support for device simulation. I wish express my appreciation to Mr. Mitsuaki Kaneko for his helpful comments and discussions on XRD and TEM measurements.

I am thankful to Mr. Shunsaku Ueta, Mr. Yuichiro Hayashi, Mr. Zhang Yibo for their continuous encouragement and support in my daily work. I am grateful to Ms. Yoriko Ohnaka, Ms. Mizuki Yamada, and Ms. Takiko Nagao for kindly supporting my daily work. I thank to all the members of Semiconductor Science and Engineering Laboratory for their kindness and support: Research Associate Masahiro Horita, Dr. Bernd Zippelius, Dr. Gan Feng, Dr. Giovanni Alfieri, Dr. Hiroki Miyake, Dr. Hironori Okumura, Dr. Hironori Yoshioka, Dr. Koutarou Kawahara, Dr. Masato Noborio, Dr. Naoki Watanabe, Dr. Nicolas Thierry-Jevali, Dr. Toshihiko Hayashi, Mr. Chihiro Kawahara, Mr. Daisuke Harata, Mr. Hajime Tanaka, Mr. Hiroaki Fujihara, Mr. Hirofumi Yamamoto, Mr. Kazuki Yamaji, Mr. Kohei Adachi, Mr. Kosuke Sato, Mr. Kyosuke Yamada, Mr. Muneharu Kato, Mr. Naoki Kaji, Mr. Ryohei Kanno, Mr. Ryosuke Kikuchi, Mr. Satoshi Asada, Mr. Seigo Mori, Mr. Seiya Nakazawa, Mr. Sho Saksaki, Mr. Shota Suzuki, Mr. Shuhei Ichikawa, Mr. Song Xiaowei, Mr. Takafumi Okuda, Mr. Takahiro Higashi, Mr. Takuma Kobayashi, Mr. Toru Hiryoshi, Mr. Yuichiro Nanen, and Mr. Youn Zeho.

This work was financially supported by the Global Center of Excellence Program (C09), the Ministry of Education, Culture, Sports, Science and Technology of Japan.

Finally, I really thank my parents, brother and all my friends for their understanding, continuing care, support and heartfelt encouragement.

February, 2014
Tatsuya Iwata

Contents

Chapter 1

Introduction

1.1 Requirement to Next-Generation Nonvolatile Memories

Today's human society is founded on the highly developed information and communication technology (ICT). By virtue of the wide spreading Internet and the development of mobile communication equipments represented by smart phones and tablet PCs, we are able to make high-speed and large-capacity communication anytime and anywhere. From now on ICT plays a more and more important role in sustainable development of our lives. Smart Town, Smart Grid, and utilizing Big Data are the examples [1]. Present ICT has been formed on the basis of remarkable development of computer technology. Toward future development of ICT, therefore, computer technology is required to further progress its performance, namely fast processing as well as large capacity of storage. Energy-saving operation should also be achieved considering today's energy problems. Memories, which are main components of computers, are not except, and requirements to the memories are becoming highly sophisticated: large capacity, fast operation, and low-power consumption.

At present, memories used for computers are static random access memory (SRAM), dynamic RAM (DRAM), Flash memory[1], and hard disk drive (HDD). The beginning of the striking development of computer technology including semiconductor memories (SRAM, DRAM and Flash memory), dates back to the invention of transistors in 1947 [2] followed by the invention of integrated circuits (ICs) in 1958 [3]. In addition to those, a turning point for semiconductor memories is the invention of DRAM in 1967 [4]. Since then, DRAM has shrunk its size under the guidance of Moore's law. Now the capacity reaches Gbit/cm^2 [5]. Another impact on memory technology is the invention of Flash memory in 1987 [6]. Flash memory has rapidly increased its capacity with the development of microfabrication technique, opening a new market as a small and light mobile storage device. Flash memory has achieved the capacity of 10 Gbit/cm^2, and has become the driver of miniaturization technology [5]. However, these memories are now approaching their scaling limit, becoming difficult to further shrink their size with ensuring performance. On the other hand, memories are divided several layers with respect to required performance, as

[1]More precisely, NAND Flash memory.

schematically shown in Fig. 1.1 [7]. In the higher layer, operation speed becomes faster, while volume becomes small. Another problem is the speed gap between each layer, which retards the performance of whole system, in particular, that between DRAM and Flash memory is a serious problem.

One potential solution of the problems concerned with the current memories is the development of a next-generation nonvolatile memory which breaks down the scaling limit and which can replace the current memory including SRAM, DRAM, and Flash memory. In particular, the replacement of volatile memories including SRAM and DRAM with nonvolatile memories is also important from a view point of normally-off computing as well as low-power consumption of computers. Therefore, various next-generation nonvolatile memories such as spin-torque-transfer magnetic RAM (STT-MRAM) [8, 9], phase change RAM (PRAM) [10–12] and resistive RAM (ReRAM), have been developed. The present performance of the current and developing memories is compared in Table 1.1. Among these nonvolatile memories, ReRAM is most suitable for high-integration and it is capable of low-current and high-speed operation. Therefore, it is the most promising candidate for replacement of DRAM and Flash memory, filling a speed gap between them. Furthermore, ReRAM has potential as an universal memory, which can replace all the present memory by a single device.

1.2 Resistive Random Access Memory (ReRAM)

1.2.1 Device structure

A basic-cell structure of ReRAM is capacitor structure where a resistive switching (RS) material is sandwiched between top electrode (TE) and bottom electrode (BE) as shown in Fig. 1.2 (a). RS materials, as the name suggests, are materials which exhibit RS phenomena, which are explained later. To date, very diverse RS materials have been reported. Most of them are metal oxides [13–15], for example, nickel oxide (NiO) [16–23], titanium dioxide (TiO_2) [24–26], hafnium dioxide (HfO_2) [27–31], $SrTiO_3$ (STO) [32], and $Pr_{1-x}Ca_xTiO_3$ (PCMO) [33]. ReRAM cells (RS cells) using a multi-layered oxide such as aluminum oxide (Al_2O_3)/HfO_2 [34, 35], and NiO/TiO_2 [36] have been also reported. Although the physical mechanism of the operation of RS cells has not been completely understood, these metal oxides can be classified into two groups based on a proposed mechanism [14]. One is binary oxides such as NiO, TiO_2, and HfO_2, where the mechanism of an RS phenomenon is based on the formation and rupture of conductive filaments, as explained later. The other is perovskite-type oxides such as STO and PCMO, where the modulation of a Schottky barrier at the interface between an electrode and an oxide may dominate an RS phenomenon [37]. Note that switching characteristics are very diverse and there are several exceptions. Although this thesis focuses on binary oxides, perovskite-type oxides are also referred in proper situations.

An electrode material most frequently used are platinum (Pt) [16–20, 22, 24, 26, 38] and titanium nitride (TiN) [29–31, 38]. In particular, TiN is used for HfO_2-based RS cells. Other

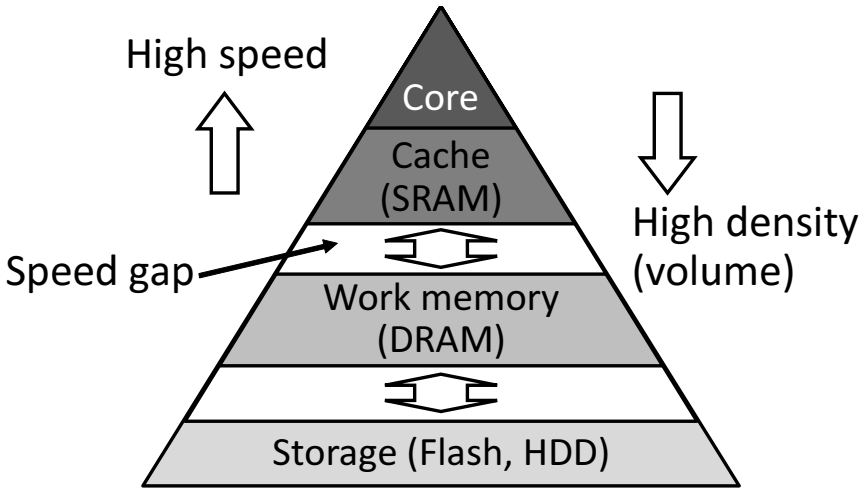

Figure 1.1: Layered structure of the current memories. [7]

Table 1.1: Comparison of properties of the current and developing memories. [5]

	SRAM	DRAM	Flash (NAND)	STT-MRAM	PRAM	ReRAM
Feature size F [nm]	45	36	22	65	45	9
Cell area	140 F^2	6 F^2	4 F^2	20 F^2	4 F^2	4 F^2
Read time	0.2 ns	<10 ns	0.1 ms	35 ns	12 ns	<50 ns
Write/Erase time	0.2 ns	<10 ns	1/0.1 ms	35 ns	100 ns	0.3 ns
Retention time	[a]	64 ms	10 y	>10 y	>10 y	>10 y
Write cycles	$> 1 \times 10^{16}$	$> 1 \times 10^{16}$	1×10^{4}	$> 1 \times 10^{12}$	1×10^{9}	1×10^{12}
Write operating voltage [V]	1	2.5	15	1.8	3	0.6/-0.2
Read operating voltage [V]	1	1.8	1.8	1.8	1.2	<0.2 V
Write Energy [J/bit]	5×10^{-16}	$> 4 \times 10^{-15}$	$> 2 \times 10^{-16}$	2.5×10^{-12}	6×10^{-12}	1×10^{-13}

[a]: Memory state is preserved as long as voltage is supplied.

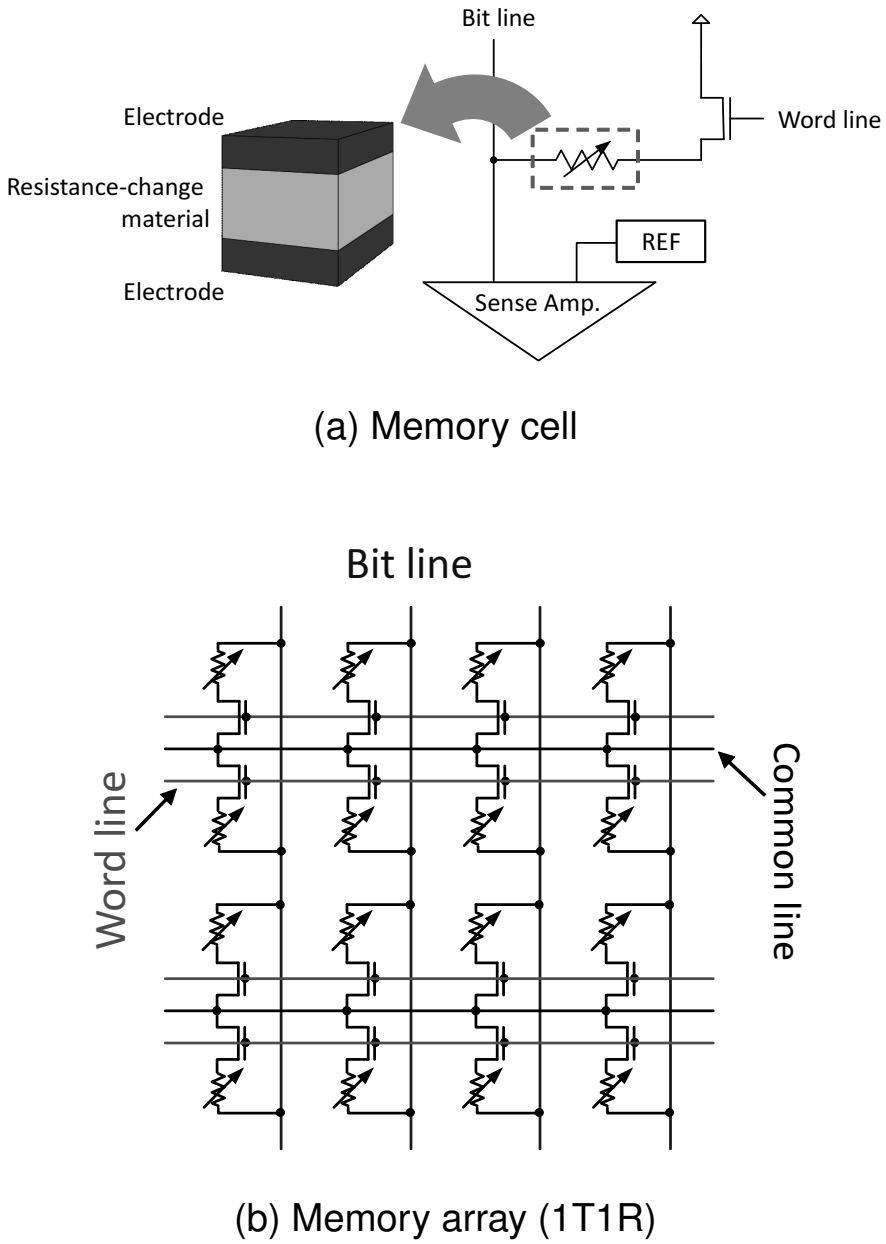

Figure 1.2: An example of (a) a memory cell and (b) a memory array of 1T1R structure. T and R indicate a select transistor and an RS cell, respectively.

materials have been also reported such as nickel (Ni) [21] and tungsten (W) [23, 39].

Several variations in the structure of an RS cell have been reported as depicted in Fig. 1.3 [15]. In addition to (a) simple capacitor-type structure, in which an oxide layer is sandwiched between a TE and a BE, Figure 1.3 represents (b) plug-type structure, (c) concave structure, and (d) cross-point-type structure. In (b)-(d), the active area is defined by the area where a TE and a BE overlap each other. The important point is that an RS phenomenon can be observed in almost every structure as long as an oxide layer is inserted between two electrodes. Furthermore, a vertical-type cell has recently been demonstrated [40, 41], which is favorable for three-dimensional integration. These simplicity and arbitrariness in the cell structure are the main advantages for high integration.

In memory arrays, several structures for selecting an RS cell have been proposed. The most basic structure is one-transistor-one-resistor (1T1R) structure as shown in Fig. 1.2 (b), where R means an RS cell. The cell size for 1T1R structure become $6-8F^2$, where F is feature size. One-diode-one-resistor (1D1R) structure is more favorable for high-integration, because it can realize $4F^2$-cell size by stacking a diode on an RS cell. For an unipolar RS cell, 1D1R structure have been demonstrated by adopting a poly-silicon (Si) diode as a cell selector [35]. Other types of select devices utilizing their nonlinear current-voltage (I–V) characteristics have been proposed [42, 43], because diodes cannot be applied to bipolar-mode RS cells, in which different bias polarities are required for switching.

1.2.2 Resistive switching (RS) phenomenon

An RS phenomenon makes the operation principle of an RS cell. Simply speaking, an RS phenomenon is reversible transitions in resistance states of an RS cell induced by the application of voltages. Typical I–V characteristics an RS cell are shown Fig. 1.4 (a). In the initial state, a RS cell generally exhibits high-resistance characteristics, which is represented by a circular symbol. When a voltage is increased, current abruptly increases at a certain voltage, as indicated by an arrow in Fig. 1.4 (a), where a transition to the low-resistance state (LRS) takes place. This initial transition to the LRS, called the "forming" process. After the forming, an RS cell exhibits repetitive resistance change between the LRS and the high-resistance state (HRS). Both in the LRS and the HRS, transitions in the resistance state take place in a similar manner to the initial state, where current abruptly changes at a certain voltage, as indicated by an arrow in Fig. 1.4 (a). The transitions from the HRS to the LRS and from the LRS to the HRS are called the "set" and the "reset" processes, respectively. Note that the forming generally requires a voltage higher than the following the set processes. Also note that currents during the forming and the set are limited by an external circuit to avoid permanent degradation of an RS cell. Figure 1.4 represents two different switching modes: (a) an unipolar and (b) a bipolar mode. An unipolar mode means both the set and reset processes occur by the same bias polarity. On the other hand, in a bipolar mode, voltages of opposite polarities are required for the set and the reset, namely, if the set processes or the forming take place by a voltage bias of positive polarity, the reset processes need a voltage bias of negative polarity. Furthermore, a switching mode in which the reset can occur by a voltage

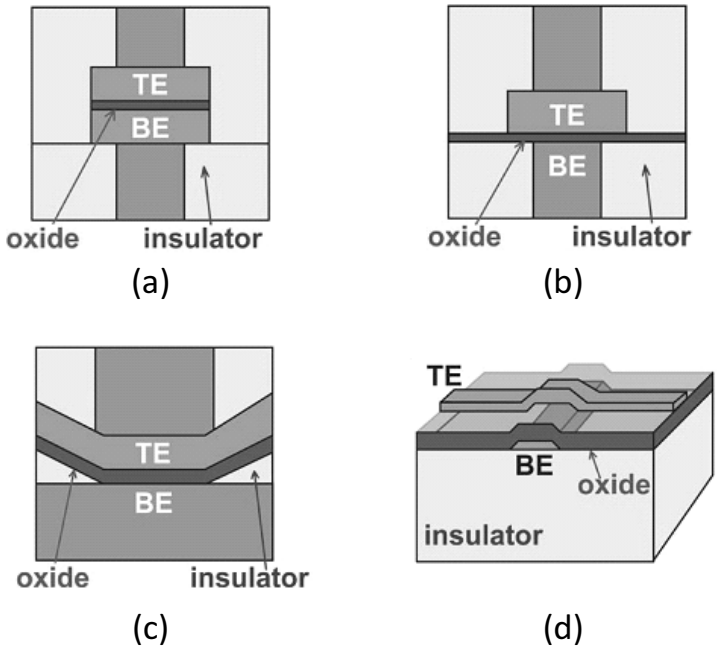

Figure 1.3: Variation of memory cell structure. (a) is basic capacitor-type structure. (b) shows the plug-type structure, (c) the concave structure. and (d) the cross-bar structure. In (b)-(d) active cell area is defined by the area overlapping a top and a bottom electrode. [15]

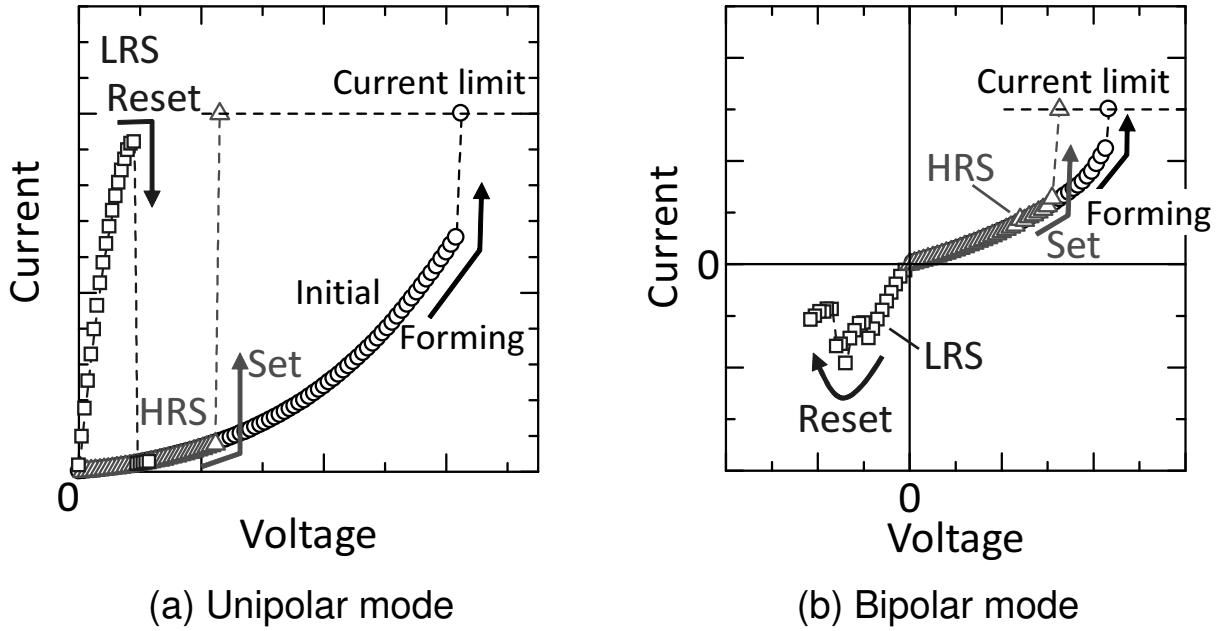

Figure 1.4: *I–V* characteristics of (a) an unipolar and (b) a bipolar switching mode. The set and reset occur by the same bias polarity in an unipolar mode, while a voltage bias of opposite polarities is required for the set and reset in a bipolar mode.

bias of both positive and negative bias polarities is often referred as a nonpolar mode.

For memory application, the difference in current between the LRS and the HRS is read out. The both resistance state is maintained even if a power supply is turned off, which enables non-volatile memory operation.

1.2.3 Current status of ReRAM

An RS phenomenon has been known for about 50 years. The first observation of an RS phenomenon dates back to the 1960s [44, 45]. The first demonstration of ReRAM using binary metal oxides was presented by Samsung in 2004 [46], which accelerated studies on ReRAM. Since then, a great deal of studies have been made, and the performance of RS cells has remarkably progressed. RS cells have rapidly shrunk their cell areas by virtue of compatibility with complementary metal-oxide-semiconductor (CMOS) process. The cell area has reached 10×10 nm^2 [47] in HfO_2-based cells and 9×9 nm^2 in WO_x-based cells [48], both of which break the scaling limit of the current memories. Although high-operation current of several mA was one of problems in RS cells in the early years, it was recently reported that operation current was reduced to 50 nA in RS cells of Al/nitrogen-doped Al_2O_3/Al [49], and to 500 nA in those of TiN/Al_2O_3/HfO_2/Hf/TiN [34]. Furthermore, switching speed of sub ns [50], and high endurance up to 10^{12} cycles [51] were reported, indicating the promising potential of ReRAM as an universal memory. Test chips of several Mbits was also demonstrated [42, 52, 53].

Despite these excellent performances, RS cells suffer from the large variation in their characteristics including resistance (ratio) and switching voltage among cells and/or switching cycles, which is one of serious problems. For example, Figure 1.5 shows the resistance distribution against switching cycles [50]. Although the data of state-of-the-art device ensures the window of resistance ratio to 10^{10} cycles, the resistance still exhibits large fluctuation among switching cycles. In addition to the variation in operation, the more serious problems are that the origin of the variation is unclear, and that a guiding principle to reduce the variation has not been established. These are mainly due to the insufficient understanding on the mechanism of an RS phenomenon, as described in the next section. Therefore, clarifying the detailed mechanism of an RS phenomenon is essential for realizing high-performance ReRAM.

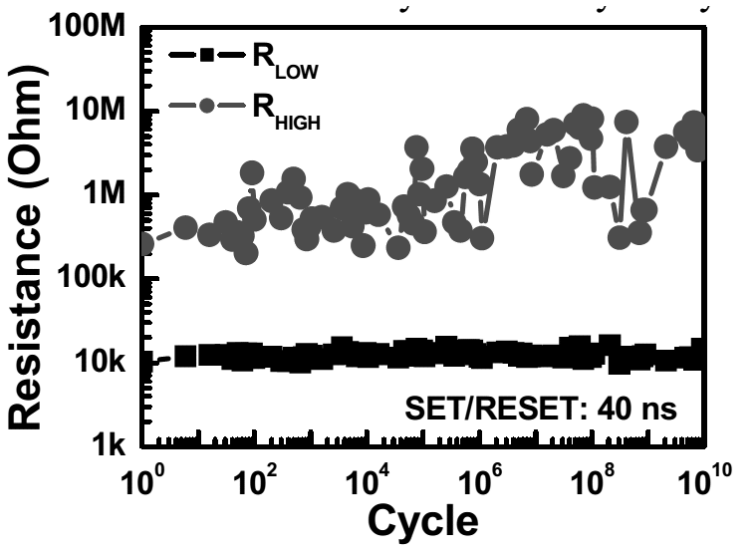

Figure 1.5: Resistance variation against switching cycles [50].

1.3 Physical Mechanism of RS Phenomenon

1.3.1 Filament Model

Now it is widely accepted that an RS phenomenon is qualitatively explained by a filament model, which was first proposed by Gibbon and Beadle [44]. In the model, conductive filaments are generated in a localized area of an RS cell by the forming, connecting a TE and a BE. Resistance switching is considered to be owing to rupture and (re-)formation of the filaments. This is schematically illustrated in Fig. 1.6. The area of filaments is much smaller than that of a RS cell. Since the resistance of the filaments is generally much smaller than that in the initial state (R_{Ini}), the resistance in the LRS (R_{LRS}) corresponds to the resistance of the filaments. On the other hand, the resistance in the HRS (R_{HRS}), in which filaments are interpreted as (partially) ruptured, frequently becomes comparable to the R_{Ini}, and thus, the resistance of the ruptured part of the filaments may be comparable to or lager than R_{Ini}. Therefore, the resistance change in an RS cell is attributed to the resistance change in localized conductive paths (filaments). The formation of filaments have been suggested by the fact that R_{LRS} is almost independent of a cell area while R_{Ini} does (the area dependence of R_{HRS} differs among reports) [19, 54]. In addition, Kinoshita *et al.* clearly proved the existence of filaments by the measurements on a separated RS cell in LRS [36]. They first set an RS cell to the LRS followed by the separation of it into two pieces, and then, measured I–V characteristics of the pieces. I–V characteristics of one piece agreed with those before separation, that is, the LRS, while the other piece was in the HRS. The origin of filaments is related to defects existing in an oxide layer [31, 55]. However, the detailed properties of the filaments including sizes, chemical composition, and electrical properties are still not fully clarified.

1.3.2 Current understanding of RS phenomenon

Forming mechanism

The forming is a generation process of filaments similar to breakdown of a dielectric, where filaments are described as the cluster of defects connecting top and bottom electrodes. The forming process completes when at least one cluster of the defects connects between both electrodes as a result of their generation. It has been pointed out that the forming process may be described by a percolation model [56]. One remarkable feature supporting the argument is that the distribution of time to forming (t_{Form}) under a constant voltage obeys Weibull distribution [57, 58]. Another feature is that that t_{Form} follows the Poisson scaling law [58] as:

$$F(t_{\mathrm{Form}}) = 1 - \exp(-\lambda A), \tag{1.1}$$

where $F(t)$ is cumulative frequency of the occurrence of the forming at time t, λ is a constant, and A is the cell area. Equation (1.1) indicates that t_{Form} decreases in cells with larger areas, indicating that the (average) defect density necessary to the forming decreases as the cell area increases.

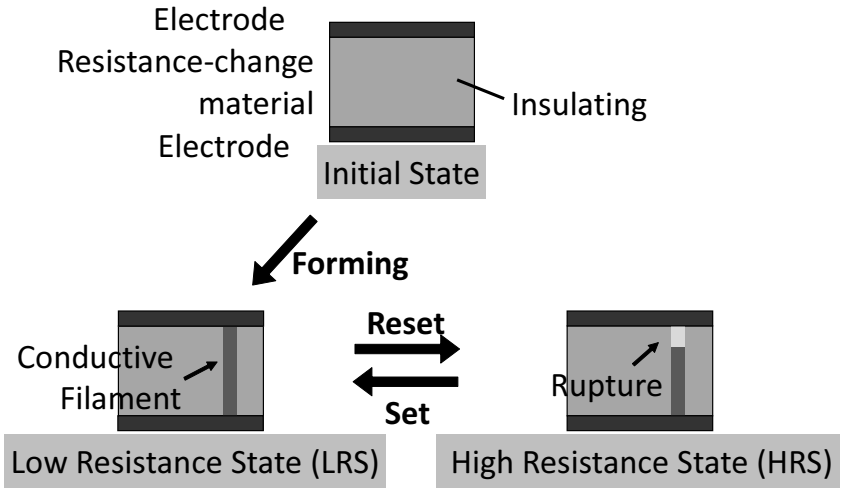

Figure 1.6: A schematic illustration of a filament model.

Mechanism of the reset and set

On the mechanism of the reset, several models have been proposed, and are diverse. In particular, the difference lies between unipolar and bipolar modes. For the unipolar mode, thermal dissolution [59] and oxidation [60] of filaments by Joule heating have been proposed. Heat simulations have shown that the temperature of filaments can be raise d to near one thousand Kelvin [61], and even above [62], which enhances the diffusion of species of filaments or oxidants. For the bipolar mode, on the other hand, the oxidation of filament by field-induced oxygen-ion migration has been proposed [63–66]. In a similar manner to the models for the unipolar mode, the migration of oxygen ions can be also enhanced by Joule heating [66]. In addition, the oxidation of the filaments responsible for the reset process occurs near the interface between an oxide material and the anode[2] [67], and it has been presumed that only a part of filaments near the anode side is oxidized (ruptured) during the reset.

Concerning the setmechanism, it has been regarded that filaments are recovered by the defect generation in a similar manner to the forming [13]. The filaments are ruptured only a thin part of their thickness during the reset, and thus, the voltage necessary to recover the filaments (the set voltage) is smaller than V_{Form}.

These model describes *measured* RS characteristics well, but cannot *predict* RS characteristics, which is essential for cell design or the optimization of cell structures. This is because these models more or less include phenomenological parameters or assumptions in, for example, the diameter and resistivity of filaments, and the diffusion coefficient of oxygen ions, due to insufficient knowledge about filaments.

Since the areas of filaments are generally small compared to the area of an RS cell, it is difficult to directly observe and characterize the properties of the filaments. In addition, the structure of filaments (size, shape and chemical composition) can change with switching cycles, among RS cells, and even with RS materials. For these reasons, understanding on the filaments is difficult, and hence, still insufficient despite the extensive studies on an RS phenomenon.

1.3.3 Key factors dominating RS characteristics

As described earlier in Section 1.3, conductive filaments play an essential role in an RS phenomenon. Resistance change originates from the change in the states of filaments, and thus, clarifying the properties of filaments, such as sizes, shapes, chemical composition, and conduction mechanism, is essential to understand the mechanism of RS phenomenon. To clarify the structural properties of filaments, cross-sectional transmission electron microscopy (TEM) observation has been conducted [68–72]. The TEM studies revealed that the microstructure of an oxide layer can be changed by resistive switching. A number of studies based on conductive-atomic force microscopy (C-AFM) have been made to identify the difference in local resistance of an

[2]For bipolar mode, an anode refers to an electrode which is positively biased for the forming and the set, and hence, negatively biased for the reset.

oxide layer [24, 56, 73–77]. It was reported that local conductive spots with a diameter of tens of nanometers appears by voltage application using a C-AFM probe [56, 73]. Nevertheless, studies that link the structural change and the local resistance have been limited [70, 71, 78]. Furthermore, studies discussing the relationship between the structural as well as electrical properties of filaments and the characteristics of an RS cell scarcely exist. Therefore, investigation of the properties on the properties of filaments and their relationship with RS-cell characteristics should be made. To investigate the properties of filaments, it is desirable that R_{LRS}, which is virtually the same as the resistance of filaments, is systematically varied. Since the forming is the process for the generation of filaments, controlling the forming characteristics such as forming voltage (V_{Form}) and R_{Ini} may be effective in controlling the resistance of filaments. Conduction mechanism of filaments is essential knowledge for nonvolatile memory application, however it is still not fully understood. Therefore, comprehensive investigation on the conduction characteristics of each resistance state including the initial state, is necessary.

1.4 Purpose and Outline of Thesis

As described above, for high-performance ReRAMs, it is essential to further understand the mechanism of an RS phenomenon, where conductive filaments play a key role. The main purpose of the study is, therefore, clarifying the properties of filaments including their microstructure, chemical composition and electrical properties.

In Chapter 2, selection of an RS material is discussed, where NiO was employed. The fabrication procedure of RS cells including the deposition method of the NiO, an electrode material, and cell structure is also described.

In Chapter 3, the origin of the filaments were investigated. It is generally difficult to identify the location of filaments because of their small areas, while filaments may be be composed of structural defects such as oxygen vacancies. Therefore, investigation was conducted from the viewpoint of chemical composition. Dominant factors in determination of the resistance in the initial state are also discussed.

In Chapter 4, direct observation of filaments is described. After the removal of a TE, exact location and area of filaments were identified by C-AFM. Cross-sectional TEM observation and energy-dispersive X-ray spectrometry (EDX) analyses revealed that the filaments were consisted of reduced NiO with inclusion of an electrode material.

In Chapter 5, to reduce V_{Form} while keeping R_{Ini} sufficiently large, influences of the structural properties of NiO films on V_{Form} and R_{Ini} were investigated. First, the substrate temperature and bottom electrodes for NiO deposition were optimized. Various NiO films were deposited by systematically varying oxygen (O_2)-flow rate during NiO deposition. The electrical and structural properties of NiO-films were characterized. It was revealed that Ni segregation was formed at grain boundaries in NiO films deposited under low O_2-flow conditions. It was demonstrated that the Ni segregation acted as leakage paths, causing the decrease in the R_{Ini}. On the other hand, it

has been found that NiO involved compressive stress, which linked to the V_{Form}. This relationship is discussed based on lattice defects. In addition, influences of post-deposition annealing on the V_{Form} are also presented. As a result of these investigations, RS cells exhibiting simultaneously low-V_{Form} and large-R_{Ini} have been obtained. R_{LRS} of the RS cells increased by more than orders of magnitude compared with those before optimization, and thus, the reset current decreased by more than two orders of magnitude.

In Chapter 6, conduction mechanism of RS cells in each resistance state was discussed from the analyses of DC and AC conduction characteristics and their temperature dependence. It was revealed that the conduction in the initial state mainly originated from hopping conduction via compensated acceptors of nickel vacancies below 170 K, while band conduction is dominant above 170 K. For LRS and HRS, it was demonstrated that the resistance change is mainly due to the change in conduction characteristics of filaments themselves rather than their rupture and formation. The difference in conduction characteristics of the filaments was discussed based on the analogy to impurity band conduction in semiconductors.

In Chapter 7, conclusions of this study and future outlook are presented.

References

[1] White paper 2013, *Information and Communications in Japan*, Ministry of Internal Affairs and Communications, Japan, `http://www.soumu.go.jp/`

[2] J. Bardeen and W. H. Brattain, US Patent 2524035 (1950).

[3] J. S. Kilby, US Patent 3138743 (1959).

[4] R. H. Dennard, US Patent 3387286 (1968).

[5] International Technology Roadmap for Semiconductor (ITRS) 2011 Edition, ITRS: `http://www.itrs.net/`

[6] F. Masuoka, Oyo Butsuri **78**, 43 (2009).

[7] H. Ohno, T. Endoh, T. Hanyu, N. Kasai, and S. Ikeda, *2010 Int. Electron Devices Meet.* (2010) p. 9.4.1.

[8] T. Kawahara, J. Appl. Phys. **109**, 07D325 (2011).

[9] T. Ohsawa, H. Koike, S. Miura, H. Honjo, K. Tokutome, S. Ikeda, T. Hanyu, H. Ohno, and T. Endoh, *2012 Symp. on VLSI Circuits* (2012) p. 46.

[10] Y. Sasago, M. Kinoshita, H. Minemura, Y. Anzai, M. Tai, K. Kurotsuchi, S. Morita, T. Takahashi, T. Takahama, T. Morimoto, T. Mine, A. Shima, and T. Kobayashi, *2011 Symp. on VLSI Technol.* (2011) p. 96.

[11] G. De Sandre, L. Bettini, A. Pirola, L. Marmonier, M. Pasotti, M. Borghi, P. Mattavelli, P. Zuliani, L. Scotti, G. Mastracchio, F. Bedeschi, R. Gastaldi, and R. Bez, IEEE J. Solid-State Circuits **46**, 52 (2011).

[12] M. Kinoshita, Y. Sasago, H. Minemura, Y. Anzai, M. Tai, Y. Fujisaki, S. Kusaba, T. Morimoto, T. Takahama, T. Mine, A. Shima, Y. Yonamoto, and T. Kobayashi, *2012 Symp. on VLSI Technol.* (2012) p. 35.

[13] H.-S. P. Wong, H.-Y. Lee, S. Yu, Y.-S. Chen, Y. Wu, P.-S. Chen, B. Lee, F. T. Chen, and M.-J. Tsai, Proc. IEEE **100**, 1951 (2012).

[14] R. Waser, R. Dittmann, G. Staikov, and K. Szot, Adv. Mater. **21**, 2632 (2009).

[15] H. Akinaga and H. Shima, Proc. IEEE **98**, 2237 (2010).

[16] S. Seo, M. J. Lee, D. H. Seo, E. J. Jeoung, D.-S. Suh, Y. S. Joung, I. K. Yoo, I. R. Hwang, S. H. Kim, and I. S. Byun, J.-S. Kim, J. S. Choi, and B. H. Park, Appl. Phys. Lett. **85**, 5655 (2004).

[17] J.-W. Park, J.-W. Park, K. Jung, M. K. Yang, and J.-K. Lee, J. Vac. Sci. Technol. B **24**, 2205 (2006).

[18] K. Tsunoda, K. Kinoshita, Y. Yamazaki, T. Izuka, Y. Ito, A. Takahashi, A. Okano, Y. Sato, T. Fukano, M. Aoki, and Y. Sugiyama, *2007 IEEE Int. Electron Devices Meet.* (2007) p. 767.

[19] H. Shima, F. Takano, H. Akinaga, Y. Tamai, I. H. Inoue, and H. Takagi, Appl. Phys. Lett. **91**, 012901 (2007).

[20] U. Russo, D. Ielmini, C. Cagli, and A. L. Lacaita, IEEE Trans. Electron Devices **56**, 186 (2009).

[21] L. Goux, J. G. Lisoni, X. P. Wang, M. Jurczak, and D. J. Wouters, IEEE Trans. Electron Devices **56**, 2363 (2009).

[22] H. D. Lee and Y. Nishi, Appl. Phys. Lett. **97**, 252107 (2010).

[23] C. Kügeler, R. Weng, H. Schroeder, R. Symanczyk, P. Majewski, K.-D. Ufert, R. Waser, and M. Kund, Thin Solid Films **518**, 2258 (2010).

[24] B. J. Choi, D. S. Jeong, S. K. Kim, C. Rohde, S. Choi, J. H. Oh, H. J. Kim, C. S. Hwang, K. Szot, R. Waser, B. Reichenberg, and S. Tiedke, J. Appl. Phys. **98**, 033715 (2005).

[25] K. Tsunoda, Y. Fukuzumi, J. R. Jameson, Z. Wang, P. B. Griffin, and Y. Nishi, Appl. Phys. Lett. **90**, 113501 (2007).

[26] W. Wang, S. Fujita, and S. S. Wong, IEEE Electron Device Lett. **30**, 763 (2009).

[27] Y.-S. Chen, H.-Y. Lee, P.-S. Chen, T.-Y. Wu, C.-C. Wang, P.-J. Tzeng, F. Chen, M.-J. Tsai, and C. Lien, IEEE Electron Device Lett. **31**, 1473 (2010).

[28] L. Goux, P. Czarnecki, Y. Y. Chen, L. Pantisano, X. P. Wang, R. Degraeve, B. Govoreanu, M. Jurczak, D. J. Wouters, and L. Altimime, Appl. Phys. Lett. **97**, 243509 (2010).

[29] G. Bersuker, D. C. Gilmer, D. Veksler, P. Kirsch, L. Vandelli, A. Padovani, L. Larcher, K. McKenna, A. Shluger, V. Iglesias, M. Porti, and M. Nafria, J. Appl. Phys. **110**, 124518 (2011).

[30] C. Walczyk, D. Walczyk, T. Schroeder, T. Bertaud, M. Sowinska, M. Lukosius, M. Fraschke, D. Wolansky, B. Tillack, E. Miranda, and C. Wenger, IEEE Trans. Electron Devices **58**, 3124 (2011).

[31] S. Yu, X. Guan, and H.-S. P. Wong, Appl. Phys. Lett. **99**, 063507 (2011).

[32] K. Szot, W. Speier, G. Bihlmayer, and R. Waser, Nature Mater. **5**, 312 (2006).

[33] S. Q. Liu, N. J. Wu, and A. Ignatiev, Appl. Phys. Lett. **76**, 2749 (2000).

[34] L. Goux, A. Fantini, G. Kar, Y.-Y. Chen, N. Jossart, R. Degraeve, S. Clima, B. Govoreanu, G. Lorenzo, G. Pourtois, D. J. Wouters, J. A. Kittl, L. Altimime, and M. Jurczak, *2012 Symp. on VLSI Technol.* (2012) p. 159.

[35] X. A. Tran, B. Gao, J. F. Kang, L. Wu, Z. R. Wang, Z. Fang, K. L. Pey, Y. C. Yeo, A. Y. Du, B. Y. Nguyen, M. F. Li, and H. Y. Yu, *2011 Symp. on VLSI Technol.* (2011) p. 44.

[36] K. Kinoshita, T. Tamura, M. Aoki, Y. Sugiyama, and H. Tanaka, Jpn. J. Appl. Phys. **45**, L991 (2006).

[37] A. Sawa, Materials Today **11**, 28 (2008).

[38] L. Goux, X. P. Wang, Y. Y. Chen, L. Pantisano, N. Jossart, B. Govoreanu, J. A. Kittl, M. Jurczak, L. Altimime, and D. J. Wouters, Electrochem. Solid-State Lett. **14**, H244 (2011).

[39] A. Demolliens, C. Muller, D. Deleruyelle, S. Spiga, E. Cianci, M. Fanciulli, F. Nardi, C. Cagli, and D. Ielmini, *2009 IEEE Int. Memory Workshop* (2009) DOI: 10.1109/IMW.2009.5090606.

[40] I. G. Baek, C. J. Park, H. Ju, D. J. Seong, H. S. Ahn, J. H. Kim, M. K. Yang, S. H. Song, E. M. Kim, S. O. Park, C. H. Park, C. W. Song, G. T. Jeong, S. Choi, H. K. Kang, and C. Chung, *2011 Int. Electron Devices Meet.* (2011) p. 31.8.1.

[41] S. Yu, H.-Y. Chen, B. Gao, J. Kang, and H.-S. P. Wong, ACS Nano **7**, 2320 (2013).

[42] A. Kawahara, R. Azuma, Y. Ikeda, K. Kawai, Y. Katoh, K. Tanabe, T. Nakamura, Y. Sumimoto, N. Yamada, N. Nakai, S. Sakamoto, Y. Hayakawa, K. Tsuji, S. Yoneda, A. Himeno, K. Origasa, K. Shimakawa, T. Takagi, T. Mikawa, and K. Aono, *2012 IEEE Int. Solid-State Circuits Conf.* (2012) p. 432.

[43] J. J. Yang, M.-X. Zhang, M. D. Pickett, F. Miao, J. P. Strachan, W. Li, W. Yi, D. A. A. Ohlberg, B. J. Choi, W. Wu, J. H. Nickel, G. Medeiros-Ribeiro, and R. S. Williams, Appl. Phys. Lett. **100**, 113501 (2012).

[44] J. F. Gibbons and W. E. Beadle, Solid-State Electron. **7**, 785 (1964).

[45] G. Dearnaley, A. M. Stoneham, and D. V. Morgan, Rep. Prog. Phys. **33**, 1129 (1970).

[46] I. G. G. Baek, M. S. M. J. J. S. Lee, S. Seo, D. H. H. Seo, D.-S. Suh, J. C. C. Park, S. O. O. Park, H. S. S. Kim, I. K. K. Yoo, S. Sco, U.-I. Chung, and J. T. Moon, *Tech. Dig. of 2004 IEEE Int. Electron Devices Meet.* (2004) p. 587.

[47] B. Govoreanu, G. S. Kar, Y.-Y. Chen, V. Paraschiv, S. Kubicek, A. Fantini, I. P. Radu, L. Goux, S. Clima, R. Degraeve, N. Jossart, O. Richard, T. Vandeweyer, K. Seo, P. Hendrickx, G. Pourtois, H. Bender, L. Altimime, D. J. Wouters, J. A. Kittl, and M. Jurczak, *2011 Int. Electron Devices Meet.* (2011) p. 31.6.1.

[48] C.H. Ho, C.-L. Hsu, C.-C. Chen, J.-T. Liu, C.-S. Wu, C.-C. Huang, C. Hu, and F.-L Yang, *2010 Int. Electron Devices Meet.* (2010) p. 19.1.1.

[49] W. Kim, S. I. Park, Z. Zhang, Y. Yang-Liauw, D. Sekar, H.-S. P. Wong, and S. S. Wong, *2011 Symp. on VLSI Technol.* (2011) p. 22.

[50] H. Y. Lee, Y. S. Chen, P. S. Chen, P. Y. Gu, Y. Y. Hsu, S. M. Wang, W. H. Liu, C. H. Tsai, S. S. Sheu, P. C. Chiang, W. P. Lin, C. H. Lin, W. S. Chen, F. T. Chen, C. H. Lien, and M.-J. Tsai, *2010 Int. Electron Devices Meet.* (2010) p. 19.7.1.

[51] M.-J. Lee, C. B. Lee, D. Lee, S. R. Lee, M. Chang, J. H. Hur, Y.-B Kim, C.-J Kim, D. H. Seo, S. Seo, U.-I. Chung, I.-K. Yoo, and K. Kim, Nature Materials **10**, 625 (2011).

[52] S.-S. Sheu, M.-F. Chang, K.-F. Lin, C.-W. Wu, Y.-S. Chen, P.-F. Chiu, C.-C. Kuo, Y.-S. Yang, P.-C. Chiang, W.-P. Lin, C.-H. Lin, H.-Y. Lee, P.-Y. Gu, S.-M. Wang, F. T. Chen, K.-L. Su, C.-H. Lien, K.-H. Cheng, H.-T. Wu, T.-K. Ku, M.-J. Kao, and M.-J. Tsai, *2011 IEEE Int. Solid-State Circuits Conf.* (2011) p. 200.

[53] H. D. Lee, S. G. Kim, K. Cho, H. Hwang, H. Choi, J. Lee, S. H. Lee, H. J. Lee, J. Suh, S.-O. Chung, Y. S. Kim, K. S. Kim, W. S. Nam, J. T. Cheong, J. T. Kim, S. Chae, E.-R. Hwang, S. N. Park, Y. S. Sohn, C. G. Lee, H. S. Shin, K. J. Lee, K. Hong, H. G. Jeong, K. M. Rho, Y. K. Kim, S. Chung, J. Nickel, J. J. Yang, H. S. Cho, F. Perner, R. S. Williams, J. H. Lee, S. K. Park, and S.-J. Hong, *2012 Symp. on VLSI Technol.* (2012) p. 151.

[54] S. Seo, M. J. Lee, D. H. Seo, S. K. Choi, D.-S. Suh, Y. S. Joung, I. K. Yoo, I. S. Byun, I. R. Hwang, S. H. Kim, and B. H. Park, Appl. Phys. Lett. **86**, 093509 (2005).

[55] D. Ielmini, F. Nardi, and C. Cagli, Appl. Phys. Lett. **96**, 053503 (2010).

[56] S. C. Chae, J. S. Lee, S. Kim, S. B. Lee, S. H. Chang, C. Liu, B. Kahng, H. Shin, D.-W. Kim, C. U. Jung, S. Seo, M.-J. Lee, and T. W. Noh, Adv. Mater. **20**, 1154 (2008).

[57] G. Buh, I. Hwang, and B. H. Park, Appl. Phys. Lett. **95**, 142101 (2009).

[58] Y. Nishi, T. Iwata, D. Horie, and T. Kimoto, *Mater. Res. Soc. Symp. Proc.* **1430** (2012) DOI: 10.1557/opl.2012.1023.

[59] U. Russo, D. Ielmini, C. Cagli, and A. L. Lacaita, IEEE Trans. Electron Devices **56**, 193 (2009).

[60] Y. Sato, K. Kinoshita, M. Aoki, and Y. Sugiyama, Appl. Phys. Lett. **90**, 033503 (2007).

[61] S. H. Chang, S. C. Chae, S. B. Lee, C. Liu, T. W. Noh, J. S. Lee, B. Kahng, J. H. Jang, M. Y. Kim, D.-W. Kim, and C. U. Jung, Appl. Phys. Lett. **92**, 183507 (2008).

[62] C. Hermes, M. Wimmer, S. Menzel, K. Fleck, G. Bruns, M. Salinga, U. Böttger, R. Bruchhaus, T. Schmitz-Kempen, M. Wuttig, and R. Waser, IEEE Electron Device Lett. **32**, 1116 (2011).

[63] B. Gao, B. Sun, H. Zhang, L. Liu, X. Liu, R. Han, J. Kang, and B. Yu, IEEE Electron Device Lett. **30**, 1326 (2009).

[64] S. Yu and H.-S. P. Wong, IEEE Electron Device Lett. **31**, 1455 (2010).

[65] X. Guan, S. Yu, and H.-S. P. Wong, IEEE Trans. Electron Devices **59**, 1172 (2012).

[66] S. Larentis, F. Nardi, S. Balatti, D. C. Gilmer, and D. Ielmini, IEEE Trans. Electron Devices **59**, 2468 (2012).

[67] K. Kinoshita, T. Tamura, M. Aoki, Y. Sugiyama, and H. Tanaka, Appl. Phys. Lett. **89**, 103509 (2006).

[68] G.-S. Park, X.-S. Li, D.-C. Kim, R.-J. Jung, M.-J. Lee, and S. Seo, Appl. Phys. Lett. **91**, 222103 (2007).

[69] J. P. Strachan, M. D. Pickett, J. J. Yang, S. Aloni, A. L. D. Kilcoyne, G. Medeiros-Ribeiro, and R. S. Williams, Adv. Mater. **22**, 3573 (2010).

[70] F. Miao, J. P. Strachan, J. J. Yang, M. Zhang, I. Goldfarb, A. C. Torrezan, P. Eschbach, R. D. Kelley, G. Medeiros-Ribeiro, and R. S. Williams, Adv. Mater. **23**, 5633 (2011).

[71] Z. Wei, T. Takagi, Y. Kanzawa, Y. Katoh, T. Ninomiya, K. Kawai, S. Muraoka, S. Mitani, K. Katayama, S. Fujii, R. Miyanaga, Y. Kawashima, T. Mikawa, K. Shimakawa, and K. Aono, *2011 IEEE Int. Electron Devices Meet.* (2011) p. 31.4.1.

[72] H. Kondo, M. Arita, T. Fujii, H. Kaji, M. Moniwa, T. Yamaguchi, I. Fujiwara, M. Yoshimaru, and Y. Takahashi, Jpn. J. Appl. Phys. **50**, 081101 (2011).

[73] J.-B. Yun, S. Kim, S. Seo, M.-J. Lee, D.-C. Kim, S.-E. Ahn, Y. Park, J. Kim, and H. Shin, Phys. Status Solidi (RRL) **1**, 280 (2007).

[74] R. Münstermann, J. J. Yang, J. P. Strachan, G. Medeiros-Ribeiro, R. Dittmann, and R. Waser, Phys. Status Solidi (RRL) **4**, 16 (2010).

[75] F. Nardi, D. Deleruyelle, S. Spiga, C. Muller, B. Bouteille, and D. Ielmini, J. Appl. Phys. **112**, 064310 (2012).

[76] D. Deleruyelle, C. Dumas, M. Carmona, C. Muller, S. Spiga, and M. Fanciulli, Appl. Phys. Express **4**, 051101 (2011).

[77] J. Y. Son and Y.-H. Shin, Appl. Phys. Lett. **92**, 222106 (2008).

[78] D.-H. Kwon, K. M. Kim, J. H. Jang, J. M. Jeon, M. H. Lee, G. H. Kim, X.-S. Li, G. Park, B. Lee, S. Han, M. Kim, and C. S. Hwang, Nature Nanotechnology **5**, 148 (2010).

Chapter 2

Materials for Resistive Switching Cells and Their Fabrication

2.1 Introduction

Various materials have been reported to exhibit a resistive switching (RS) phenomenon. Since it is still controversial what material is the most promising for high-performance resistive random access memories (ReRAMs), the selection of an RS material is an important problem for fabricating RS cells.

RS characteristics are influenced by not only the difference in an RS material, but also the condition for its deposition [1]. Furthermore, an electrode material even influences on the RS characteristics [2–5]. Therefore, the selections of a deposition method for the RS material and an electrode material are also important for the fabrication of RS cells.

In this chapter, the selection of an RS material is discussed. The deposition method for the RS material, the selection of an electrode material, and the RS cell fabrication procedure are also presented.

2.2 Selection of an RS Material

Various kinds of oxides have been reported as an RS material, for example, nickel oxide (NiO) [6–12], titanium dioxide (TiO_2) [13–15], hafnium dioxide (HfO_2) [16–20], tantalum oxide (TaO_x) [21–23], aluminum oxide (Al_2O_3) [24, 25], and others [26–29]. However, as described in 2.1, a guiding principle for the selection of an RS material has not yet been established because of the insufficient understanding of the mechanism of an RS phenomenon. Taking it into consideration that the main goal of this study is to understand the mechanism of an RS phenomenon, a criterion for the selection of an RS material was:

- An oxide whose RS characteristics and physical properties have been extensively studied,

because the existence of abundant data is helpful in interpreting new experimental data, leading to comprehensive understanding on an RS phenomenon. In addition, concerning a practical use, the following conditions were also taken into consideration:

- A metal element composing an oxide exists in abundance among RS materials.
- An oxide which can be deposited at a low temperature enough to be embedded to the back-end of complementary metal-oxide-semiconductor (CMOS) process.

In consequence, NiO was adopted as an RS material satisfying these criteria in this study.

Overview of NiO and its deposition technique

NiO is a well-known anti-ferromagnetic material [30], having sodium chloride (NaCl) type structure with a lattice constant of 4.177Å [31]. The crystalline structure of NiO is shown in Fig. 2.1[1]. Its insulating origin had been a main target of interest, and, it has been now widely accepted that NiO is a charge-transfer-type insulator [33, 34]. Although a perfect crystalline NiO is an insulator, it exhibits *p*-type conductivity by introducing lithium substitutionals or nickel vacancies [35]. A number of studies on the electrical properties of NiO have been made [35–39]. The RS characteristics of NiO have been also extensively studied since its RS phenomenon was first reported in 1967 [40].

NiO films are prepared by various methods, such as electron beam (EB) evaporation [41], sputtering [6–9, 12], pulsed-laser deposition [42], thermal oxidation [11, 43], and atomic-layer deposition [44]. In this study, sputtering was employed for the deposition of NiO films because it is a most simple and widely used method. In addition, when NiO films are deposited using a Ni target and an oxygen (O_2) as a reactive gas together with argon (Ar), which is known as reactive sputtering, it is possible to systematically alter the properties of the NiO films such as chemical composition, by controlling the O_2 amount in the process gas during sputtering [7, 45]. Reactive sputtering is, therefore, suitable for the investigation of the influences of the film properties on their RS characteristics, and was adopted in this study.

2.3 Fabrication of RS Cells

2.3.1 Sputtering system for NiO-film deposition

A sputtering system used for NiO deposition (ANELVA L-250-FHL) is composed of a pair of electrodes as schematically shown in Fig. 2.2. The sputtering system has three planer magnetron cathodes with a diameter of 2 inches for targets facing with a substrate holder (an anode). An rf power supply (frequency: 13.56 MHz) is used for plasma discharge. The substrate holder can be heated up to 600°C. The vacuum chambers consist of a sputtering (SP) chamber and a load-lock (LL) chamber, thus, it is possible to exchange a specimen without exposing the SP chamber to the

[1]The crystalline structure was drawn by VESTA [32]

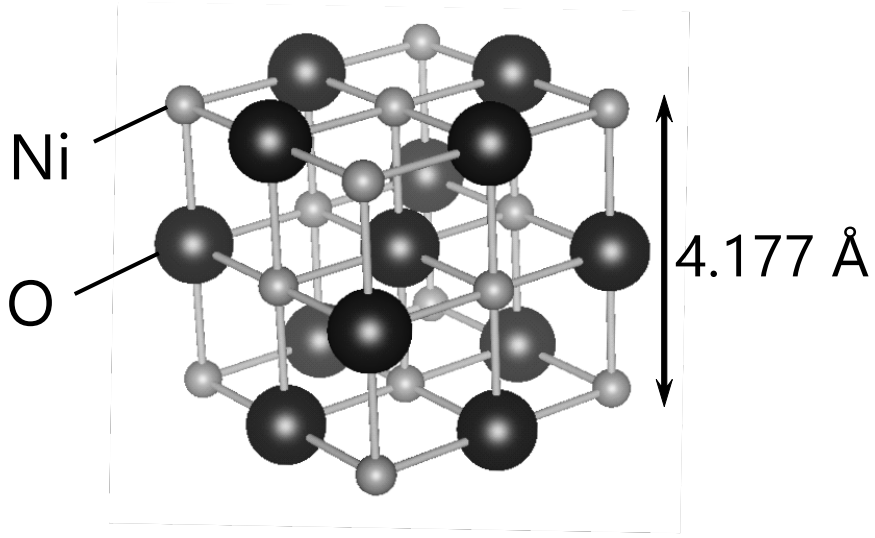

Figure 2.1: Crystalline structure of NiO.

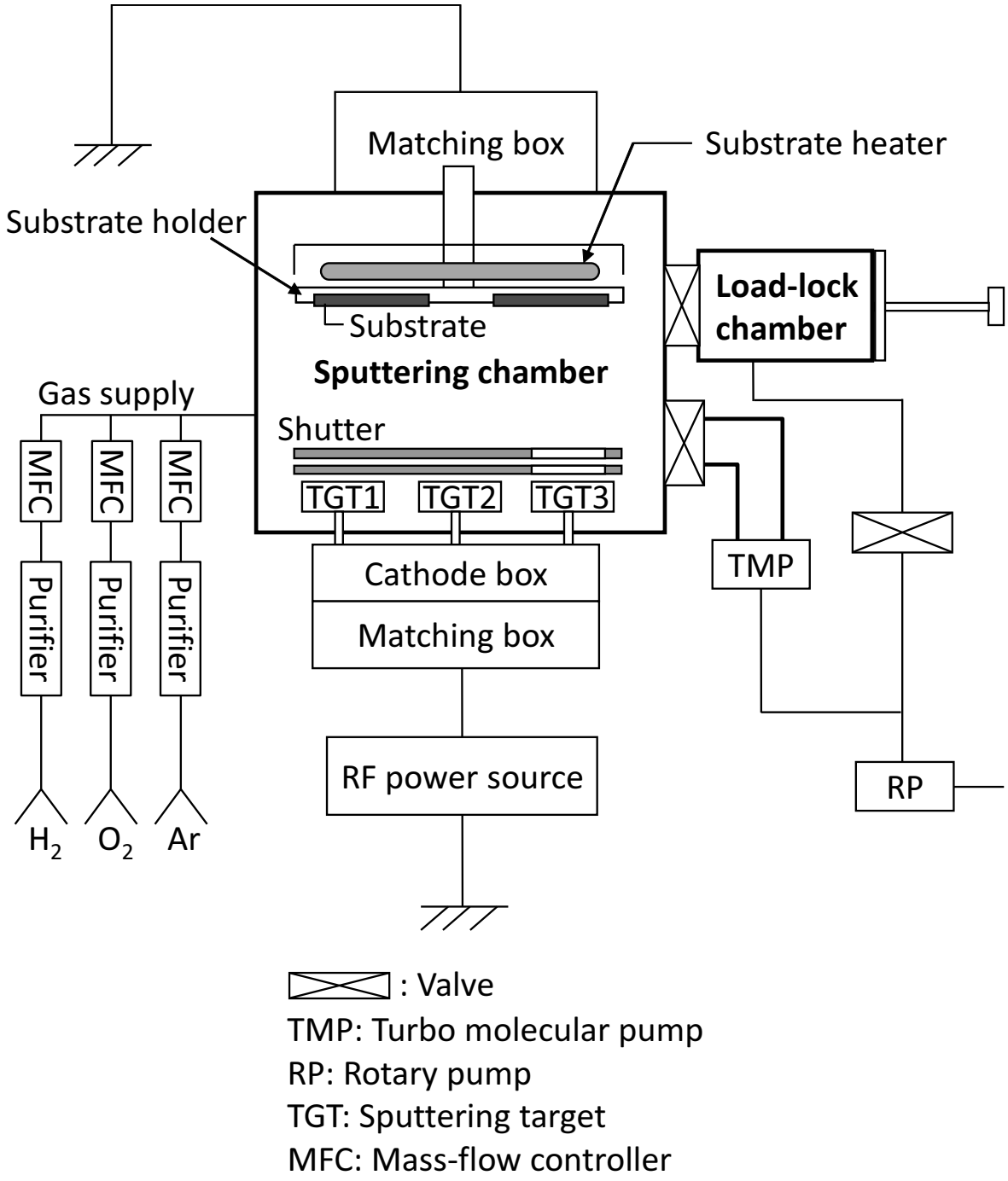

Figure 2.2: A schematic illustration of the sputtering system for NiO deposition.

air. The SP chamber is pumped by a turbo molecular pump (TMP) with the assistance of a rotary pump (RP). The RP is also used for the pumping for the LL chamber. Background pressure of the SP chamber can reach 5×10^{-5} Pa without heating the substrate. The sputtering system are equipped three kinds of gas supplies: Ar, O_2, and hydrogen (H_2). The gases are introduced to the SP chamber through a purifier, and their flow rate is controlled by a mass-flow controller (MFC). For NiO deposition, a Ni target (99.99% purity) and a mixture of Ar and O_2 as a process gas were used.

2.3.2 Electrode material

In a similar manner to RS materials, diverse electrode materials for RS cells have been reported, for example, platinum (Pt) [4, 6–10, 12, 13, 15], titanium nitride (TiN) [4, 18–20], and tungsten (W) [46, 47]. For the selection of an electrode material, it should be taken into account that electrode materials can be oxidized during NiO deposition [48]. RS characteristics may be affected by the oxidation of the electrode material, and thereby the RS characteristics intrinsic to NiO may be blurred. Therefore, Pt, which is a highly oxidation-resistant material, was adopted as an electrode material. Pt is the most frequently used material as electrodes for NiO-based RS cells, because stable RS characteristics have been reported in those with Pt electrodes.

2.3.3 Cell structure

The structure of an RS cell is composed of a Pt/NiO/Pt stack. The cross section of an RS cell is schematically illustrated in Fig. 2.3. A procedure for RS-cell fabrication is as follows. As a bottom electrode (BE), 100 nm-thick Pt was deposited on the entire area of a substrate. After the deposition of a BE, a NiO film was deposited on it. Various NiO-films were deposited by varying the O_2-flow rate and the substrate temperature during the deposition, while the total gas pressure was kept at 0.6 Pa throughout this study. The details of the condition for NiO deposition are explained in every chapter. The thickness of the NiO films was typically 100 nm. Finally, Pt was deposited using an EB-evaporation system (ANELVA L-043E) through a shadow mask to form circular-shaped top electrodes (TEs) with diameters ranging from 50 to 300 μm. Since a BE was deposited on the entire area of a substrate, the areas of RS cells are defined by the areas of TEs. The thickness of TEs was typically 100 nm. An optical microscopy image of a sample chip is shown in Fig. 2.4, where a number of TEs with different diameters are formed on a NiO layer. Substrates employed in this study were either silicon (Si) wafers or Si wafers covered with a 200 nm-thick thermal oxide (SiO_2/Si). BEs were deposited by either EB evaporation or sputtering. Since the substrate and the method for BE deposition have been improved during this study, they are explained in every chapter.

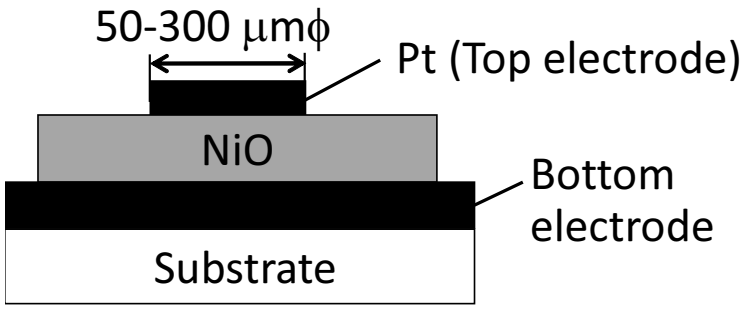

Figure 2.3: A schematic illustration of the cross section of a sample.

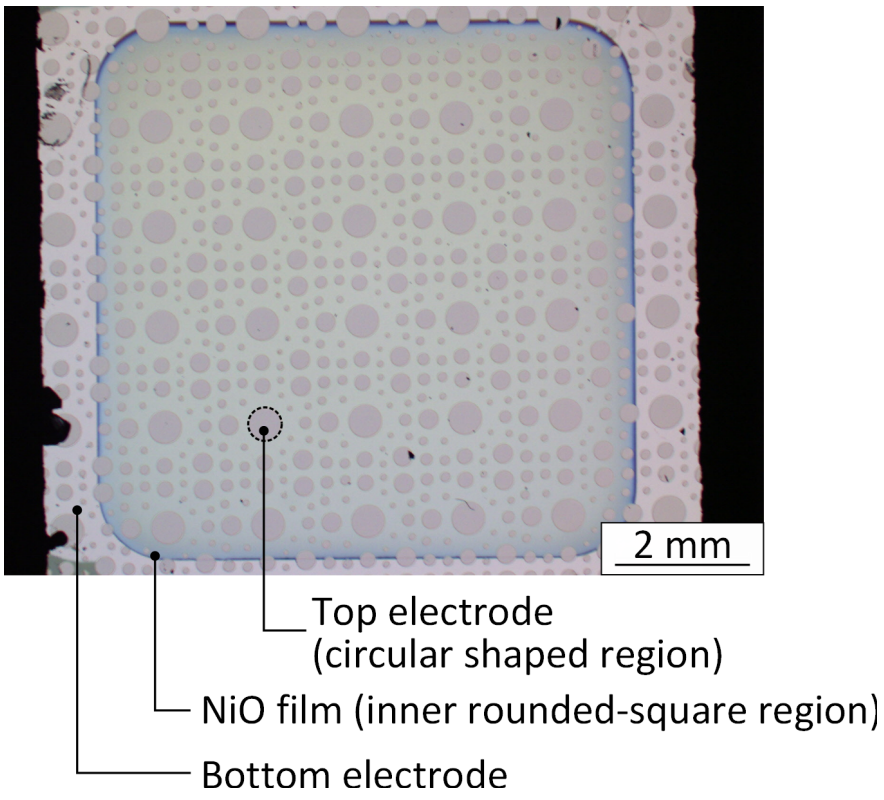

Figure 2.4: An optical microscopy image of a sample chip. A bottom electrode is on the entire area of the substrate, and is exposed to the air near the edges of the chip. The inner squared region with round corners is a NiO layer. A number of circular-shaped top electrodes with various diameters are formed in the chip.

2.4 Typical RS characteristics

Typical current-voltage (I–V) characteristics of an RS cell with a diameter of 100 μm are shown in Fig. 2.5. Resistance in the initial state (R_{Ini}) was about 6 kΩ at a voltage bias of 0.1 V. The forming, set, and reset occurred at about 6 V, 1 V and 2 V, respectively. Resistance in the low-resistance state (R_{LRS}) and current for the reset are about 60 Ω and 9 mA, respectively, while resistance in the high-resistance state was comparable to the R_{Ini}.

2.5 Summary

The selection of RS material was discussed, and the fabrication procedure of RS cells was described. As an RS material, NiO has been adopted from the following reasons that: (1) it is suitable for elucidating the mechanism of an RS phenomenon because of plentiful previous studies, (2) Ni exists relatively abundantly compared with other metals for RS materials, and (3) the deposition of NiO is compatible with the CMOS process. Reactive sputtering has been adopted for NiO deposition. On the other hand, Pt was adopted as an electrode material, because Pt is a highly oxidation-resistant material and because stable RS characteristics have been reported in NiO-based RS cells with Pt electrode. RS cells in this study consist of a Pt/NiO/Pt stack structure, the diameters of which ranged from 50 to 300 μm. The thickness of NiO films, BEs, and TEs was typically 100 nm.

References

[1] R. Jung, M.-J. Lee, S. Seo, D. C. Kim, G.-S. Park, K. Kim, S. Ahn, Y. Park, I.-K. Yoo, J. Kim, and B. H. Park, Appl. Phys. Lett. **91**, 022112 (2007).

[2] S. Seo, M. J. Lee, D. C. Kim, S. E. Ahn, B.-H. Park, Y. S. Kim, I. K. Yoo, I. S. Byun, I. R. Hwang, S. H. Kim, J.-S. Kim, J. S. Choi, J. H. Lee, S. H. Jeon, S. H. Hong, and B. H. Park, Appl. Phys. Lett. **87**, 263507 (2005).

[3] D. C. Kim, M. J. Lee, S. E. Ahn, S. Seo, J. C. Park, I. K. Yoo, I. G. Baek, H. J. Kim, E. K. Yim, J. E. Lee, S. O. Park, H. S. Kim, U.-I. Chung, J. T. Moon, and B. I. Ryu, Appl. Phys. Lett. **88**, 232106 (2006).

[4] L. Goux, X. P. Wang, Y. Y. Chen, L. Pantisano, N. Jossart, B. Govoreanu, J. A. Kittl, M. Jurczak, L. Altimime, and D. J. Wouters, Electrochem. Solid-State Lett. **14**, H244 (2011).

[5] C. B. Lee, B. S. Kang, A. Benayad, M. J. Lee, S.-E. Ahn, K. H. Kim, G. Stefanovich, Y. Park, and I. K. Yoo, Appl. Phys. Lett. **93**, 042115 (2008).

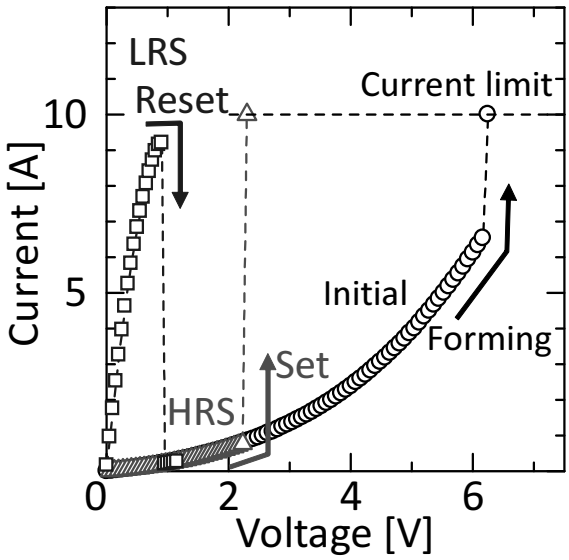

Figure 2.5: Typical *I*–*V* characteristics of an RS cell.

[6] S. Seo, M. J. Lee, D. H. Seo, E. J. Jeoung, D.-S. Suh, Y. S. Joung, I. K. Yoo, I. R. Hwang, S. H. Kim, and I. S. Byun, J.-S. Kim, J. S. Choi, and B. H. Park, Appl. Phys. Lett. **85**, 5655 (2004).

[7] J.-W. Park, J.-W. Park, K. Jung, M. K. Yang, and J.-K. Lee, J. Vac. Sci. Technol. B **24**, 2205 (2006).

[8] K. Tsunoda, K. Kinoshita, Y. Yamazaki, T. Izuka, Y. Ito, A. Takahashi, A. Okano, Y. Sato, T. Fukano, M. Aoki, and Y. Sugiyama, *2007 IEEE Int. Electron Devices Meet.* (2007) p. 767.

[9] H. Shima, F. Takano, H. Akinaga, Y. Tamai, I. H. Inoue, and H. Takagi, Appl. Phys. Lett. **91**, 012901 (2007).

[10] U. Russo, D. Ielmini, C. Cagli, and A. L. Lacaita, IEEE Trans. Electron Devices **56**, 186 (2009).

[11] L. Goux, J. G. Lisoni, X. P. Wang, M. Jurczak, and D. J. Wouters, IEEE Trans. Electron Devices **56**, 2363 (2009).

[12] H. D. Lee and Y. Nishi, Appl. Phys. Lett. **97**, 252107 (2010).

[13] B. J. Choi, D. S. Jeong, S. K. Kim, C. Rohde, S. Choi, J. H. Oh, H. J. Kim, C. S. Hwang, K. Szot, R. Waser, B. Reichenberg, and S. Tiedke, J. Appl. Phys. **98**, 033715 (2005).

[14] K. Tsunoda, Y. Fukuzumi, J. R. Jameson, Z. Wang, P. B. Griffin, and Y. Nishi, Appl. Phys. Lett. **90**, 113501 (2007).

[15] W. Wang, S. Fujita, and S. S. Wong, IEEE Electron Device Lett. **30**, 763 (2009).

[16] Y.-S. Chen, H.-Y. Lee, P.-S. Chen, T.-Y. Wu, C.-C. Wang, P.-J. Tzeng, F. Chen, M.-J. Tsai, and C. Lien, IEEE Electron Device Lett. **31**, 1473 (2010).

[17] L. Goux, P. Czarnecki, Y. Y. Chen, L. Pantisano, X. P. Wang, R. Degraeve, B. Govoreanu, M. Jurczak, D. J. Wouters, and L. Altimime, Appl. Phys. Lett. **97**, 243509 (2010).

[18] G. Bersuker, D. C. Gilmer, D. Veksler, P. Kirsch, L. Vandelli, A. Padovani, L. Larcher, K. McKenna, A. Shluger, V. Iglesias, M. Porti, and M. Nafria, J. Appl. Phys. **110**, 124518 (2011).

[19] C. Walczyk, D. Walczyk, T. Schroeder, T. Bertaud, M. Sowinska, M. Lukosius, M. Fraschke, D. Wolansky, B. Tillack, E. Miranda, and C. Wenger, IEEE Trans. Electron Devices **58**, 3124 (2011).

[20] S. Yu, X. Guan, and H.-S. P. Wong, Appl. Phys. Lett. **99**, 063507 (2011).

[21] Z. Wei, Y. Kanzawa, K. Arita, Y. Katoh, K. Kawai, S. Muraoka, S. Mitani, S. Fujii, K. Katayama, M. Iijima, T. Mikawa, T. Ninomiya, R. Miyanaga, Y. Kawashima, K. Tsuji, A. Himeno, T. Okada, R. Azuma, K. Shimakawa, H. Sugaya, T. Takagi, R. Yasuhara, K. Horiba, H. Kumigashira, and M. Oshima, *2008 IEEE Int. Electron Devices Meet.* (2008) DOI: 10.1109/IEDM.2008.4796676.

[22] J. J. Yang, M.-X. Zhang, J. P. Strachan, F. Miao, M. D. Pickett, R. D. Kelley, G. Medeiros-Ribeiro, and R. S. Williams, Appl. Phys. Lett. **97**, 232102 (2010).

[23] M.-J. Lee, C. B. Lee, D. Lee, S. R. Lee, M. Chang, J. H. Hur, Y.-B Kim, C.-J Kim, D. H. Seo, S. Seo, U.-I. Chung, I.-K. Yoo, and K. Kim, Nature Materials **10**, 625 (2011).

[24] S. Nigo, M. Kubota, Y. Harada, T. Hirayama, S. Kato, H. Kitazawa, and G. Kido, J. Appl. Phys. **112**, 033711 (2012).

[25] W. Kim, S. I. Park, Z. Zhang, Y. Yang-Liauw, D. Sekar, H.-S. P. Wong, and S. S. Wong, *2011 Symp. on VLSI Technol.* (2011) p. 22.

[26] K. Fujiwara, T. Nemoto, M. J. Rozenberg, Y. Nakamura, and H. Takagi, Jpn. J. Appl. Phys. **47**, 6266 (2008).

[27] I. H. Inoue, S. Yasuda, H. Akinaga, and H. Takagi, Phys. Rev. B **77**, 035105 (2008).

[28] C.H. Ho, C.-L. Hsu, C.-C. Chen, J.-T. Liu, C.-S. Wu, C.-C. Huang, C. Hu, and F.-L Yang, *2010 Int. Electron Devices Meet.* (2010) p. 19.1.1.

[29] K. Jung, Y. Kim, W. Jung, H. Im, B. Park, J. Hong, J. Lee, J. Park, and J.-K. Lee, Appl. Phys. Lett. **97**, 233509 (2010).

[30] G. A. Slack, J. Appl. Phys. **31**, 1571 (1960).

[31] I. Wakabayashi, H. Kobayashi, H. Nagasaki, and S. Minomura, J. Phys. Soc. Jpn. **25**, 227 (1968).

[32] K. Momma and F. Izumi, J. Appl. Crystallogr. **44**, 1272 (2011).

[33] G. A. Sawatzky and J. W. Allen, Phys. Rev. Lett. **53**, 2339 (1984).

[34] J. Zaanen, G. A. Sawatzky, and J. W. Allen, Phys. Rev. Lett. **55**, 418 (1985).

[35] H. J. Van Daal and A. J. Bosman, Phys. Rev. **158**, 736 (1967).

[36] S. Koide, J. Phys. Soc. Jpn. **20**, 123 (1965).

[37] A. J. Springthorpe, I. G. Austin, and B. A. Austin, Solid State Commun. **3**, 143 (1965).

[38] I. G. Austin, A. J. Springthorpe, B. A. Smith, and C. E. Tuner, Proc. Phys. Soc. **90**, 157 (1967).

[39] A. J. Bosman and C. Crevecoeur, Phys. Rev. **144**, 763 (1966).

[40] J. F. Gibbons and W. E. Beadle, Solid-State Electron. **7**, 785 (1964).

[41] C. Dumas, D. Deleruyelle, A. Demolliens, C. Muller, S. Spiga, E. Cianci, M. Fanciulli, I. Tortorelli, and R. Bez, Thin Solid Films **519**, 3798 (2011).

[42] M. Kawai, K. Ito, and Y. Shimakawa, Appl. Phys. Lett. **95**, 012109 (2009).

[43] H. Kondo, M. Arita, T. Fujii, H. Kaji, M. Moniwa, T. Yamaguchi, I. Fujiwara, M. Yoshimaru, and Y. Takahashi, Jpn. J. Appl. Phys. **50**, 081101 (2011).

[44] D. Ielmini, S. Spiga, F. Nardi, C. Cagli, A. Lamperti, E. Cianci, and M. Fanciulli, J. Appl. Phys. **109**, 034506 (2011).

[45] I. Hotový, D. Búc, Š. Haščík, and O. Nennewitz, Vacuum **50**, 41 (1998).

[46] A. Demolliens, C. Muller, D. Deleruyelle, S. Spiga, E. Cianci, M. Fanciulli, F. Nardi, C. Cagli, and D. Ielmini, *2009 IEEE Int. Memory Workshop* (2009) DOI: 10.1109/IMW.2009.5090606.

[47] C. Kügeler, R. Weng, H. Schroeder, R. Symanczyk, P. Majewski, K.-D. Ufert, R. Waser, and M. Kund, Thin Solid Films **518**, 2258 (2010).

[48] H. Shima, F. Takano, H. Muramatsu, H. Akinaga, Y. Tamai, I. H. Inque, and H. Takagi, Appl. Phys. Lett. **93**, 113504 (2008).

Chapter 3

Effects of Heat Treatment on Chemical and Electrical Properties of Resistive Switching Cells

3.1 Introduction

As discussed in Chapter 1, to clarify the origin of conductive filaments is important to understand the mechanism of a resistive switching (RS) phenomenon. Although the origin of the filaments are not completely understood, it has been proposed that their origin is related to defects such as oxygen vacancies [1] or metal precipitates [2]. Thus, the relationship between electrical characteristics of RS cells and the properties, in particular, chemical composition, of nickel oxide (NiO) films may give clues on the origin of the filaments.

On the other hand, resistance in the initial state (R_{Ini}), which corresponds to resistivity of NiO films, is also an important character because it determines the upper limit of resistance in the high-resistance state (HRS), R_{HRS}. Therefore large R_{Ini} is desirable to ensure large resistance ratio or to reduce operation current while keeping the sufficient resistance ratio. It has been known that point defects (vacancies of interstitials) act as dopant, giving rise to semiconductor-like conduction in metal oxides [3]. In a single crystalline NiO, majority defects in thermal equilibrium are nickel (Ni) vacancies (V_{Ni}), which act as acceptors, giving rise to *p*-type conduction [3–5]. Therefore, chemical composition influences on the resistivity of NiO films. In addition, sputtered-NiO films are frequently deposited under nonequilibrium conditions, and thus, they may contain several types of defects besides V_{Ni}, *e.g.* oxygen (O) vacancies (V_{O}) and Ni interstitials ($\mathrm{Ni_i}$). Furthermore, NiO films are composed of nanocrystals with diameters of tens of nm, as will be shown in Chapter 5, also including grain boundaries (GBs). These structural defects may also influence the electrical properties of NiO films. Nevertheless, detailed studies on the conduction mechanism of NiO films are still insufficient.

In this chapter, electrical properties of RS cells in the initial state and the chemical composition of NiO-films are investigated by altering the NiO-film properties to clarify the origin of conduc-

tive filaments as well as the dominant factors determining R_{Ini}. Heat treatment was adopted as a method to alter the NiO-film properties because it is a most simple and effective way to systematically alter the film properties. It was found that oxygen desorption from NiO films can give rise to filament formation. On the other hand, the R_{Ini} was increased by heat treatment under which the oxygen desorption rarely took place. It has been revealed that the increase in R_{Ini} is linked to the increase in the activation energy for conduction.

3.2 Experimental Procedure

RS cells of platinum (Pt)/NiO/Pt stack structure were fabricated on *p*-silicon (Si) (100) substrates. As bottom electrodes (BEs), 100-nm-thick Pt was deposited on *p*-Si by electron beam (EB) evaporation. After the BE deposition, NiO films were deposited at room temperature (RT) in the mixture of argon (Ar) and oxygen (O_2). The proportion of O_2 in the atmosphere, O_2/(Ar + O_2), and the total gas pressure were kept at 5% and 0.6 Pa, respectively. The thickness of the NiO films was about 130 nm. A Pt film with 100 nm thickness was deposited on the NiO films by EB evaporation using a shadow mask to form top electrodes (TEs). The diameter of the TEs was 100 μm. Heat treatment was carried out before or after the deposition of TEs, namely, without or with TEs, and the conditions were as follows: 30 min in vacuum ($< 3 \times 10^{-3}$ Pa) or Ar at 220 or 300°C. Nine different kinds of samples including as-deposited samples were eventually fabricated. Electrical properties of RS cells were characterized by the measurements of current-voltage (*I*–*V*) characteristics and the temperature dependence of resistance. The chemical composition of the NiO films was analyzed on the area not covered with the TEs, using energy-dispersive X-ray spectrometry (EDX).

3.3 Chemical Composition and Electrical Properties of NiO Films

3.3.1 Chemical composition of NiO films

Table 3.1 shows the oxygen composition of NiO films before and after heat treatment. As-deposited NiO films had a Ni-rich composition of $NiO_{0.94}$. Seo *et al.* have also reported RS behavior in Ni-rich NiO [6]. No remarkable changes in the composition of the NiO films were observed after the heat treatment in vacuum at 220°C, in Ar at 220 and 300°C. On the other hand, the oxygen composition was significantly decreased to 0.90 after the heat treatment in vacuum at 300°C, indicating that oxygen desorption from the NiO films took place during the heat treatment.

Table 3.1: Oxygen composition of the NiO films before and after heat treatment.

	As-deposited	Vacuum	Ar
	0.94	–	–
220°C	–	0.94	0.94
300°C	–	0.90	0.93

3.3.2 Current-voltage characteristics

Figure 3.1 (a) shows the distributions of R_{Ini} at a TE bias voltage of 0.1 V before and after heat treatment with a TE. R_{Ini} of as-deposited cells was about 3.5 kΩ. After the heat treatment in vacuum at 220°C, R_{Ini} of the RS cells was increased by more than four orders of magnitude to about 100 MΩ and showed good uniformity among the RS cells. In the case of heat treatment in Ar, R_{Ini} was also increased to about 5 MΩ at 220°C and 50 MΩ at 300°C, and also showed good uniformity. Shima *et al.* also reported an increase in R_{Ini} in NiO films upon annealing in Ar ambient at 700°C [7]. In contrast, after the heat treatment in vacuum at 300°C, R_{Ini} of the RS cells was decreased compared to the RS cells heated in vacuum at 220°C, and showed a very large variation among the RS cells. Since significant oxygen desorption from the NiO films occurred only after the heat treatment in vacuum at 300°C, the decrease in R_{Ini} and the large variation may be attributed to the oxygen desorption.

Figure 3.1 (b) shows the distributions of R_{Ini} before and after heat treatment without a TE. The distributions of R_{Ini} were similar to those in the case of heat treatment with a TE. Note that the magnitude of R_{Ini} was virtually independent of the polarity of the bias voltage (data not shown). Since R_{Ini} in the samples heated with and without a TE are comparable to each other at both positive and negative bias voltages, the increase in R_{Ini} is not caused by the formation of a potential barrier at the TE/NiO interface. Furthermore, the increase in R_{Ini} is not attributed to a potential barrier at the NiO/BE interface, because R_{Ini} at bias voltages of both polarity was similarly increased in the samples heated without a TE. The increase in R_{Ini}, therefore, originates from a change in the bulk properties of NiO not from a change at the Pt/NiO interface. On the other hand, after the heat treatment without a TE by which the oxygen composition of the NiO films was not changed (in vacuum at 220°C, in Ar at 220°C and 300°C), some cells exhibited R_{Ini} ranging from 10 to 100 kΩ, which was lower than that of most other cells. It will be discussed later why R_{Ini} was decreased in these cells even though the oxygen composition of the NiO films was scarcely changed by the heat treatment.

Figure 3.2 (a)-(c) show the I–V characteristics of (a) an as-deposited RS cell, and an RS cell after heat treatment with a TE in vacuum at (b) 220°C and (c) 300°C. During the measurements, the current compliance (I_{comp}) for the forming and set processes was set to 10 mA to avoid the degradation of the RS cells. RS cells in all the samples exhibited reproducible unipolar resistive switching. As shown in Fig. 3.2 (a), in the initial voltage sweep of the as-deposited RS cell, the current monotonically increased with increasing applied voltage, and a forming process occurred when the applied voltage was about 6 V. The R_{HRS} was as large as the R_{Ini}, and the resistance in the low-resistance state (LRS), R_{LRS}, was about 60 Ω. The initial state of the RS cell after heat treatment in vacuum at 220°C was also high resistance and a forming process occurred, as shown in Fig. 3.2 (b). In addition, R_{HRS} was increased by the heat treatment in vacuum at 220°C, whereas R_{LRS} and the switching voltages were comparable to those of the as-deposited RS cells. The reason why R_{LRS} was not affected by the heat treatment may be that the current compliance during the set process was fixed to 10 mA throughout the measurements [6, 8]. R_{HRS} was also

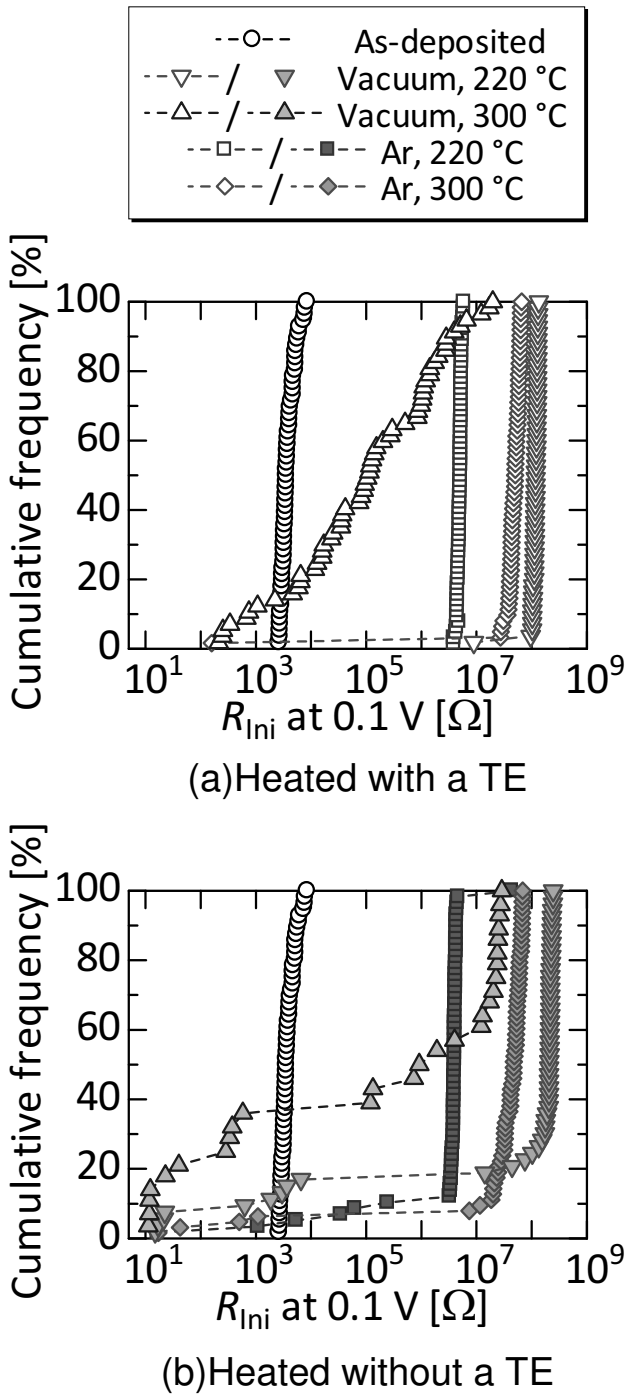

Figure 3.1: Cumulative frequency of initial resistance of RS cells after heat treatment (a) with a TE and (b) without a TE.

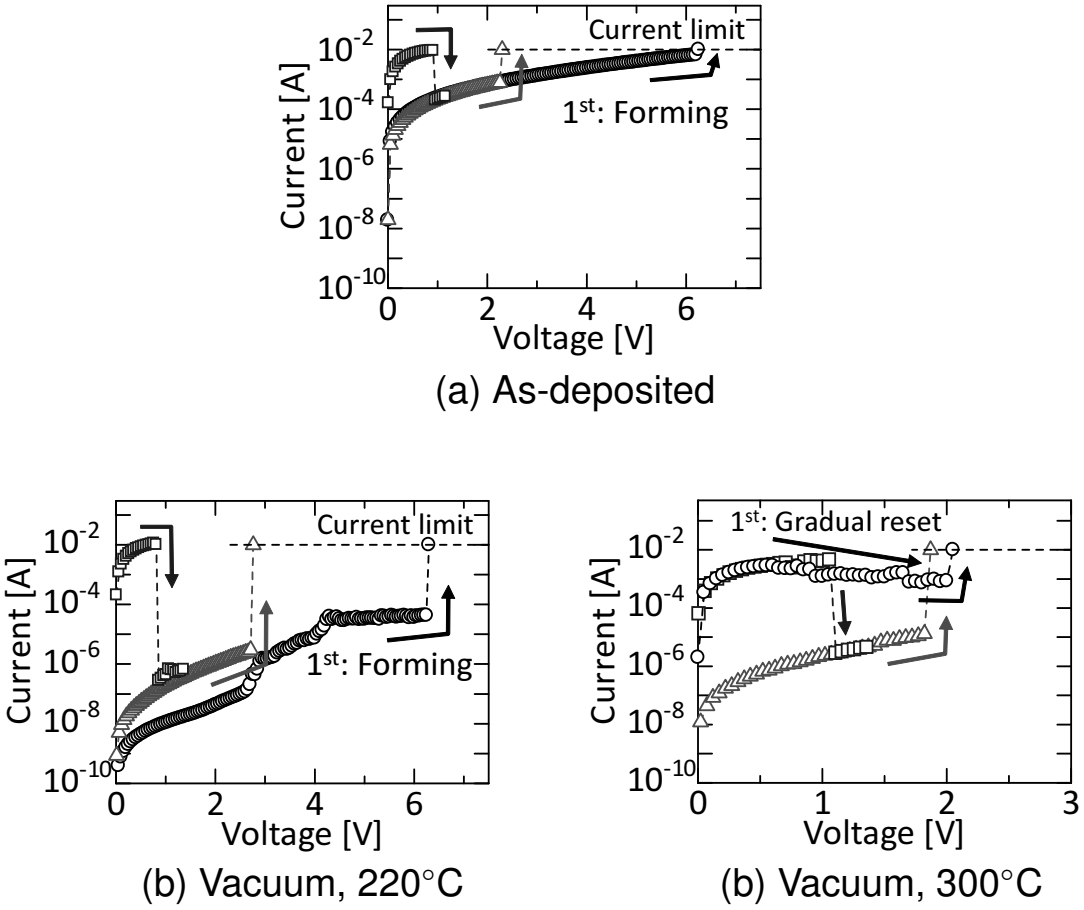

Figure 3.2: Current-voltage characteristics of (a) an as-deposited RS cell, an RS cell after heat treatment (b) in vacuum at 220°C, and (c) at 300°C.

increased in the case of heat treatment in Ar at 220°C and in Ar at 300°C. Note that as expected from the filament model [9], the initial state exhibits high-resistance character, and R_{HRS} is similar to or lower than R_{Ini}, in the as-deposited RS cells as well as most of the RS cells in which the oxygen composition of the NiO films was not changed by the heat treatment.

Figure 3.2 (c) shows the RS characteristics of the RS cell after heat treatment in vacuum at 300°C. R_{Ini} of the RS cell is decreased from about 3.5 kΩ to 150 Ω. In the first voltage sweep, the current gradually decreased with increasing applied voltage, which is similar to the reset process, and then the set process occurred at about 2 V. In the RS characteristics, the R_{LRS} was about 100 Ω, which was comparable to the R_{Ini}, and R_{HRS} was increased to about 1 MΩ by the heat treatment. These *I*–*V* characteristics indicate that the initial state of the RS cell after heat treatment in vacuum at 300°C is equivalent to the LRS. In other words, filaments were formed in advance without a forming process, and hence, by the heat treatment. RS cells, the initial state of which is equivalent to the LRS, were observed mostly after heat treatment at 300°C where significant oxygen desorption from the NiO films took place, indicating that filaments were generated by oxygen desorption. As a results of the filament formation, the R_{Ini} may be decreased after heat treatment in vacuum at 300°C compared with that after heat treatment in vacuum at 220°C.

3.3.3 Temperature dependence of initial resistance

The temperature dependence of R_{Ini} in the temperature range from 100 to 350 K was investigated for the RS cells, in which the oxygen composition of the NiO films was not changed by the heat treatment, *i.e.*, the as-deposited cells, and those heated in vacuum at 220°C, in Ar at 220 and 300°C. Arrhenius plots of the R_{Ini} in the RS cells are shown in Fig. 3.3 (a). The R_{Ini} decreases exponentially with increasing temperature near room temperature. Note that the detection limit of the measuring instrument was 1 pA, which corresponded to the resistance of 10^{11} Ω. It has been reported that resistivity of NiO is thermally activated [4, 5, 10]. Hence, it is assumed that R_{Ini} is described as:

$$R_{\mathrm{Ini}} = R_0 \exp\left(\frac{E_{\mathrm{a}}}{k_{\mathrm{B}}T}\right), \tag{3.1}$$

where R_0 is a constant, E_{a} is the activation energy, k_{B} is the Boltzmann constant, and T is the temperature. Using the R_{Ini} values near room temperature, the activation energy was estimated. The activation energy was 260 meV for the as-deposited cell, and was increased to 420 meV by the heat treatment in vacuum at 220°C, 300 meV, and 340 meV in Ar at 220°C and 300°C, respectively. Figure 3.3 (b) shows a plot of the R_{Ini} against the activation energy. The R_{Ini} monotonically increased with the activation energy, indicating that the increase in R_{Ini} due to the heat treatment was linked to the increase in the activation energy.

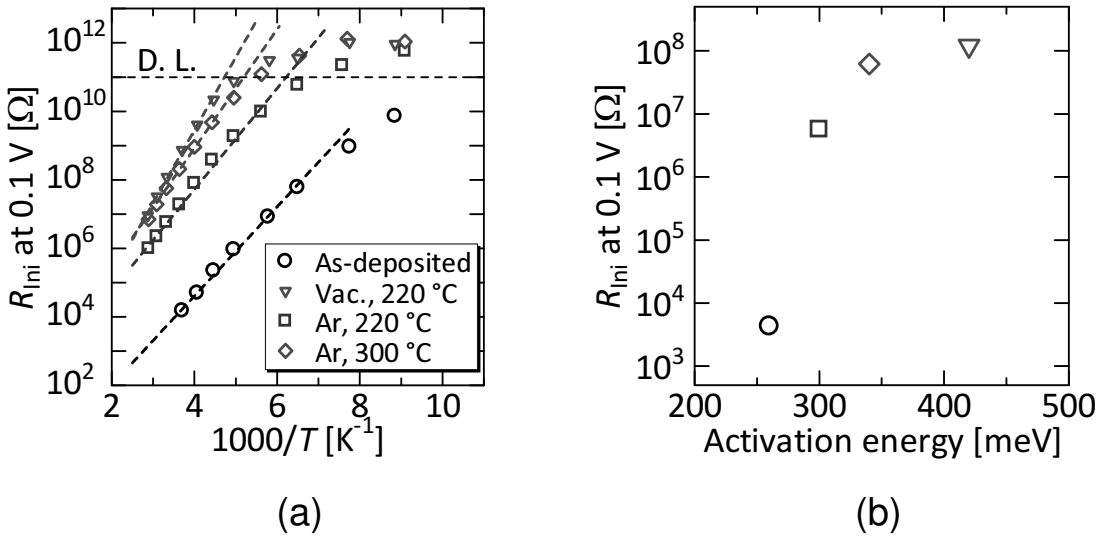

Figure 3.3: (a) Arrhenius plots of the R_{Ini}. (b) The R_{Ini} plotted against activation energy of R_{Ini}.

3.3.4 Discussion

Filament formation by heat treatment

As described in Section 1.3.1, based on the filament model, the LRS is considered to be the state in which conductive filaments are formed between the two electrodes. RS cells that exhibited an initial state equivalent to the LRS appeared mostly after the heat treatment in vacuum at 300°C, where significant oxygen desorption from the NiO films took place Therefore, filaments may be formed within the RS cells by the oxygen desorption from the NiO films, and thereby the initial state of the RS cells became equivalent to the LRS. Taking account of the result that filaments are formed by oxygen desorption, the filaments may consist of oxygen vacancies, which induce a similar phenomenon in $SrTiO_3$ [11]. In addition, the large variation of R_{Ini} among the RS cells with a TE of diameter 100 μm may result from the difference in the number or thickness of the filaments formed among the RS cells [12], indicating that the formed filaments are spatially distributed at an interval on the order of 10 μm. The difference in the number or thickness of the filaments may be owing to the stochastic nature of filament formation. The forming process by a voltage application can be described as a percolation model [13, 14], where a percolation path (a filament in this study) is modeled as a cluster of defects, and connects a TE and a BE as a result of the defect generation by electrical stress, as schematically depicted in Fig. 3.4. Based on the model, the defect density necessary to the formation of a single filament varies among cells, conforming to Weibull distribution [15, 16]. On the other hand, if the defect density is the same among cells, the number or thickness of the filaments can vary among the cells [17]. Since, in this study, the spatial distribution of defects generated by oxygen desorption is presumed to be almost uniform among the RS cells, the number or thickness of the resulting filaments may vary among cells, in a similar manner to the voltage-induced filaments. As a consequence, the difference in the number or thickness of the filaments was observed as the large variation in R_{Ini}.

R_{Ini} was decreased in some RS cells, even after the heat treatment without a TE, by which the oxygen composition of NiO films was not changed, and the RS cells were initially in the LRS (data not shown). Kawai *et al.* reported that the RS cells initially in the LRS were observed in Pt/NiO/platinum-iridium (PtIr) structures, for which NiO films were annealed at 450°C for 30 min following NiO deposition by pulsed-laser deposition [18] . In their study, the composition of the NiO films was determined to be unchanged by the annealing using Auger electron spectroscopy (AES). Taking account of the results of the heat treatment without a TE and Ref. 18, the filaments can be generated by oxygen desorption in localized area such as grain boundaries [2]. Because of the very localized composition change, it could not be detected by SEM-EDX and AES. Furthermore, the oxygen desorption during heat treatment was suppressed by the existence of the TE, resulting in the formation of fewer filaments. On the other hand, during heat treatment in vacuum at 300°C, oxygen atoms in NiO could diffuse more easily, and sufficient oxygen desorption occurred to form filaments within the RS cells even in the samples heated with a TE. In the case of heat treatment in vacuum at 300°C, therefore, R_{Ini} distribution in the sample heated with a TE is similar to that in the sample heated without a TE.

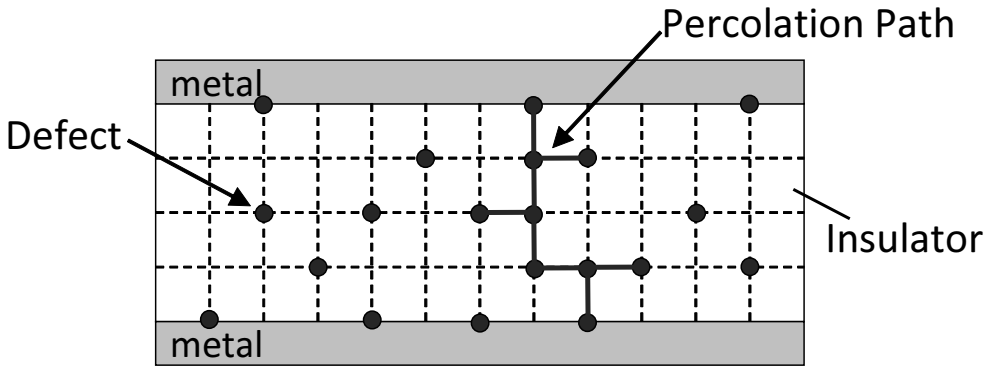

Figure 3.4: A schematic illustration of a percolation model.

Increase in activation energy in R_{Ini}

The activation energy in (3.1) may be related to the energy for thermal excitation of a hole from a trap level or an acceptor level to the valence band [19, 20], which is also discussed in Chapter 6. A trap level can depend on the microstructure of a material including defect structure and its surrounding. On the other hand, it was reported that in lithium-doped NiO, the activation energy of resistivity was lowered as the concentration of lithium is increased, where lithium acted as acceptors [4, 5]. Therefore, the increase in the activation energy may be attributed to the changes in NiO-film properties, including their microstructure and the concentration of acceptors, caused by the heat treatment.

3.4 Summary

Effects of heat treatment on the RS characteristics of cells were investigated. After the heat treatment, by which the chemical composition of NiO films was not changed, R_{Ini} of the RS cells significantly increased. The increase in R_{Ini} originates from the change in the bulk properties of NiO films, not a change at the Pt/NiO interface. It was revealed that the increase in R_{Ini} is linked to the increase in its activation energy, which may be related to the energy for the excitation of a hole from a trap or an acceptor level to the valence band in NiO. On the other hand, after the heat treatment in vacuum at 300°C, by which significant oxygen desorption from NiO films occurred, R_{Ini} for the RS cells was decreased, and the initial state of the RS cells became equivalent to the LRS. The RS cells initially in the LRS may be result from the formation of filaments within the RS cells by oxygen desorption, indicating that the origin of filaments are defects generated by the oxygen desorption, and thus, related to oxygen vacancies. The large variation in R_{Ini} among the RS cells after the heat treatment in vacuum at 300°C may originate from the difference in the number or thickness of the generated filaments owing the stochastic nature of a filament-formation process.

References

[1] S. Yu, X. Guan, and H.-S. P. Wong, Appl. Phys. Lett. **99**, 063507 (2011).

[2] G.-S. Park, X.-S. Li, D.-C. Kim, R.-J. Jung, M.-J. Lee, and S. Seo, Appl. Phys. Lett. **91**, 222103 (2007).

[3] P. A. Cox, *Transition Metal Oxides —An introduction to their electronic structure and properties* (Oxford University Press, New York, 2010).

[4] S. Koide, J. Phys. Soc. Jpn. **20**, 123 (1965).

[5] I. G. Austin, A. J. Springthorpe, B. A. Smith, and C. E. Tuner, Proc. Phys. Soc. **90**, 157 (1967).

[6] S. Seo, M. J. Lee, D. H. Seo, E. J. Jeoung, D.-S. Suh, Y. S. Joung, I. K. Yoo, I. R. Hwang, S. H. Kim, and I. S. Byun, J.-S. Kim, J. S. Choi, and B. H. Park, Appl. Phys. Lett. **85**, 5655 (2004).

[7] H. Shima, F. Takano, H. Akinaga, Y. Tamai, I. H. Inoue, and H. Takagi, Appl. Phys. Lett. **91**, 012901 (2007).

[8] K. Kinoshita, K. Tsunoda, Y. Sato, H. Noshiro, S. Yagaki, M. Aoki, and Y. Sugiyama, Appl. Phys. Lett. **93**, 033506 (2008).

[9] J. F. Gibbons and W. E. Beadle, Solid-State Electron. **7**, 785 (1964).

[10] D. Adler and J. Feinleib, Phys. Rev. B **2**, 3112 (1970).

[11] K. Szot, W. Speier, R. Carius, U.Zastrow, and W. Beyer, Phys. Rev. Lett. **88**, 075508 (2002).

[12] D. C. Kim, S. Seo, S. E. Ahn, D.-S. Suh, M. J. Lee, B.-H. Park, I. K. Yoo, I. G. Baek, H.-J. Kim, E. K. Yim, J. E. Lee, S. O. Park, H. S. Kim, U.-I. Chung, J. T. Moon, and B. I. Ryu, Appl. Phys. Lett. **88**, 202102 (2006).

[13] G. Buh, I. Hwang, and B. H. Park, Appl. Phys. Lett. **95**, 142101 (2009).

[14] Y. Nishi, T. Iwata, D. Horie, and T. Kimoto, *Mater. Res. Soc. Symp. Proc.* **1430** (2012) DOI: 10.1557/opl.2012.1023.

[15] J. Suñé, I. Placencia, N. Barniol, E. Farrès, F. Martín, and X. Aymerich, Thin Solid Films **185**, 347 (1990).

[16] R. Degraeve, G. Groeseneken, R. Bellens, M. Depas, and H. E. Maes, *1995 Int. Electron Devices Meet.* (1995) p. 863.

[17] J. Suñé and E. Wu, *2002 Int. Electron Devices Meet.* (2002) p. 147.

[18] M. Kawai, K. Ito, N. Ichikawa, and Y. Shimakawa, Appl. Phys. Lett. **96**, 072106 (2010).

[19] I. G. Austin and N. F. Mott, Adv. Phys. **50**, 757 (2001).

[20] A. J. Bosman and C. Crevecoeur, Phys. Rev. **144**, 763 (1966).

Chapter 4

Identification of the Location of Filaments and Their Microscopic Properties

4.1 Introduction

In Chapter 3, it has been shown that the origin of conductive filaments are related to oxygen vacancies, namely, related to the partial reduction of nickel oxide (NiO). The evidence presented in the previous chapter, however, is indirect. In addition, the detailed properties of filaments such as size (shape, diameter, etc.), chemical composition, and resistivity, have not been fully clarified.

A number of studies on the properties of the filaments have been reported. Localized conductive spots with diameters ranging from 10 to 100 nm have been detected in resistive switching (RS) cells in the low-resistance state (LRS) by various techniques, including conductive-atomic force microscopy (C-AFM) [1–6], electron-beam absorbed current measurement [7], and others [8–10]. On the other hand, changes in the structure and composition of the oxide layers of RS cells after the forming and switching have been observed by cross-sectional transmission electron microscopy (XTEM) [8, 10–12]. Nevertheless, comprehensive studies that link the electrical properties of such conductive spots to the structural and compositional changes of an oxide layer are limited [7, 9, 10]. Furthermore, it is still unclear how the electrical and structural (size and shape) properties of the filaments influence the resistances in RS cells.

In this chapter, the areas and current of conductive filaments formed in RS cells were observed by C-AFM. The relationships between the electrical and structural properties of the filaments and resistance in the LRS (R_{LRS}) were investigated. The shape and chemical composition of the filaments were also analyzed by XTEM.

4.2 Experimental Procedure

4.2.1 RS cell fabrication

As bottom electrodes (BEs), 100 nm-thick-platinum (Pt) was deposited by electron beam (EB) evaporation on a thermally-oxidized silicon (Si) wafer, where the thickness of silicon dioxide (SiO_2) was about 200 nm. Between Pt and SiO_2, a titanium (Ti) layer with a thickness of 5 nm was inserted. Pt films directly deposited onto a Si wafer used in Chapter 3 were poor adhesive and frequently peeled off during a cell fabrication process. On the other hand, Pt/Ti/SiO_2/Si has been frequently used for the substrates of RS cells [13–15]. It has been known that the insertion of Ti between Pt and SiO_2 improves their adhesion [16]. Hence, in this chapter, Pt (100 nm)/Ti (5 nm)/SiO_2/Si was used as a substrate for NiO deposition, where Ti and Pt were deposited by EB evaporation.

NiO films were deposited at room temperature (RT). During the deposition, the proportion of oxygen (O_2) in the atmosphere and the ambient pressure were kept at 10% and 0.6 Pa, respectively. The thickness of the NiO films was about 100 nm. Pt films with a thickness of 200 nm were deposited on the NiO films to form top electrodes (TEs). The TE thickness of 200 nm was twice as thick as that in Chapter 3. The deposition rate of the TEs was maintained to ≈ 0.2 nm/sec, which was relatively fast compared with that of BEs (≈ 0.08 nm/sec). Because of the fast deposition rate and the thickness, TEs were a poor adhesive and removed easily.

4.2.2 Measurement procedure

Current-voltage (I–V) characteristics were measured by a DC voltage sweep with an increment of 10 mV. During I–V measurements a positive bias voltage was applied on the TEs of RS cells, while BEs were grounded. Current compliance (I_{comp}) during the forming was typically set to 1 mA. For C-AFM observation, RS cells just after the forming were used. After the forming, TEs were removed by ultrasonic vibration in acetone following scratching using a needle to prevent the chemical changes of the filaments and NiO layers. Then, the local resistances of NiO layers were measured by C-AFM. C-AFM was carried out in the air using a platinum-iridium (PtIr)-coated probe with a tip radius of 20 nm. The number of data points for C-AFM was 256×256. After specifying the location of a filament, the structural and compositional changes of a NiO layer near the filament were investigated by XTEM and energy-dispersive X-ray spectrometry (EDX).

4.3 Cell Deformation Induced by the Forming Process

Figure 4.1 shows typical I–V characteristics of an RS cell with a diameter of 300 μm. The forming occurred at about 5.7 V in the initial voltage sweep. After that, the cell exhibited repetitive resistive switching several times. Nomarski microscopy images of the RS cell are depicted in Fig. 4.2. A deformation appeared after the forming (b), and it expanded after the resistive switch-

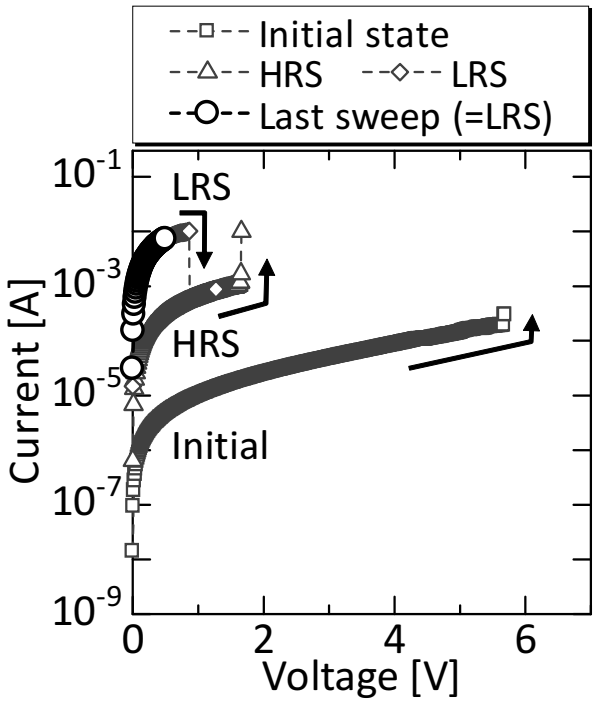

Figure 4.1: *I–V* characteristics of an RS cell with a diameter of 300 μm. After the resistive switching of several times, resistance state was set to LRS, which is indicated as Last sweep.

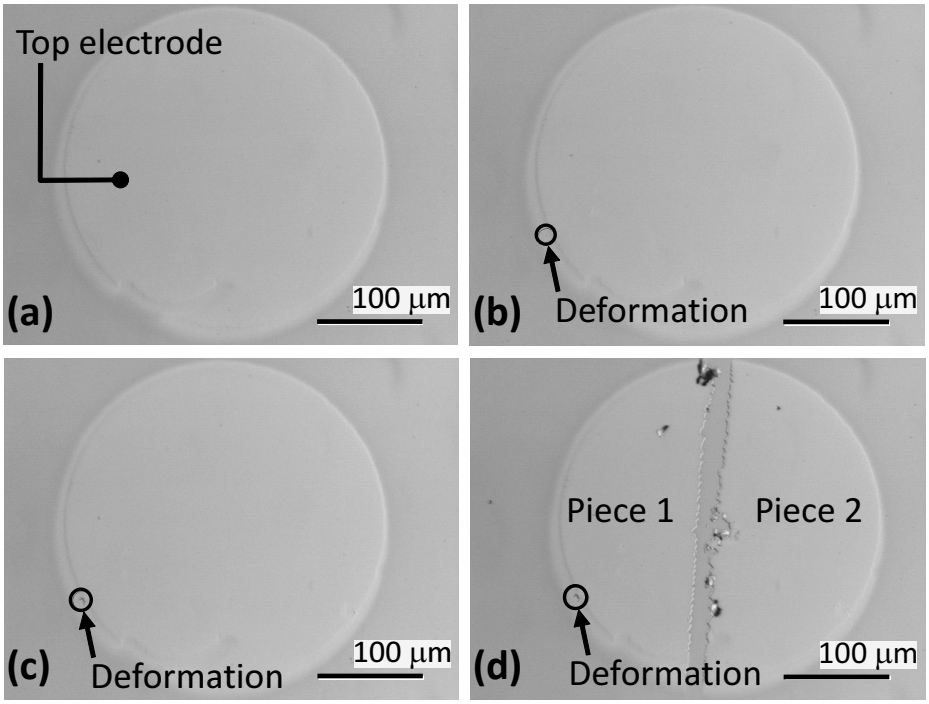

Figure 4.2: Nomarski microscopy images of the RS cell (a) in the initial state, (b) after forming, and (c) after switching, respectively. *I–V* characteristics is depicted in Fig. 4.1. Deformation was observed after forming, and it extended by repetitive switching, as indicated by an circle in the figures. After switching, the RS cell is separated into two pieces.

ing (c), as indicated by a circle in the figures. After the resistive switching, the resistance state of the RS cell was set to the LRS ("Last sweep" in Fig. 4.1), and then, separated into two pieces where one included the deformation (piece 1) and the other did not (piece 2), as shown in Fig. 4.2 (d). *I–V* characteristics of the piece 1 and the piece 2 as well as those of the RS cell just before the separation are shown in Fig. 4.3. The piece 1, which included the deformation, exhibited a similar *I–V* characteristic in the first sweep to those of the RS cell before the separation and showed reset behavior, indicating that filaments existed in advance in the piece 1. On the other hand, the piece 2 exhibited high-resistance characteristics and forming-like behavior in the first sweep, representing the character of the initial state. These results evidence that filaments existed in the neighborhood of the cell deformation generated during the forming. Similar deformation accompanying the forming has been observed by other groups [12, 17, 18].

4.4 Observation of Filaments by Conductive-AFM Technique

4.4.1 Electrode removal and Conductive-AFM observation

I–V measurements were carried out on an RS cell with a diameter of 50 μm shown in Fig. 4.4 (a). Figure 4.4 (c) shows a Nomarski microscopy image of the RS cell after the forming. *I–V* characteristics of the RS cell during the forming are shown in Fig. 4.4 (b), where I_{comp} was set to 500 μA. A protrusion appeared in a part of the RS cell as indicated by a dashed circle in Fig. 4.4 (c). Figure 4.4 (d) depicts the RS cell after the removal of the TE, a deformation of the NiO layer was observed, the location of which is the same as that of the protrusion of the TE.

C-AFM was carried out near the deformation shown in Fig. 4.4 (d). Figure 4.5 (a) shows the topography of the deformation, and Fig. 4.5 (b) and (c) show the corresponding current images. Data in Fig. 4.5 (b) and (c) were obtained using different settings of the current amplifier and plotted in different current scales. The deformation was a protrusion with a diameter of about 1 μm and a height smaller than 150 nm. It was observed that conductive spots, *i.e.* filaments, existed mostly along the edges of the protrusion. In addition, there were several kinds of filaments that show significant differences in the current flowing through them. They can be classified into two groups (F1 and F2) in terms of the magnitude of their current. F1 (indicated by a dotted ellipse in Fig. 4.5 (b) and (c)) is highly conductive, the current through which is about 500 nA when a voltage of 1 mV is applied on a C-AFM probe. On the other hand, the current through F2 [(indicated by arrows in Fig. 4.5 (b)] is smaller than 10 pA at a voltage of 1 mV. The difference in current between F1 and F2 is more than four orders of magnitude; thus, the current through F2 is negligible compared with that in F1, indicating that the resistance of this RS cell is mainly determined by the resistance of F1.

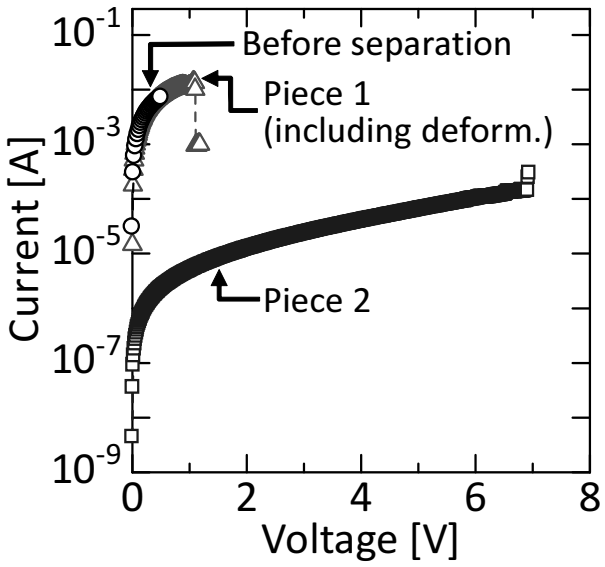

Figure 4.3: *I–V* characteristics of each separated piece and the RS cell before separation. The piece 1 included the deformation and showed similar *I–V* characteristics to the RS cell before separation. On the other hand, the piece 2 without deformation exhibited *I–V* characteristics similar to the initial state.

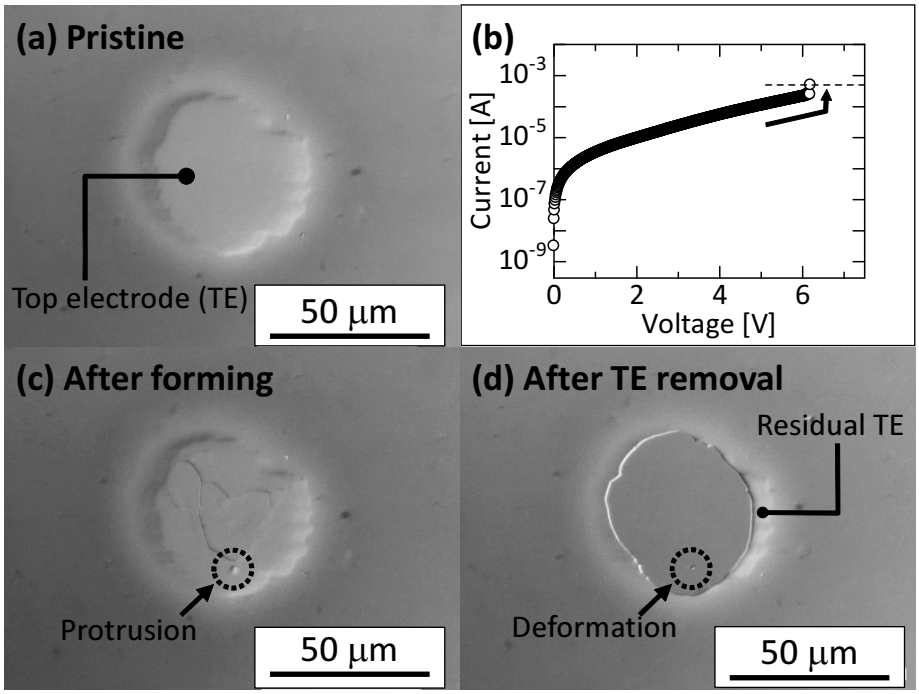

Figure 4.4: (a) A Nomarski microscopy images of an pristine RS cell with a diameter of 50 μm. (b) *I–V* characteristics during the forming in the RS cell shown in (a). Nomarski images of the RS cell after (c) the forming and after (d) the TE removal.

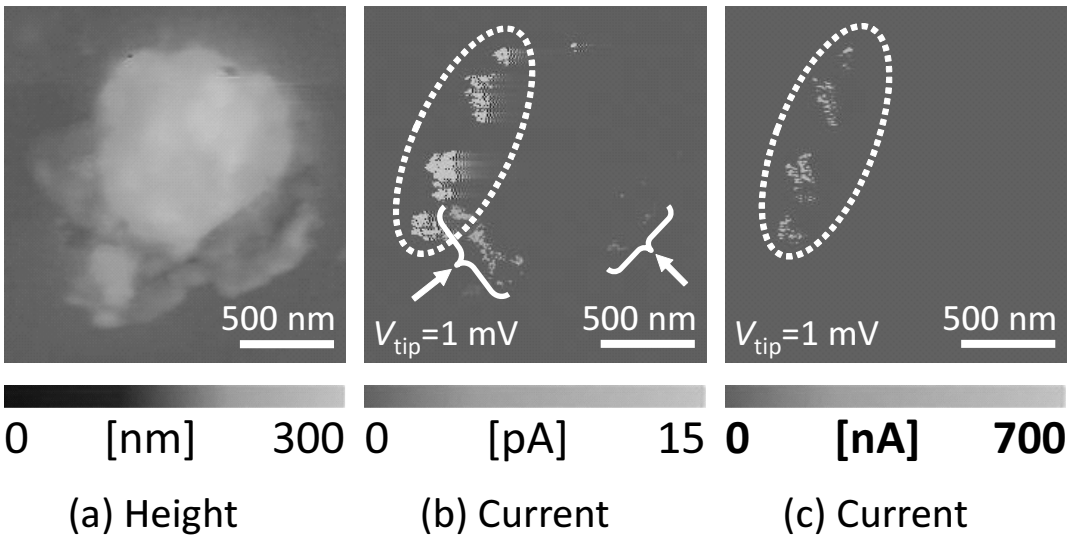

Figure 4.5: C-AFM images near the deformation shown in Fig. 4.4 (d). (a) shows topology, while (b) and (c) current images, respectively. (b) and (c) are different in current scale.

4.4.2 Spatial distribution of filaments and relationship with resistance of cells

In a similar manner to Section 4.4.1, C-AFM was carried out on RS cells with various R_{LRS} values (10–220 Ω) after the forming, not after repetitive RS operation, to prevent further expansion of the deformations [4]. In some RS cells, deformations observed are depressions, not protrusions. Although most parts of the filaments (both F1 and F2) mainly existed along the edges of a deformation in each RS cell, F1 in some RS cells was also located near the center of a deformation, as reported in titanium dioxide (TiO_2) [4]. Figure 4.6 shows areas of the filaments observed by C-AFM in RS cells with various R_{LRS} values plotted against the filament current at 1 mV. In RS cells with R_{LRS} less than 100 Ω, both F1 and F2 existed. Although filaments other than F1 and F2 also existed, their current is smaller than that of F1 by about two orders of magnitude, and thus negligible. In these RS cells, therefore, R_{LRS} is determined by the resistance of F1. On the other hand, in RS cells with R_{LRS} larger than 100 Ω, only F2 was observed. The R_{LRS} of these RS cells is, however, not likely to be dominated by the resistance of F2, because the current through F2 is smaller than that through F1 by more than four orders of magnitude, while the variation in R_{LRS} among all the RS cells is at most 22 times (10–220 Ω). In RS cells with R_{LRS} larger than 100 Ω, the area of F1 may be too small to be detected, as will be discussed later. Consequently, R_{LRS} in the range of 10–220 Ω may be determined by the resistance of F1.

The resistivity of F1 was estimated by comparing it with that of a metal film (a Pt film, the resistivity of which is about 40 μΩcm determined by the four-probe method), because it is not easy to extract resistivity from the resistance detected by C-AFM [19]. The current detected in the Pt film is comparable to that in F1, and thus the resistivity of F1 is roughly estimated to be about 40 μΩcm. As discussed above, R_{LRS} is mainly determined by the resistance of F1. Using the estimated resistivity of F1, the resistance of F1 (R_{F1}) was calculated with respect to RS cells in which F1 was observed by the following equation:

$$R_{F1} = \rho_{F1} \frac{t_{NiO}}{A_{F1}}, \tag{4.1}$$

where ρ_{F1}, t_{NiO}, and A_{F1} are the resistivity of F1, the NiO thickness, and the area of F1 measured by C-AFM, respectively. The values used are as follows: $\rho_{F1} = 40$ μΩcm and $t_{NiO} = 100$ nm. Here, it is assumed that F1 is cylindrical, that is, its in-plane cross-sectional area is nearly constant along the thickness direction. Figure 4.7 shows (a) the calculated R_{F1} plotted against R_{LRS} (measured values) and (b) the measured areas of F1 plotted against R_{LRS}. The dashed line in Fig. 4.7 (a) indicates where $R_{F1} = R_{LRS}$. On the other hand, that in Fig. 4.7 (b) represents the area of F1 calculated from equation (4.1) assuming $R_{F1} = R_{LRS}$: $A_{F1} = \rho_{F1} t_{NiO} / R_{LRS}$. As shown in Fig. 4.7 (a), R_{F1} is comparable to R_{LRS} in the RS cell with R_{LRS} of 70 Ω, indicating that the F1 in this RS cell is nearly cylindrical. On the other hand, the other three RS cells show R_{F1} lower than R_{LRS}. This indicates that the areas of F1 in these three RS cells must be smaller at the end of the TE side if the F1 is cylindrical, as represented in Fig. 4.7 (b). In these RS cells, therefore, the cross-sectional areas of F1 should vary and become narrow somewhere along the depth direction.

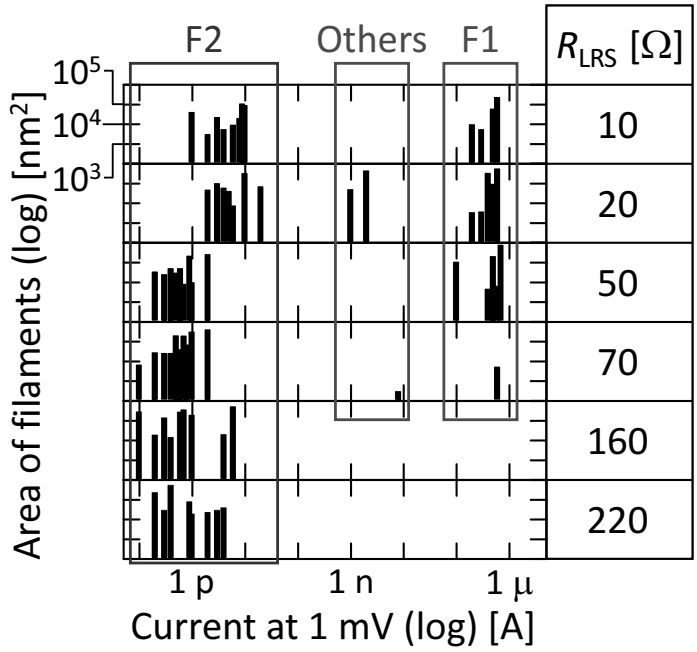

Figure 4.6: Area of filaments observed in various RS cells with different R_{LRS}, plotted against their current at a voltage of 1 mV. Both axes are plotted in a logarithmic scale.

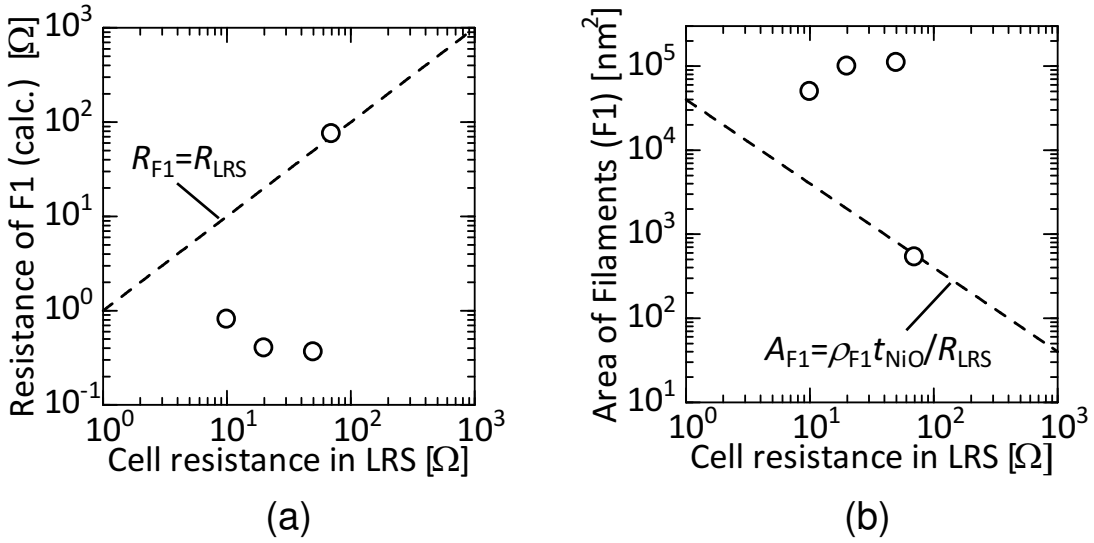

Figure 4.7: (a) The relationship between filament resistance (R_{F1}) calculated by equation (4.1) and R_{LRS}. Areas of F1 plotted against R_{LRS}.

Here, the relationship between the location of F1 and the expected shape of F1 is discussed. In RS cells where the shapes of F1 may vary along the depth direction, F1 existed mostly near the edges of a deformation (for example, see Fig. 4.5 (c)). On the other hand, in the RS cell where F1 may be cylindrical, F1 existed near the center of the deformation (data not shown). Therefore the shape of F1 may depend on its location in a deformation.

Finally in this section, it is discussed why F1 was not observed in RS cells with R_{LRS} larger than 100 Ω, as shown in Fig. 4.6. According to Fig. 4.7 (b), the areas of F1 in RS cells with R_{LRS} larger than 100 Ω are estimated to be smaller than ≈ 400 nm^2, if F1 is cylindrical. In other words, the areas of F1 can be smaller than 400 nm^2. F1 with such areas would be detectable if the vicinity of F1 were examined. However, the whole areas of the deformations must be scanned to find the location of F1. A typical scan area of C-AFM was 3×3 μm^2, which depends on the area of the deformations, and the corresponding sampling pitch was about 11.7 nm (256×256 data points). A C-AFM mapping data can include only four data points of the F1 region at most, even if its area is 400 nm^2; thus, it is not easy to directly detect F1. This may be the reason why F1 was not detected in RS cells with R_{LRS} larger than 100 Ω. From the discussion, it is concluded that the variation in R_{LRS} in the range of 10–220 Ω originates from the differences in the size and shape of filaments (F1) rather than in their resistivity.

4.5 TEM Analyses of Filaments

In Section 4.4, the exact location of filaments F1 dominating R_{LRS} was identified. Then, XTEM observation and EDX analyses were carried out near the F1 shown in Fig. 4.5 to investigate its shape and chemical composition. The R_{LRS} of the RS cell, on which XTEM was conducted, was about 10 Ω. Figure 4.8 (a) shows an AFM image of the same deformation shown in Fig. 4.5 (a). A bright-field XTEM image is depicted in Fig. 4.8 (b), where the cross section is along the dotted line shown in Fig. 4.8 (a). The deformation is observed as a depression by XTEM, while it appeared as a protrusion by C-AFM [see Fig. 4.8 (a)]. Other groups have reported the formation of cavities by the forming [12, 18], probably because of oxygen gas emission [20]. In this study, a cavity may also be formed inside the protrusion, which was supported at its edges. The protrusion may be mechanically weak and removed during sample preparation for XTEM observation. Therefore, the deformation was observed as a depression, not a protrusion, by XTEM. The solid arrow in the XTEM image indicates the location of a conductive filament (F1) observed by C-AFM.

Figure 4.8 (c) shows EDX element mappings of O, nickel (Ni), and Pt. For most parts of the deformation, a Pt-rich layer exists on the top layer, which might be the residue of the protrusion. Under the top Pt-rich layer, a NiO layer exists. On the other hand, the region beneath the solid arrow shows a different contrast from the other regions in the XTEM image (marked by a white dashed curve). Since the solid arrow points to the location of F1 detected by C-AFM, the region marked by the white dashed curve may correspond to a conductive filament F1. The region mostly consists of Pt and Ni, while the O signal intensity in the region is small compared with

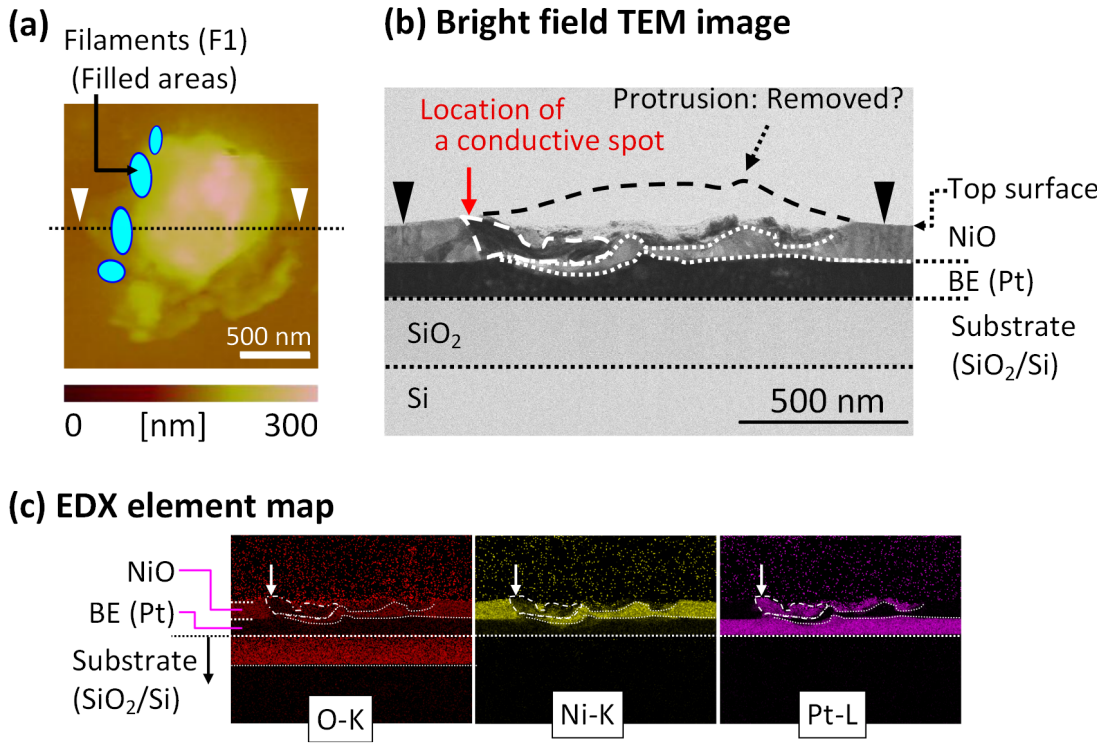

Figure 4.8: (a) Same C-AFM image of deformation shown in Fig. 4.5 (a). (b) Bright-field cross-sectional TEM image of deformation. The position of the cross section is indicated by a dotted line in (a). (c) EDX element mappings (O, Ni, and Pt) of the cross section.

that in unchanged NiO, suggesting that the conductive filaments consist of a mixture of Pt and reduced NiO. To evaluate the chemical composition of the filament (F1), EDX point analysis was conducted at several points including the region of F1 as well as in the region of unchanged NiO. The positions analyzed are indicated as white dots (points 1-3 and unchanged NiO) in Fig. 4.9 (a), which is a magnified image near the left side of the same cross section in Fig. 4.9 (b). The chemical composition of each point is shown in Fig. 4.9 (b). Point 1, which is inside of F1, exhibits a distinctly lower oxygen concentration than unchanged NiO, while the chemical compositions of points 2 and 3 are similar to that of unchanged NiO, corroborating that NiO is reduced in the filament. Note that the chemical composition at point 1 may include information on the neighboring non-conductive region owing to beam spreading. The chemical composition of the filament (the white dashed curve in Fig. 4.9 (b)) is more Pt-rich and O-deficient than that of point 1, which has been confirmed from the line profile extracted from the EDX mapping data. In addition, the results of the EDX point analysis also indicate that the shape of the filament significantly varies along the thickness direction. Note that the R_{LRS} of the RS cell analyzed by XTEM was about 10 Ω. Also, as discussed in Section 4.4.2, it has been deduced from the results of the C-AFM analysis that the area of F1 of this RS cell varies along the thickness direction. These XTEM results are consistent with the speculation obtained from the C-AFM analysis, although the exact shape of F1 could not be clarified.

It should be noted that the filaments in this study includes a considerable amount of Pt. During the forming, a significant amount of Joule heat may be generated by a large current (more than hundreds of μA) and cause intermixing between NiO and Pt [21] as well as the reduction of NiO. Consequently, the TEM analysis demonstrated that, in this study, conductive filaments in NiO consist of reduced NiO with an inclusion of a TE material (Pt). The intermixing between NiO and Pt may be suppressed if current during the forming is reduced properly.

4.6 Discussion

Although the filaments were directly observed and their chemical composition was clarified in this chapter, clear relationship between cell-resistance and the size and/or shape of the filaments could not be obtained. Due to cell deformation during the forming, it was difficult to elucidate detailed shape and size of the filaments. In addition, filaments included considerable amount of Pt, which result from the intermixing of an electrode material. This may not be the intrinsic property of filaments, taking into account that NiO-based cells exhibit an RS phenomenon using even different electrode materials [22]. Therefore, cell deformation during the forming should be suppressed to investigate the properties of filaments in detail and their relationship between cell resistance. In addition, forming current should be reduced to suppress an intermixing of an electrode material.

It has been concluded that the variation in R_{LRS} arises from the variation of the size of the filaments in the R_{LRS} range 10–220 Ω. However, R_{LRS} in the range is too small for practical use.

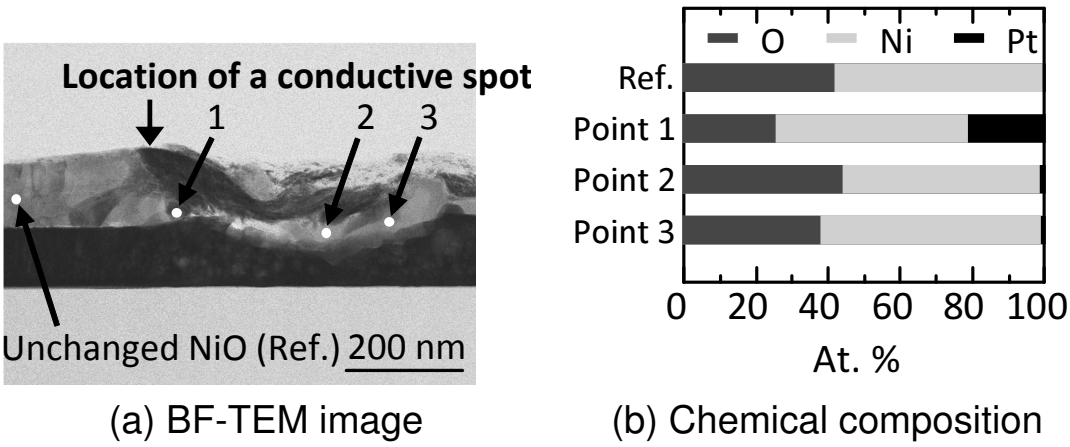

Figure 4.9: (a) Magnified image of left side of same cross section in Fig. 4.8 (b). Each white dot indicates the position analyzed by EDX. (b) Chemical composition of each point.

In addition, the validity of the model for R_{LRS} variation proposed in this chapter is limited to low R_{LRS} range, because state-of-the-art RS cells even exhibit R_{LRS} larger than 1 MΩ [23], for which equation (4.1) gives an unphysical result that a filament diameter becomes of the order of an atomic radius (∼ 1 Å). There should be a turning point that the origin of the variation in R_{LRS} changes from the variation in the size and shape of the filaments to the resistivity or conduction characteristics of the filaments. Hence, it is necessary to obtain large R_{LRS} to investigate these conduction properties of filaments in detail.

4.7 Summary

Conductive filaments formed in RS cells were directly detected by C-AFM after the removal of TEs. The area and current of the filaments were investigated in detail by C-AFM. There are several kinds of filaments that show a significant difference in current. By measuring RS cells with various R_{LRS} values, it has been revealed that the variation in R_{LRS} in the range of 10–220 Ω arises principally from the differences in the size and shape of filaments. The resistivity of the filaments mainly determining R_{LRS} was estimated to be about 40 Ωcm. From the relationship between the areas of the filaments and R_{LRS}, the shape of the filaments was also discussed. It was suggested that the area of the filaments can vary along the thickness direction depending on their location. XTEM and EDX analyses were also carried out on a filament that dominantly determines R_{LRS}. The cross-sectional area of the filament significantly varied along the thickness direction, as speculated from C-AFM analysis. It has been demonstrated that the filaments observed in this chapter consist of reduced NiO, into which a TE material (Pt) was included owing to Joule heating induced by the current during the forming.

References

[1] B. J. Choi, D. S. Jeong, S. K. Kim, C. Rohde, S. Choi, J. H. Oh, H. J. Kim, C. S. Hwang, K. Szot, R. Waser, B. Reichenberg, and S. Tiedke, J. Appl. Phys. **98**, 033715 (2005).

[2] J.-B. Yun, S. Kim, S. Seo, M.-J. Lee, D.-C. Kim, S.-E. Ahn, Y. Park, J. Kim, and H. Shin, Phys. Status Solidi (RRL) **1**, 280 (2007).

[3] S. C. Chae, J. S. Lee, S. Kim, S. B. Lee, S. H. Chang, C. Liu, B. Kahng, H. Shin, D.-W. Kim, C. U. Jung, S. Seo, M.-J. Lee, and T. W. Noh, Adv. Mater. **20**, 1154 (2008).

[4] R. Münstermann, J. J. Yang, J. P. Strachan, G. Medeiros-Ribeiro, R. Dittmann, and R. Waser, Phys. Status Solidi (RRL) **4**, 16 (2010).

[5] F. Nardi, D. Deleruyelle, S. Spiga, C. Muller, B. Bouteille, and D. Ielmini, J. Appl. Phys. **112**, 064310 (2012).

[6] D. Deleruyelle, C. Dumas, M. Carmona, C. Muller, S. Spiga, and M. Fanciulli, Appl. Phys. Express **4**, 051101 (2011).

[7] Z. Wei, T. Takagi, Y. Kanzawa, Y. Katoh, T. Ninomiya, K. Kawai, S. Muraoka, S. Mitani, K. Katayama, S. Fujii, R. Miyanaga, Y. Kawashima, T. Mikawa, K. Shimakawa, and K. Aono, *2011 IEEE Int. Electron Devices Meet.* (2011) p. 31.4.1.

[8] J. P. Strachan, M. D. Pickett, J. J. Yang, S. Aloni, A. L. D. Kilcoyne, G. Medeiros-Ribeiro, and R. S. Williams, Adv. Mater. **22**, 3573 (2010).

[9] D.-H. Kwon, K. M. Kim, J. H. Jang, J. M. Jeon, M. H. Lee, G. H. Kim, X.-S. Li, G. Park, B. Lee, S. Han, M. Kim, and C. S. Hwang, Nature Nanotechnology **5**, 148 (2010).

[10] F. Miao, J. P. Strachan, J. J. Yang, M. Zhang, I. Goldfarb, A. C. Torrezan, P. Eschbach, R. D. Kelley, G. Medeiros-Ribeiro, and R. S. Williams, Adv. Mater. **23**, 5633 (2011).

[11] G.-S. Park, X.-S. Li, D.-C. Kim, R.-J. Jung, M.-J. Lee, and S. Seo, Appl. Phys. Lett. **91**, 222103 (2007).

[12] H. Kondo, M. Arita, T. Fujii, H. Kaji, M. Moniwa, T. Yamaguchi, I. Fujiwara, M. Yoshimaru, and Y. Takahashi, Jpn. J. Appl. Phys. **50**, 081101 (2011).

[13] S. Seo, M. J. Lee, D. H. Seo, E. J. Jeoung, D.-S. Suh, Y. S. Joung, I. K. Yoo, I. R. Hwang, S. H. Kim, and I. S. Byun, J.-S. Kim, J. S. Choi, and B. H. Park, Appl. Phys. Lett. **85**, 5655 (2004).

[14] K. Tsunoda, Y. Fukuzumi, J. R. Jameson, Z. Wang, P. B. Griffin, and Y. Nishi, Appl. Phys. Lett. **90**, 113501 (2007).

[15] H. Shima, F. Takano, H. Akinaga, Y. Tamai, I. H. Inoue, and H. Takagi, Appl. Phys. Lett. **91**, 012901 (2007).

[16] I. Kondo, T. Yoneyama, O. Takenaka, and A. Kinbara, J. Vac. Sci. Technol. A **10**, 3456 (1992).

[17] R. Muenstermann, T. Menke, R. Dittmann, and R. Waser, Adv. Mater. **22**, 4819 (2010).

[18] H. Schroeder, R. Pandian, and J. Miao, Phys. Status Solidi (a) **208**, 300 (2011).

[19] P. De Wolf, T. Clarysse, and W. Vandervorst, J. Vac. Sci. Technol. B **16**, 320 (1998).

[20] J. J. Yang, F. Miao, M. D. Pickett, D. A. A. Ohlberg, D. R. Stewart, C. N. Lau, and R. S. Williams, Nanotechnology **20**, 215201 (2009).

[21] F.-H. Lu, M. L. Newhouse, R. Dieckmann, and J. Xue, Solid State Ionics **75**, 187 (1995).

[22] C. B. Lee, B. S. Kang, A. Benayad, M. J. Lee, S.-E. Ahn, K. H. Kim, G. Stefanovich, Y. Park, and I. K. Yoo, Appl. Phys. Lett. **93**, 042115 (2008).

[23] F. Nardi, D. Ielmini, C. Cagli, S. Spiga, M. Fanciulli, L. Goux, and D. J. Wouters, Solid-State Electron. **58**, 42 (2011).

Chapter 5

Influences of Structural Properties of NiO Films on Forming Characteristics

5.1 Introduction

As discussed in Chapter 4, deformation of a resistive switching (RS) cell during the forming should be suppressed and the resistance in the low-resistance state (LRS), R_{LRS}, should be increased. Current overshooting above the current limit of a measuring instrument can take place during the forming and set processes, because the switching speeds during the forming and set processes are too fast for the measuring instruments to prevent the current from overshooting [1–3]. In addition, current overshooting becomes larger when the forming or set voltage (V_{Form} or V_{Set}) become larger [2]. Large current overshooting can cause the oxide material and/or the electrode material to melt [4], resulting in deformation of the RS cell. It has been reported that the R_{LRS} is inversely proportional to the current limit during the set process, if the current overshoot is negligible in comparison with the current limit of the measuring instrument [5, 6]. The V_{Form} of the RS cells in Chapter 4 was more than 5 V, which was larger than the V_{Set}, as shown in the typical current-voltage (I–V) characteristics in Fig. 5.1. After forming, the R_{LRS} became small, irrespective of the current limit of the measuring instrument, because of the substantial current overshooting during the forming. Therefore, reduction of the V_{Form} is effective at suppressing cell deformation, as well as the excessive decrease in the R_{LRS}.

The forming is a similar process to dielectric breakdown of a gate oxide in a metal-oxide-semiconductor field-effect transistor (MOSFET) [7, 8], where the origin of the filaments is related to lattice defects, as discussed in Chapter 3. Therefore, to reduce the V_{Form}, two possible strategies were considered: reducing the thickness of the nickel oxide (NiO) film, or altering the properties of the NiO film. If the film thickness is reduced, the resistance in the initial state (R_{Ini}) of the RS cell also decreases. To increase the R_{LRS}, reducing the thickness of the NiO film was not an appropriate approach for reducing the V_{Form} because the upper limit of the R_{LRS} is determined by the R_{Ini}. Hence, the latter approach was adopted in this study. Several studies aiming at reducing the V_{Form} by altering the properties of the oxide film have been reported. In RS cells based on

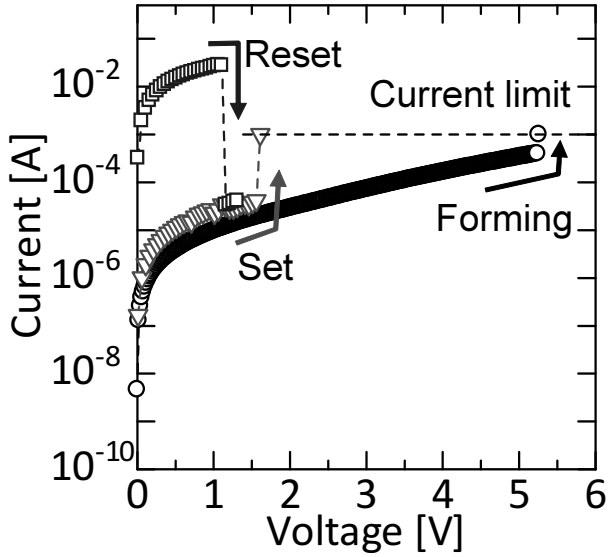

Figure 5.1: Typical *I*–*V* characteristics of an RS cell with a diameter of 50 μm, fabricated under the conditions described in Chapter 4.

hafnium dioxide (HfO_2), it was reported that the initial state of the RS cells became equivalent to the LRS, when titanium (Ti) was inserted between the HfO_2 and the electrode material of titanium nitride (TiN), followed by annealing [9]. Another study on HfO_2-based RS cells reported that the V_{Form} could be reduced by high-temperature and high-pressure hydrogen (H_2) annealing [10]. Although these studies provided the methods used to reduce the V_{Form}, influences from the oxide-film properties, such as the chemical composition and crystalline properties, on the V_{Form} are still unclear.

As mentioned above, the R_{Ini} should be large enough to increase the R_{LRS}. The NiO-film resistivity, which determines the R_{Ini}, is influenced by the film properties, as discussed in Chapter 3. In addition, it was revealed that the NiO films sputtered under a low oxygen (O_2) pressure contained a Ni metallic phase, which was examined by X-ray photoelectron spectroscopy. The microstructures, such as grain shapes (columnar or granular) and grain boundaries, may influence the NiO-film resistivity. Nevertheless, investigations of the microstructure and its influence on the electrical properties of NiO films are rare.

In this chapter, various NiO films were prepared by varying the deposition conditions, and influence of their properties on the R_{Ini} and V_{Form} were investigated. First, the conditions that were controlled during deposition as well as the determination of the other fixed conditions are discussed in Section 5.2. After that, the effects of the microstructure of the NiO films on the R_{Ini} are described in Section 5.3. Then, the factor that determines the V_{Form} is investigated from the viewpoints of the chemical composition and the crystalline properties of the NiO films. Finally, reduction of the V_{Form} was achieved while maintaining a sufficient large R_{Ini} (Section 5.5), which enabled the R_{LRS} to increase and reduced the operation current.

5.2 Optimization of the Conditions for NiO-Film Deposition

The important conditions that influence the film properties during sputtering are; the O_2-flow rate, the substrate temperature (T_{sub}), the deposition rate (and thus the input power), and the total gas pressure. A model of reactive sputtering, called "Berg's model," has been proposed [11, 12]. According to Berg's model, the O_2-flow rate directly affects the chemical composition, as long as it is controlled within a metal mode [12]. Thus, this may be the most straightforward way to alter the film properties. The T_{sub} and the deposition rate can influence, not only chemical composition, but also the crystalline properties, such as the grain size and the crystalline orientation [13, 14], which can also affect the R_{Ini} and V_{Form}. As a result, interpretation of the relationship between the film properties and the V_{Form} can become complicated when the T_{sub} and deposition rate are varied. The total gas pressure should also be kept sufficiently low since a high pressure degrades the surface morphology because of the increase in the scattering of the sputtered atoms by gas species [15]. Therefore, the O_2-flow rate was adopted as a parameter for altering the NiO-film properties, while all other conditions were fixed. Among the deposition conditions, the bottom electrodes and T_{sub}, which significantly influenced the crystalline properties of the NiO films,

were optimized to reduce the V_{Form} and the surface roughnesses of the NiO films.

5.2.1 Experimental procedure

Bottom electrodes (BEs) were platinum (Pt) with a thickness of 100 nm deposited on the SiO_2/Si substrates with a 5 nm-thick-Ti insertion layer. The BEs were deposited by either sputtering or by electron beam (EB) evaporation. Hereafter, in Section 5.2, sputter-deposited BE and EB-evaporated BE are denoted as BE(SPT) and BE(EB), respectively. Sputtering was carried out using the system ES-250 Eiko at room temperature (RT) in an argon (Ar) atmosphere, while the pressure was maintained at 0.25 Pa. The deposition rate of Pt was about 10 nm/min. EB evaporation was carried out at RT using the system ANELVA L-043E and the deposition rate of Pt was about 4.8 nm/min. After deposition of the BEs, NiO films were deposited on top at T_{sub} of 623 K. During deposition, the total gas-flow rate, the O_2-flow rate, and the total gas pressure were t 9 sccm, 1.1 sccm and 0.6 Pa, respectively. The deposition rate of the NiO films was about 42 nm/min.

The NiO films were also deposited on BE(SPT) under various T_{sub} ranging from RT to 873 K, where all of the conditions were kept the same as above, except for the T_{sub}.

The crystalline properties of the BE and NiO films were evaluated by X-ray diffraction (XRD) and atomic force microscopy. For the NiO films deposited with different T_{sub}, the V_{Form} was determined from the I–V measurements in a Pt (100 nm)/NiO/BE (SPT) structure, where the top electrodes (TEs) had a diameter of 50 μm. The NiO thicknesses used for the I–V and AFM measurements were about 90 nm, while a thickness of about 640 nm was adopted for XRD to obtain a sufficient diffraction intensity.

5.2.2 Bottom electrode

Figure 5.2 shows XRD $2\theta/\omega$-scans of a NiO film deposited on (a) BE(SPT) and (b) BE(EB). The intensity was normalized by the intensity of the direct beam. Comparing the overall intensities of the Pt and NiO films, a stronger intensity was obtained in the sample with BE(SPT). In addition, both Pt and NiO were highly $\langle 111 \rangle$ oriented in the sample with BE(SPT). It has been reported that a sputter-deposited Pt film on a SiO_2/Si substrate with a Ti adhesion layer tended to exhibit a $\langle 111 \rangle$ orientation [16]. In the sample with BE(EB), peaks associated with the $\{200\}$ and $\{220\}$ planes were observed besides those with $\{111\}$ and $\{222\}$ planes, although the peak associated with the $\{111\}$ plane was the most intense peak. Therefore, crystals composing a film in the sample with BE(EB) had a more or less random orientation. NiO and Pt had the same orientation for both the BE(SPT) and BE(EB). In the initial stage of film deposition, nucleation preferentially occurred along the orientation that minimized the surface energy between the film and the substrate. The same orientation between the NiO and Pt may be the result of minimizing the energy at the interface between NiO and Pt because both NiO and Pt had a face-centered-cubic (FCC) structure.

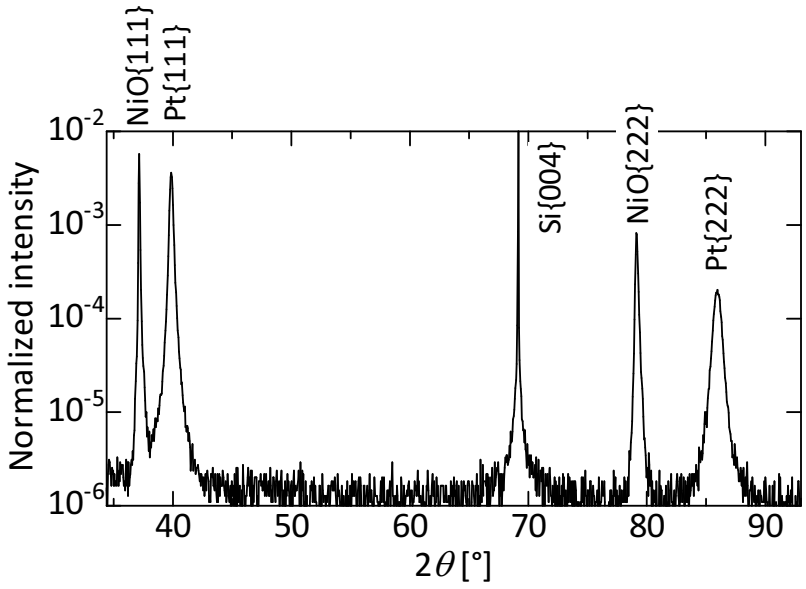

(a) NiO film on BE deposited by sputtering

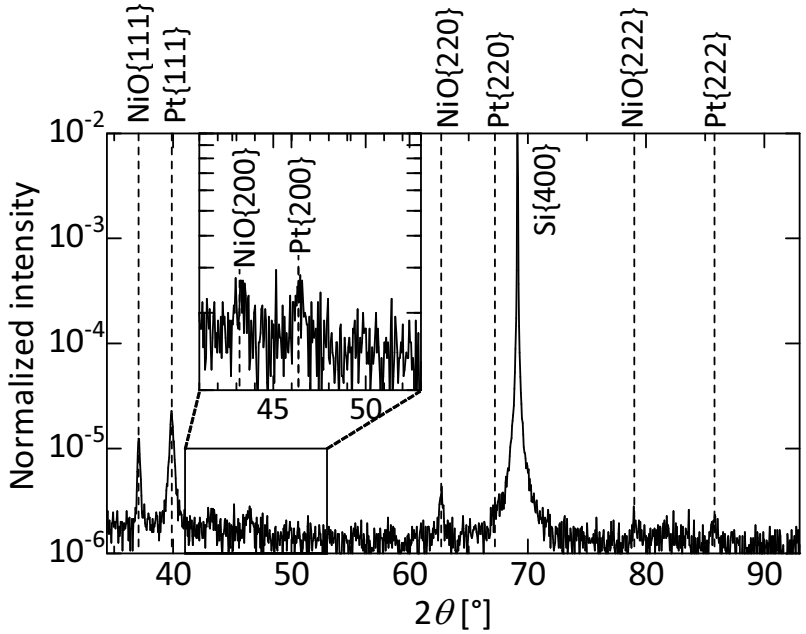

(b) NiO film on BE deposited by EB evaporation

Figure 5.2: XRD $2\theta/\omega$-scans of NiO/BE/sub. stack samples, in which BE was deposited by (a) sputtering and (b) EB evaporation.

Figure 5.3 shows the surface topology of the NiO layers deposited on (a) BE(SPT) and (b) BE(EB). The scan area was 5×5 μm^2. NiO on BE(SPT) displayed a smooth surface, whereas many cracks appeared in the NiO layer on BE(EB). The appearance of cracks in the NiO on BE(EB) may be ascribed to the thermal stress originating from the difference in the coefficient of thermal expansion (CTE) between the substrate (SiO_2/Si) and the BE and/or between the BE and the NiO layer. The lower mechanical strength of BE(EB) compared with BE(SPT) may be the reason why the cracks appeared only in the sample with BE(EB). BE(EB) was not appropriate for NiO deposition at elevated temperatures because of the occurrence of cracks. In addition, BE(SPT) was more suitable for investigation of the influences of the crystalline properties of NiO films on their electrical properties, because the NiO films deposited on BE(SPT) were highly ⟨111⟩-oriented and no other peaks associated with other planes were observed, which may enable a straightforward interpretation the relationship between the crystalline and electrical properties of NiO films.

5.2.3 Substrate temperature during NiO-film deposition

Figure 5.4 shows the surface topology of NiO films deposited on BE(SPT) at different T_{sub}. The scan area was 500×500 nm^2. Values of the root-mean-square (RMS) roughness are also described in the figures. The large surface roughness causes local fluctuations in the film thickness, which may cause electric field crowding, both of which affect the V_{Form}. Therefore, the surface roughness should be sufficiently small compared with the NiO-film thickness. When $T_{sub} \leq 523$ K, grains with diameters of 20–40 nm were observed. When $T_{sub} = 623$ K, the surface became slightly smoother than that for $T_{sub} \leq 523$ K and the boundaries between the grains appeared to be unclear compared with the samples with $T_{sub} \leq 523$ K. Although the RMS roughness slightly decreased with an increase in T_{sub} for $T_{sub} \leq 623$ K, it was within the range of 0.93–0.61 nm and the peak to peak values were about 5 nm, which is small compared with the NiO-film thickness (90 nm). In contrast, when T_{sub} was increased to 723 K, the surface roughness was remarkably increased to 1.2 nm, as depicted in Fig. 5.4 (e). In addition, protrusions with diameters of 30–60 nm and heights of 20–50 nm were observed. The RMS roughness value presented in Fig. 5.4 (e) was taken in the region without these protrusions. For $T_{sub} = 873$ K, the surface roughness and the grain size further increased, as shown in Fig. 5.4 (g). The peak to peak value of the surface topology was more than 50 nm, which is about half of the NiO-film thickness.

Fig. 5.5 shows V_{Form} plotted against T_{sub} during NiO-film deposition. When the NiO films were deposited at different T_{sub}, V_{Form} significantly varied in the range of 1.7–20 V. V_{Form} was highest when deposited at 423 K, while the lowest V_{Form} was obtained at $T_{sub} = 723$ K. Among these samples, the NiO films deposited at 623 K and 723 K exhibited a V_{Form} below 3 V.

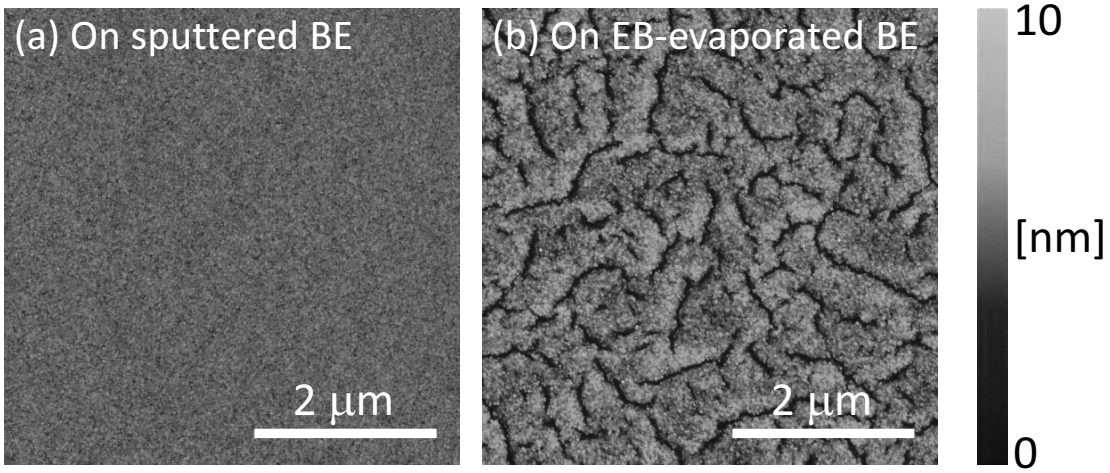

Figure 5.3: AFM topological images of NiO films deposited at 623 K on (a) sputtered BE and (b) EB with an evaporated BE. The scan areas are 5×5 μm^2.

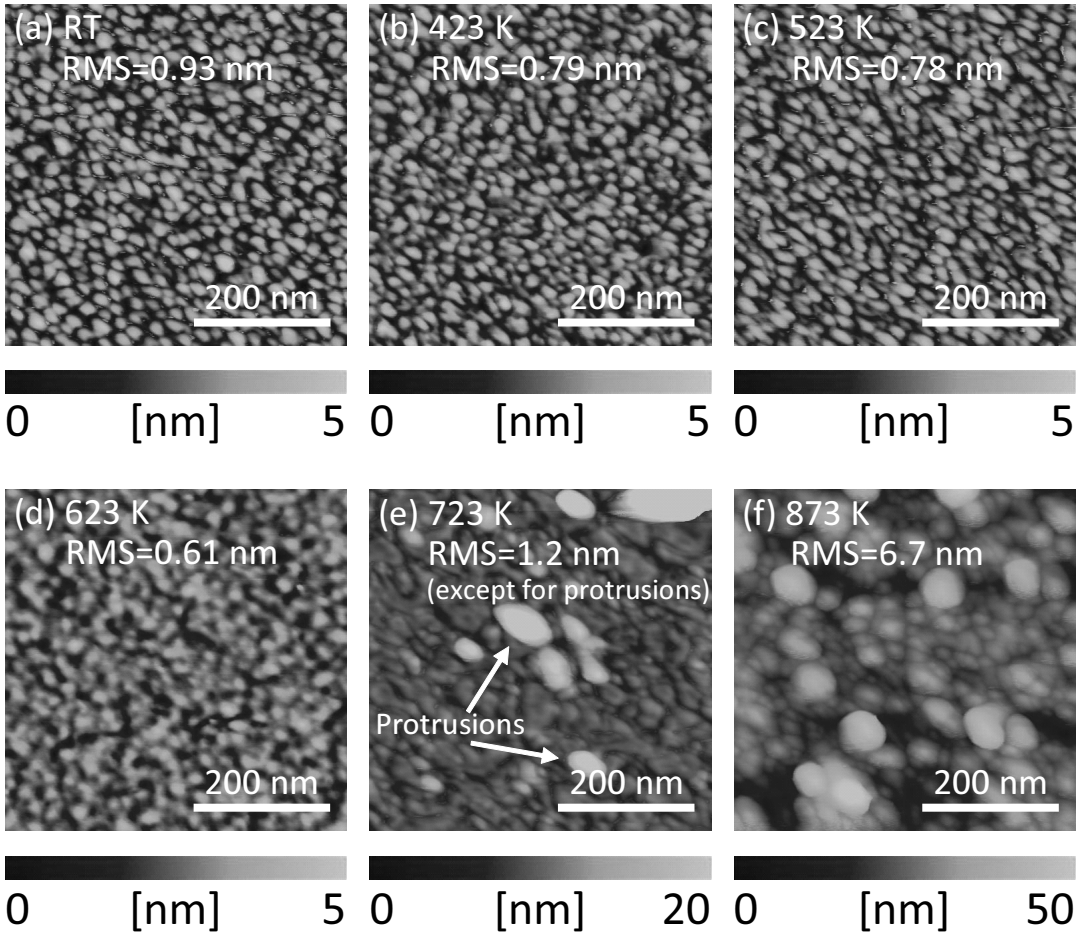

Figure 5.4: Topologies of NiO films deposited with an O_2-flow rate of 1.1 sccm at (a) RT, (b) 423 K, (c) 523 K, (d) 623 K, (e) 723 K, and (f) 873 K. The scan areas are 500 × 500 nm^2. Note that the z scale is different in each figure. The RMS roughnesses are presented in each figure. The RMS roughness at (e) 723 K was taken for the region where protrusions on the surface were excluded.

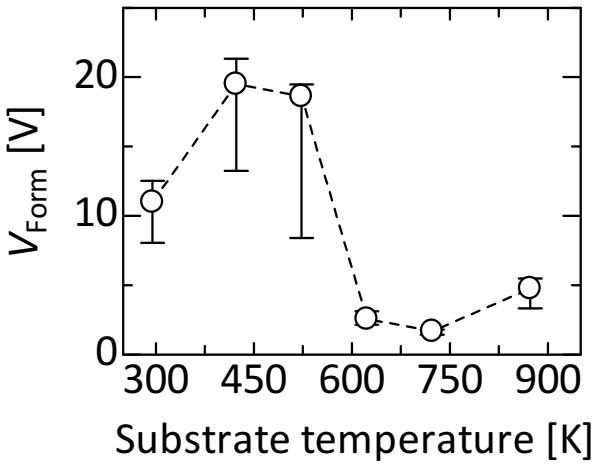

Figure 5.5: Dependence of the forming voltage on the substrate temperature during NiO deposition. BE was deposited by sputtering and the O_2-flow rate during NiO deposition was 1.1 sccm.

5.2.4 Discussion

Topological change with T_{sub}

The NiO surface topology significantly changed in the T_{sub} range from 623 K to 873 K. When T_{sub} was increased, the surface topology was influenced by the enhancement of the diffusion of species (Ni atoms or NiO molecules) adsorbed on the substrate until nucleation, and there were topological changes in the BE when the substrates were heated. Fig. 5.6 shows the surface topology of Pt on BE(SPT) after a heat treatment at different temperatures. For $T < 723$ K, the grain size of Pt was almost unchanged compared with the as-deposited sample, while at 873 K, the grain size significantly increased. Therefore, the topological changes in the NiO films between 623 K and 723 K were mainly caused by enhancement of the surface diffusion of adatoms during deposition. At 873 K, in addition to further surface diffusion of NiO, the increase in the grain size of BE(SPT) also influenced on the resultant topology of the NiO films.

Adopted deposition conditions

Sputtered films were adopted based on the discussions in Section 5.2.2 for the bottom electrode. With respect to T_{sub}, as described above, the surface roughness should be small compared with the NiO-film thickness, to investigate the V_{Form}. In addition, the conditions under which a low V_{Form} was obtained should be adopted. Although the RS cells with NiO deposited at T_{sub} =723 K exhibited the smallest V_{Form}, protrusions with heights of 20–50 nm appeared. Therefore, T_{sub} =623 K is promising from the viewpoint of the surface roughness as well as the reduction in the V_{Form}. As a consequence, a T_{sub} of 623 K and a sputtered BE were adopted for deposition of the NiO films.

5.3 Microstructure of NiO Films and Its Influences on Initial Resistance

5.3.1 Experimental procedure

Various NiO films were deposited on Pt (100 nm)/Ti (5 nm)/SiO_2/Si substrates by varying the O_2-flow rate from 0.9 to 1.3 sccm, while the total gas-flow rate and the total pressure were maintained at 9 sccm and 0.6 Pa, respectively. The substrate temperature during NiO deposition was 723 K and a BE of Pt/Ti was deposited by sputtering using the optimized conditions in Section 5.2. The deposition rate of the NiO films was about 42 nm/min, which was almost independent of the O_2-flow rate. Hereafter, a NiO film deposited with an O_2-flow rate of X sccm is denoted as NiO(X).

The chemical composition and crystalline properties of the NiO films were characterized by Rutherford backscattering spectrometry (RBS) and XRD, respectively. The film structure and chemical composition on the microscopic scale were analyzed by plan-view transmission elec-

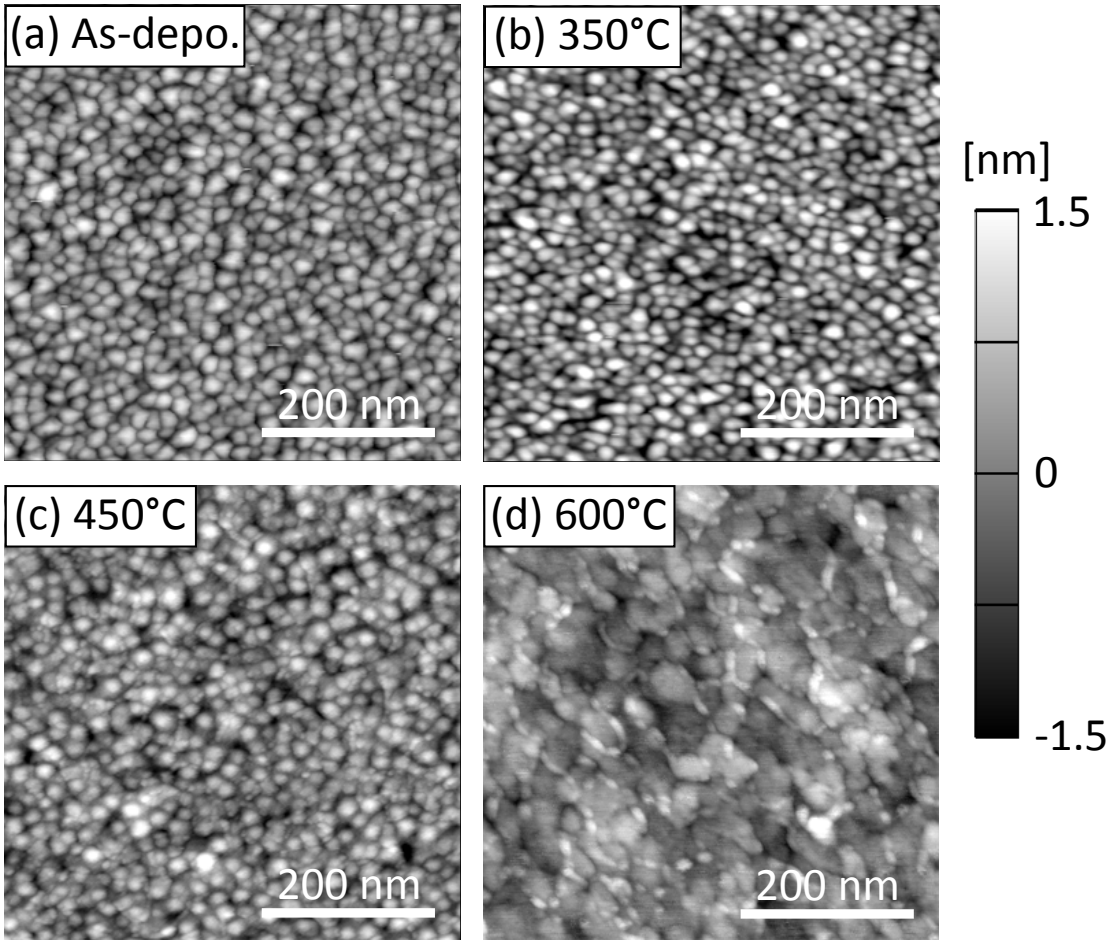

Figure 5.6: (a) Surface topology of Pt films deposited by sputtering at RT. Topology of Pt films after a heat treatment at (b)623 K, (c) 723 K, and (d) 873 K. The scan area is 500 × 500 nm^2. A significant increase in the grain size was observed after heat treatment at (d) 873 K.

tron microscopy (TEM) and energy-dispersive X-ray spectrometry (EDX). Electrical measurements were carried out in the RS cells with a Pt/NiO/Pt stack structure and a diameter of 50 μm, formed by evaporating a 100 nm-thick Pt film on the NiO layer. The resistivity of the NiO films was determined from the resistance of the RS cells, measured using a two-terminal method. The electrical properties of the NiO films, on the microscopic scale, were also characterized by conductive-AFM (C-AFM), in which a platinum-iridium (PtIr) coated probe with a tip radius of 20 nm was used. The thickness of the NiO films were about 90 nm for RBS, TEM, electrical measurements, and C-AFM, and about 640 nm for XRD.

5.3.2 Resistivity and structural properties of NiO films

Resistivity of NiO films

The resistivity in the initial state of the NiO films was plotted against the O_2-flow rate during the NiO deposition in Fig. 5.7, where the resistivity was calculated from the resistance of the RS cells when a bias voltage of 0.1 V was applied. When the O_2-flow rate was 1.1 sccm or less, the resistivity decreased with a decreasing O_2-flow rate, while it was nearly constant in the range of $6 - 7 \times 10^5$ Ωcm for O_2-flow rates of 1.1 sccm and above. As shown in Fig. 5.7, remarkable changes in the resistivity were observed for NiO films deposited under low O_2-flow rates in the range of 0.9-1.1 sccm.

Chemical composition and crystalline structure

Figure 5.8 shows the oxygen composition of the NiO films (x in NiO_x) plotted against the O_2-flow rate during NiO deposition. While NiO(0.9) had a Ni-rich composition of $NiO_{0.93}$, the NiO films had an O-rich composition for $O_2 \geq 1.0$ sccm, where x was almost saturated at a value of 1.13. Figure 5.9 shows XRD $2\theta/\omega$-scans of the prepared samples. In all of the samples, both Pt and NiO exhibited an orientation in the $\langle 111 \rangle$ direction. In addition, a Ni$\{111\}$ phase also existed in NiO(0.9), indicating that the excess Ni existed as a metallic phase in NiO(0.9).

TEM observations

TEM observations were conducted on NiO(1.0) and NiO(1.1) to investigate the microscopic film structures. The chemical compositions of the local regions were analyzed by EDX. Plan-view TEM images of (a), (b) NiO(1.0) and (c), (d) NiO(1.1) are shown in Fig. 5.10. Figure 5.10 (a), (c) and (b), (d) show bright-field (BF) and high-angle annular dark-field (HAADF) images, respectively. As depicted in Fig. 5.10 (a) and (c), both NiO(1.0) and NiO(1.1) were composed of grains with diameters of tens of nm (data not shown). In addition, NiO(1.1) had a columnar structure, which was revealed by cross-sectional TEM. NiO(1.0) may also have a columnar structure. The HAADF images displayed a different appearance between NiO(1.0) and NiO(1.1). Bright regions were observed at the grain boundaries (GBs) in NiO(1.0), circled in Fig. 5.10(b), but they were not observed in NiO(1.1). Since the brighter regions in the HAADF images indicate a larger

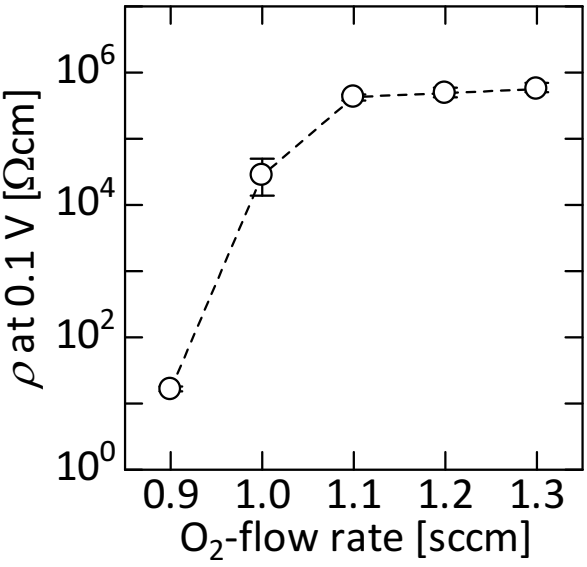

Figure 5.7: Resistivity of NiO films in the initial state plotted against the O_2-flow rate during NiO deposition.

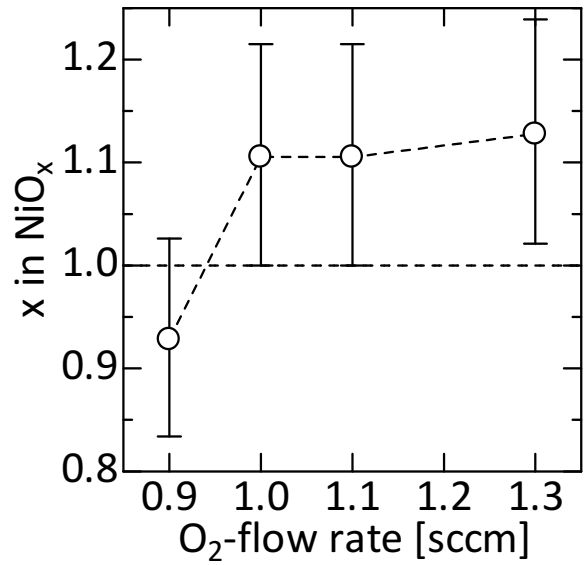

Figure 5.8: Oxygen composition of NiO films plotted against the O_2-flow rate during deposition.

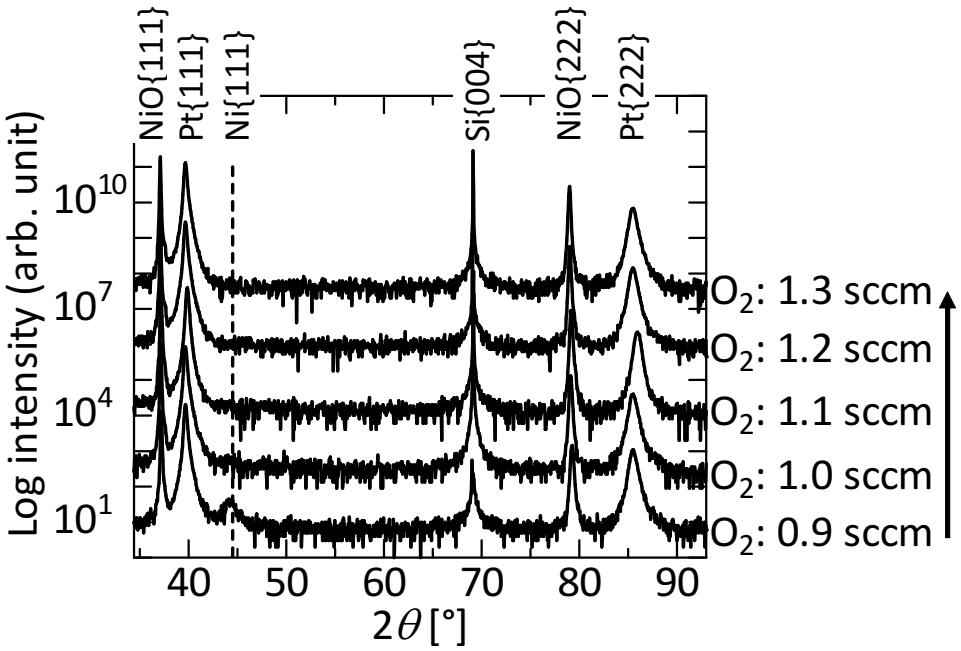

Figure 5.9: XRD $2\theta/\omega$-scans of prepared samples, where the NiO films were deposited with different O_2-flow rates ranging from 0.9 to 1.3 sccm.

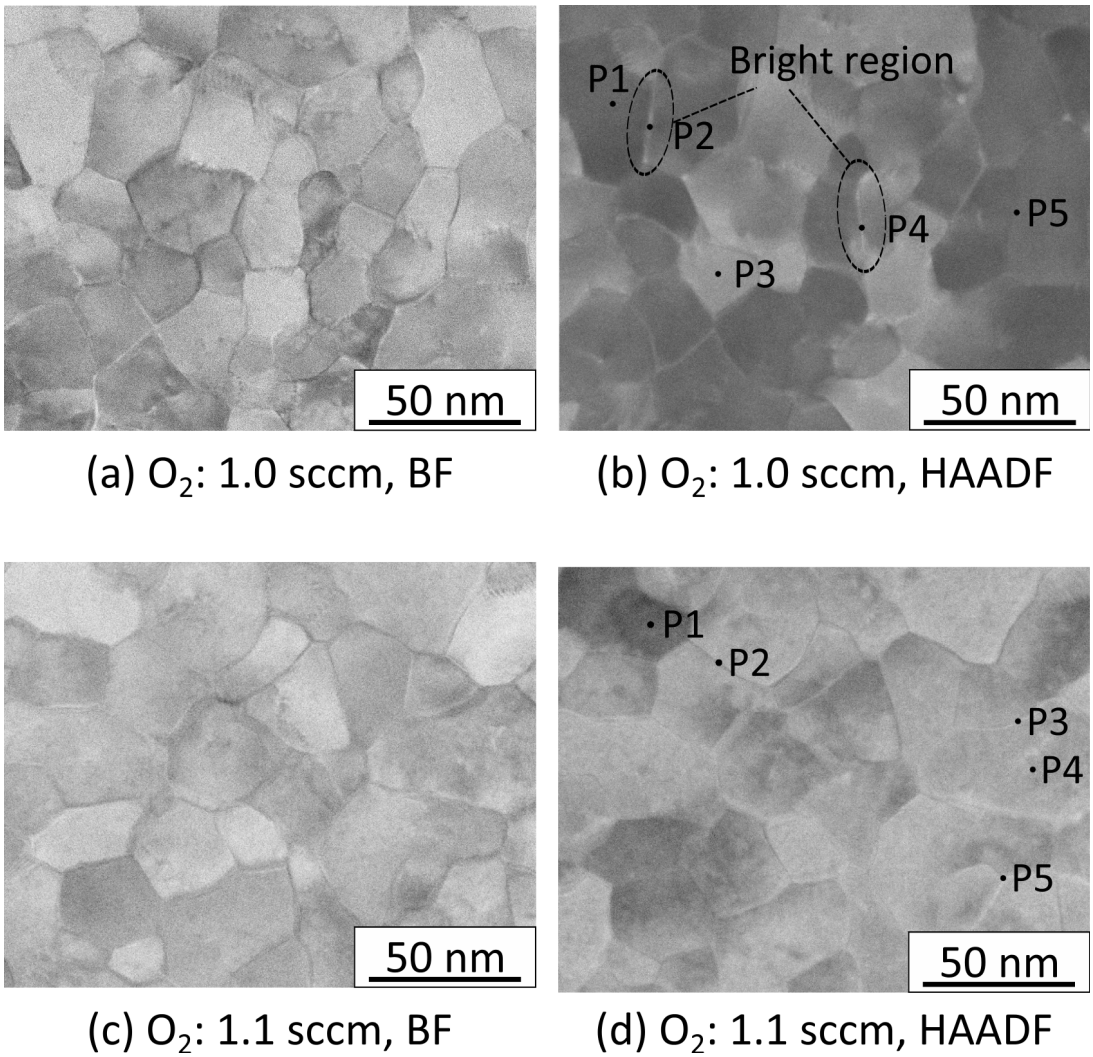

Figure 5.10: Plan-view TEM images of NiO films deposited with O_2-flow rates of (a) and (b) 1.0 sccm and (c) and (d) 1.1 sccm. (a) and (c) are bright-field and (b) and (d) are high-angle-annular-dark-field images. The points where the chemical compositions were analyzed are depicted in (b) and (d).

atomic mass, it is suggested that the brighter regions at the GBs had a Ni-rich composition compared with the grains. The chemical composition near the points indicated in Fig. 5.10 (b) and (d) were examined by EDX. The results are summarized in Table 5.1, which shows that the GBs (P2 and P4) in NiO(1.0) had a lower oxygen (Ni-rich) composition than the grains, while such Ni-rich regions were not observed in NiO(1.1), even at the GBs. Ni-rich regions at the GBs were not always observed in NiO(1.0) [for example P5 in Fig. 5.10 (b)]. NiO(0.9) had a higher Ni excess composition than NiO(1.0), thus, Ni-rich regions at GBs may have also existed in NiO(0.9). Taking into account that a Ni metallic phase was observed in the XRD for NiO(0.9), the excess Ni at the GBs crystallized as a Ni phase rather than as an O-deficient NiO in both NiO(0.9) and NiO(1.0), where the Ni phase segregated during the NiO deposition under the low-O_2 flow rate. The different contrast between the grains was caused by the diffraction and/or channeling contrast of the electron beam, not by the differences in the chemical composition, which was ascertained by the analysis of the chemical composition [see, P1 and P3 in Fig. 5.10 (b)]

The preferential formation of Ni segregation at GBs is discussed. The mean resident times of the adatoms are generally different between the GBs and in the grains because of the differences in the surface energies. In this study, the oxygen atoms that were adsorbed onto the substrate surfaces desorbed from the GBs more easily than from the grains. Thus, the incorporation rate of the oxygen atoms during growth was less at the GBs than in the grains. Under the O_2-deficient conditions, a Ni metallic phase was likely formed at the GBs rather than the formation of a NiO phase. As a result, Ni segregation appeared preferentially at the GBs, although further investigations on the GB structure in NiO films are necessary. Since the volume of the Ni segregation in NiO(1.0) was much smaller than that of the grains, the difference in the oxygen composition and the crystalline phase between NiO(1.0) and NiO(1.1) could not be detected.

The resistivity began to decrease when the O_2-flow rate was decreased from 1.1 to 1.0 sccm. Ni segregation was observed at the GBs in NiO(1.0), but not in NiO(1.1). Therefore, the Ni segregation at the GBs acted as electrical leakage paths and may give rise to the resistivity decrease in the NiO films deposited under O_2-deficient conditions. This is verified in the next section.

5.3.3 Identification of the electrical leakage paths in NiO films

In Section 5.3.2, it was suggested that Ni segregations at the GBs acted as electrical leakage paths. C-AFM measurements were conducted to examine the contribution of the GBs to the electrical conduction. Figure 5.11 shows images of the surface topography (left) and a current mapping (right) of (a) NiO(1.0) and (b) NiO(1.1), where a voltage of 2 V was applied to the BE while the probe was grounded. The scan area for both measurements was 500×500 nm^2. A sectional profile along the line indicated in the image is depicted in the image underneath. NiO(1.1) displayed a smoother surface topology with an RMS roughness of 0.50 nm, compared with NiO(1.0), which had an RMS roughness of 0.88 nm. In addition, no notable features were observed in NiO(1.1). In contrast, a number of narrow depressed regions (grooves) were observed in NiO(1.0). It was deduced that the location of the grooves corresponded to the locations where the Ni segregation

Table 5.1: Chemical compositions of NiO(1.0) and NiO(1.1), near the points indicated in Fig. 5.9, analyzed by EDX.

NiO(1.0)	P1	P2	P3	P4	P5
Ni [at. %]	47.5	**55.9**	46.8	**53.9**	46.5
O [at. %]	52.5	**44.1**	53.2	**46.1**	53.5

NiO(1.1)	P1	P2	P3	P4	P5
Ni [at. %]	46.3	46.1	46.8	45.3	47.7
O [at. %]	53.7	53.9	53.2	54.7	52.3

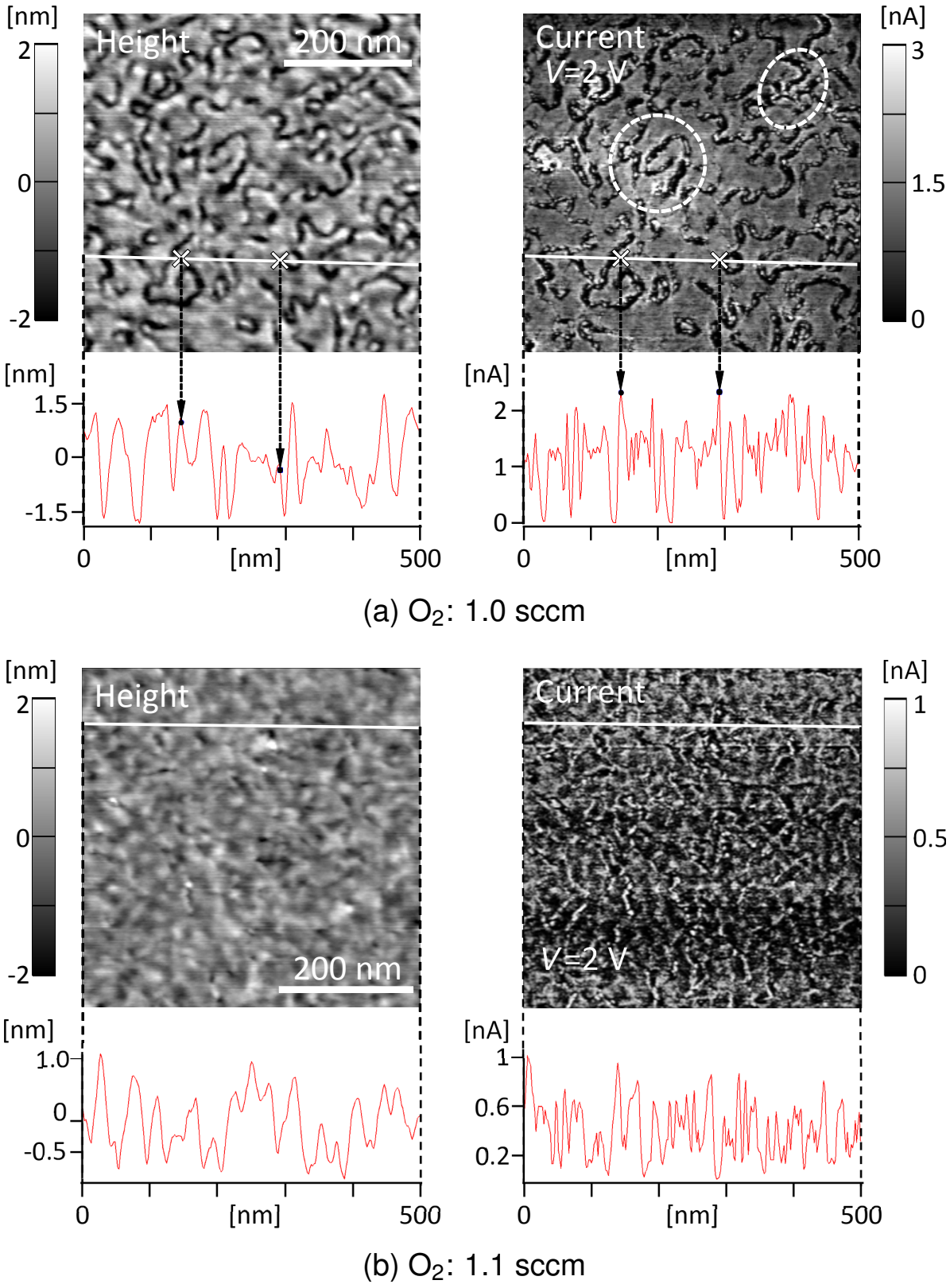

Figure 5.11: C-AFM images of NiO films deposited with (a) O_2 = 1.0 sccm and (b) O_2 = 1.1 sccm. The left and right images show the surface topology and current mapping at a bias of 2 V. The scan area is 500 × 500 nm^2.

was formed from the following reasons. The GBs generally tended to be depressed compared with the grains, to minimize the total energy by lowering the interfacial energy [17]. In this study, the interface energy of the GBs, where the Ni segregation was formed, was larger compared with that of the GBs without the Ni segregation, because of the inclusion of a material other than NiO. Therefore, by lowering the interface energy, the heights of the GBs containing the Ni segregation became smaller than those of the GBs without Ni segregation. Ni segregation in NiO(1.0) was not formed at every GB, as described in Section 5.3.2. Thus, the spatial distribution of the grooves in NiO(1.0), where the Ni segregation may have been formed, did not correspond to that in the GBs, observed by TEM (Fig. 5.10 (a)).

In NiO(1.0), an almost uniform current of about 1.3 nA was observed within the grains, while the current flowing through near the grooves or the edges of the grains was greater than 2 nA, as represented by the line profile in Fig. 5.11 (a). In particular, the regions where the grooves were crowded exhibited large currents, as circled in the image on the right in Fig. 5.11 (a). Since the Ni segregation was formed at the grooves, the current distribution indicated that the Ni segregation acted as current leakage paths in NiO(1.0). In NiO(1.1), the current flowing through the grains was in the range from 0.2 nA to 0.6 nA, which is less than the half of that through the NiO(1.0) grains. The spatial distribution of the current may be caused by the condition of the probe contact with the surface of NiO(1.1). Comparing the results between NiO(1.0) and NiO(1.1), the smaller current (larger resistance) was detected in NiO(1.1), which is consistent with the resistivity measurements in the RS cells. Combining the result for the spatial distribution of the C-AFM current in NiO(1.0) with the result where a larger current that was detected in NiO(1.0), it is concluded that the low resistivity in the NiO films deposited under the O_2-deficient condition was caused by the formation of Ni segregation, which acted as electrical leakage paths.

It is discussed that the Ni segregation at the grooves acted as leakage paths in NiO(1.0). However, the current was difficult to detect in the grooves where the Ni segregation was considered to be formed, which seemingly contradicts the argument that the Ni segregation acted as leakage paths. The reason why almost no current was detected at the grooves is explained as follows: when the probe was located just above a groove, it could not make contact directly with the Ni segregation because of the finite tip radius (≈ 20 nm), instead it could touch both sides of the grain walls across the groove. In such a situation, the contact area of the probe with a sample increased. Thus, the contact pressure of the probe decreased, which increased the contact resistance [18, 19]. An increasing voltage drop at the interface between the probe and the sample surface caused the increase in contact resistance, resulting in the decrease in the current detected at the grooves. In the scanning spreading resistance microscopy, which was an AFM-based current-sensing technique similar to C-AFM, a difference in the contact force by 3 times caused a difference in the detected resistance by more than one order of magnitude [18]. As a result, the current was difficult to detect at the grooves. Therefore, it was difficult for the current to flow at the grooves, which may be consistent with the argument that the Ni segregation acted as electrical leakage paths.

Further insight into the results for the C-AFM measurements

The C-AFM measurements showed that the Ni segregation, which acted as electrical leakage paths, gave rise to the decrease in the resistivity in the NiO films deposited under O_2-deficient conditions. Nevertheless, the current (resistance) in NiO(1.0) measured by C-AFM was several times larger (smaller) than that in NiO(1.1), while the resistivity measured with a two-terminal method in the RS cells was different by about one order of magnitude, as described in Section 5.3.2. The resistance measured by C-AFM is speculated to have been determined from the resistivity near the probe because there was a significant voltage drop near the probe contact. Therefore, the resistance may be different from that measured in the RS cells. As a result, a discrepancy in the measured resistance between the C-AFM and the two-terminal method may arise. To gain further insight into the above speculation, two-dimensional-device simulations were carried out.

The simulated structure is shown in Fig. 5.12(a). It consists of three NiO grains separated by two GBs 1.2 nm in width, at which the Ni segregation was formed. The width of the center grains, excluding the grain edges, was assumed to be 40 nm, which corresponded to the typical distance between two neighboring grooves [see the left image in Fig. 5.11(a)]. The shape of the grain edges were determined from the line profile in NiO(1.0). The widths of both sides of the grains were assumed to be 1000 nm. The width of the grains on both sides barely affected the results when they were above 100 nm. The resistivity of NiO (the center of the grain and both sides of the grains) ρ_1 was assumed to be 6.5×10^5 Ωcm, which is roughly the same as the resistivity of NiO(1.1) at 0.1 V. The bottom electrode was Pt with a resistivity of 1×10^{-5} Ωcm [20]. The resistivity at the GB (ρ_2) was assumed to be 7.2×10^{-6} Ωcm, which corresponded to the value of bulk Ni [20], and was the same as ρ_1 (6.5×10^5 Ωcm) to simulate NiO(1.0) and NiO(1.1), respectively. ρ_1 was assumed to be the same for both NiO(1.0) and NiO(1.1). The resistivity values used for the simulations are tabulated in Table 5.2. In every structure, the contact radius of the probe a was assumed to be 0.8 nm, which was estimated by Hertz theory. In the theory, a is described as:

$$a = \left[\frac{3}{4} \left(\frac{1 - \nu_{\mathrm{probe}}^2}{E_{\mathrm{probe}}} + \frac{1 - \nu_{\mathrm{NiO}}^2}{E_{\mathrm{NiO}}} \right) rF \right]^{\frac{1}{3}}, \tag{5.1}$$

where ν is the Poisson ratio, E is Young′s modulus, r the radius of the probe, and F is the contact force [21]. In this study, the probe was made of Si coated with PtIr. Hence, it was difficult to obtain the actual elastic moduli of the probe. Here, as a substitution, the values of Pt-Ir [22] were adopted. The values applied for the calculations on the (5.1) are summarized in Table 5.3. According to the C-AFM measurements, a voltage bias of 2 V was applied to the bottom electrode, while the probe was grounded. The calculations were performed in Cartesian coordinates, assuming a uniform structure along the direction perpendicular to a paper surface.

Figure 5.13 shows the simulated I–V characteristics for each configuration. In NiO(1.0), when the probe was at the edge of a grain (b), the current was about 1.2 times larger than when the probe was at the center of the grain (a). The current in (c) NiO(1.1) was about 0.8 times as large as that in (a) NiO(1.0). The distribution of the electrostatic potential for each configuration is depicted in

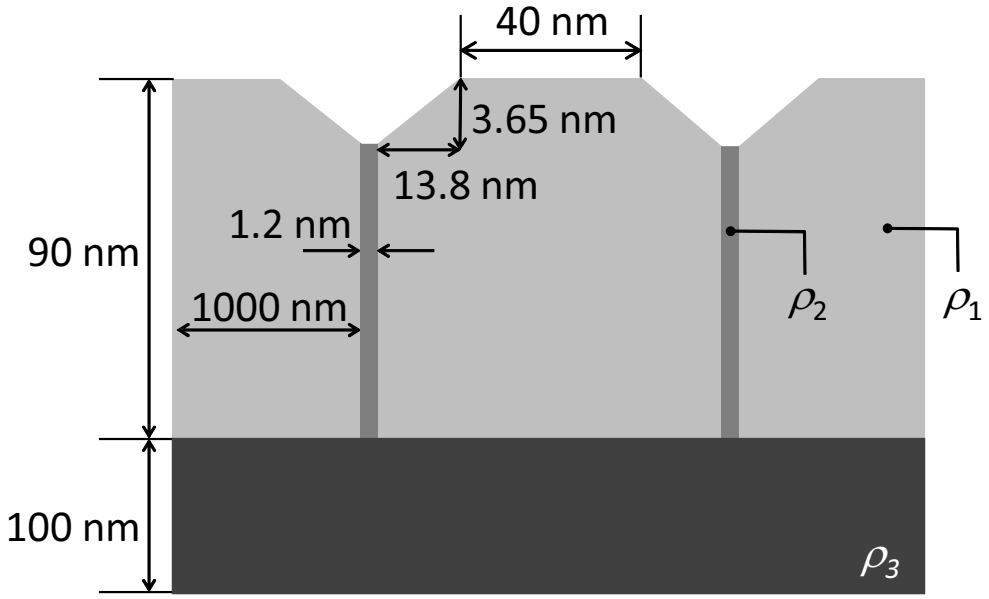

Figure 5.12: A schematic illustration of the structure on which the device simulations were conducted.

Table 5.2: Resistivity values used for the device simulations.

	ρ_1 [Ωcm]	ρ_2 [Ωcm]	ρ_3 [Ωcm]
1: NiO(1.0)	6.5×10^5	7.2×10^{-6}	10×10^{-6}
2: NiO(1.1)		6.5×10^5	

Table 5.3: Mechanical parameters used to estimate the contact radius, a.

F [nN]	4
r [nm]	20

	NiO	PtIr
E [GPa]	190	263
ν	0.320	0.346

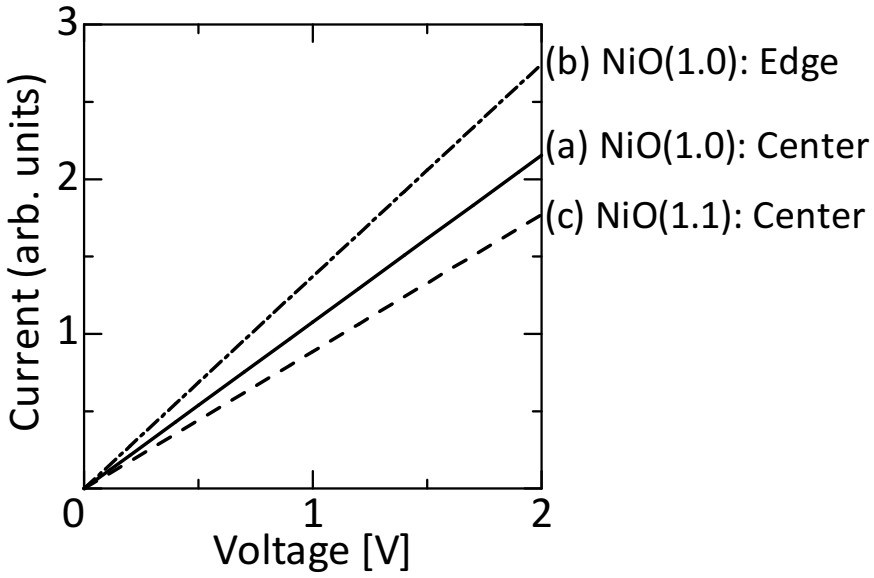

Figure 5.13: Simulated *I*–*V* characteristics under the conditions where the probe was located at (a) the grain edge of NiO(1.0), (b) the center of a NiO(1.0) grain and (c) at the center of a NiO(1.1) grain.

Fig. 5.14. More than 60% of the potential dropped off 30 nm from the probe. Therefore, the total resistance was determined from the resistivity near the probe. This is why the difference in the simulated currents between NiO(1.0) and NiO(1.1) was only 0.8 times, while ρ_2 was 10^{11} times different between them.

As demonstrated by the simulations, most of the voltage drop took place near the probe contact in the C-AFM measurements; thus, the resistance was determined from the resistivity near the probe. As a result, the current measured by C-AFM in NiO(1.0) was only double that in NiO(1.1), while the resistivity measured with the two-terminal method had one order of magnitude difference between NiO(1.0) and NiO(1.1). As the difference in the C-AFM currents between NiO(1.0) and NiO(1.1) was only double, this indicated that the resistivity of the grains was almost the same for both NiO(1.0) and NiO(1.1). This supports the idea that the Ni segregation acted as electrical leakage paths.

5.3.4 Electrical properties

In Sections 5.3.2 and 5.3.3, it was shown that the Ni segregation formed at the GBs acted as electrical leakage paths, and that it caused a decrease in the resistivity in the NiO films. In this section, the electrical properties of the Ni segregation are discussed.

Current-voltage characteristics

The *I–V* characteristics for NiO(0.9–1.1), measured at RT, are shown in Fig. 5.15, where the *I–V* curves in both the forward and reverse sweeps are plotted; that is, the voltage was swept, for example, from 0 V → 1.5 V → 0 V. The *I–V* characteristics of NiO(1.1) were nonlinear, which is typical for NiO films [23].

In contrast, the NiO(1.0) films, where most of the current flowed through the Ni segregation, exhibited unique *I–V* characteristics, as shown in Fig. 5.15 (b). The maximum bias voltage in each sweep was gradually increased as: 0.5, 1.5, 1.6, and 1.7 V. When the maximum bias voltage was below 1.5 V (0.5 V in the figure), the *I–V* characteristics were nonlinear and exhibited little hysteresis. When the bias voltage exceeded about 1.5 V, the current drastically increased and hysteresis was observed in the *I–V* characteristics; that is, the resistance decreased in the reverse sweep, compared with the forward sweep. The resistance further decreased as the maximum bias voltage was increased. The resistance changes were not reversible. After the resistance decreased, the RS cell exhibited nearly linear *I–V* characteristics.

NiO(0.9) exhibited nearly linear *I–V* characteristics, where little hysteresis was observed, as shown in Fig. 5.15 (c). The resistance of the RS cell with NiO(0.9) was about 17 Ω, which was comparable to the resistance of the BE (≈ 10 Ω). Therefore, it was difficult to extract the *I–V* characteristics specific to the Ni segregation. NiO(0.9) might have exhibited *I–V* characteristics similar to NiO(1.0), including the irreversible resistance decrease, when they were measured in an RS cell with a smaller area, thus, with a larger resistance.

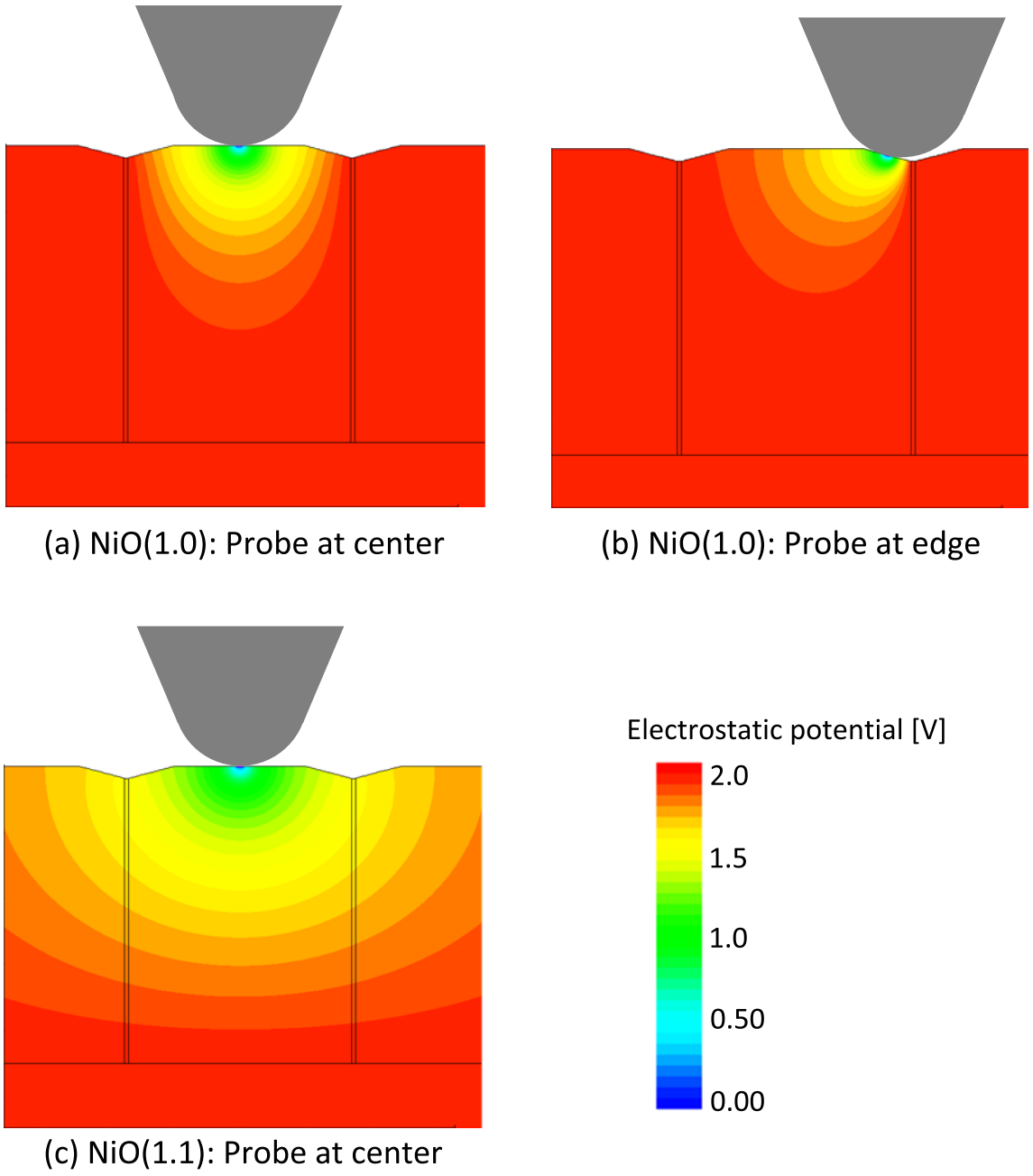

Figure 5.14: Simulated electrostatic potential distribution under the conditions where the probe was located at (a) the grain edge of NiO(1.0), (b) the center of a NiO(1.0) grain and (c) at the center of a NiO(1.1) grain. A voltage of 2 V was applied to the bottom electrode, while the probe was grounded.

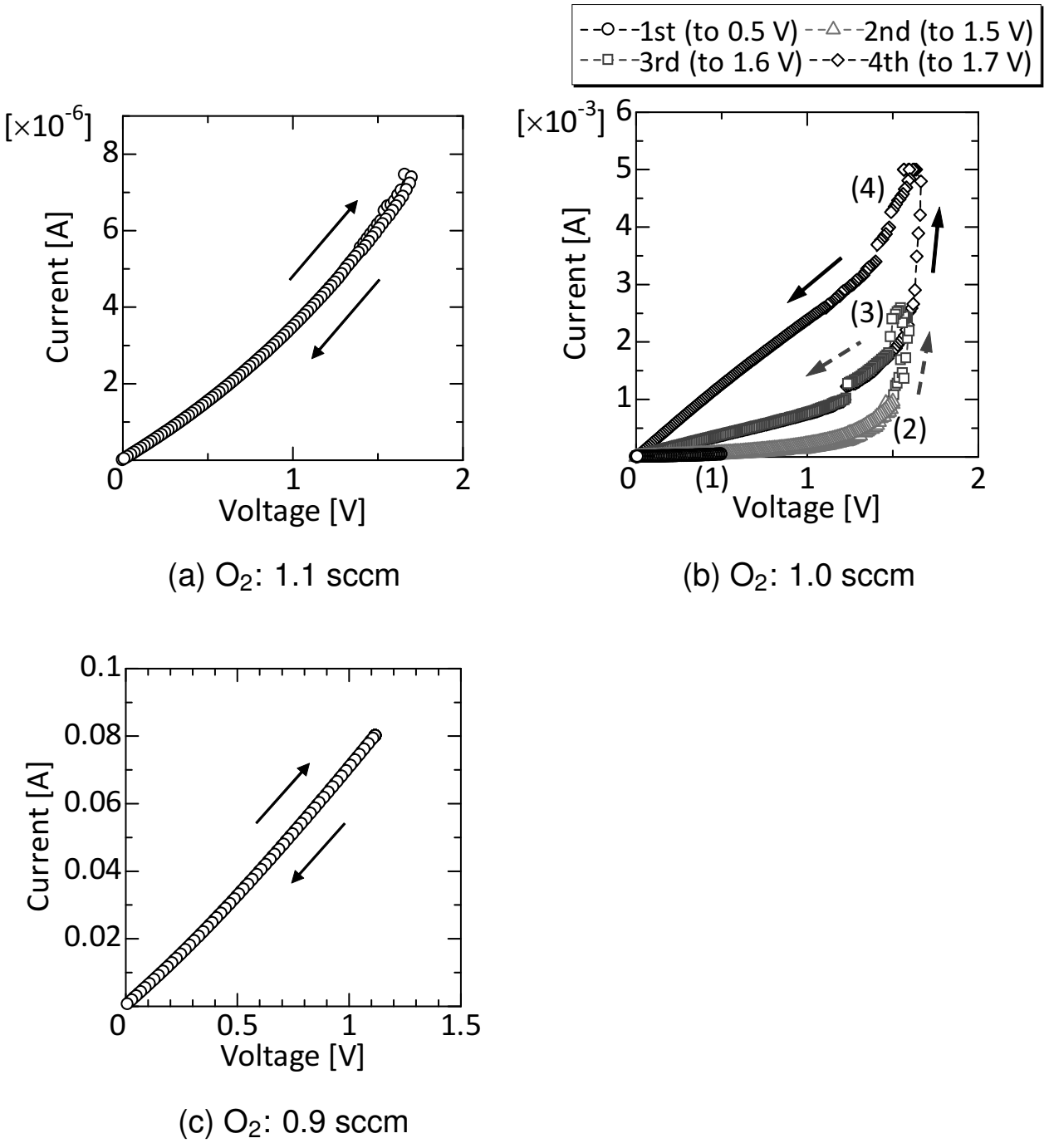

Figure 5.15: *I–V* characteristics of RS cells in their initial state. The NiO films in the RS cells were deposited with O_2-flow rates of (a) 1.1 sccm, (b) 1.0 sccm, and (c) 0.9 sccm.

Temperature dependence of the resistance

The temperature dependence of the resistance in the initial state was measured in NiO(0.9–1.1) films. Figure 5.16 shows (a) an Arrhenius plot of the resistance for NiO(1.1), and the resistance for (b) NiO(1.0) and (c) NiO(0.9), plotted against temperature, where the resistance was determined at a voltage bias of 0.1 V. In Fig. 5.16 (b), NiO(1.0)-1 and NiO(1.0)-2 denote the RS cells before and after the irreversible resistance decrease, respectively. The maximum voltages applied to the RS cells were 0.5 V for NiO(1.0)-1 and 1.7 V for NiO(1.0)-2.

The resistance of NiO(1.1) decreased as the temperature increased. Near room temperature, the temperature dependence of the resistance could be well fitted with an Arrhenius-type-resistance of the form, $R \sim \exp(E_{\mathrm{a}}/k_{\mathrm{B}}T)$. The dependence was similar to that in Chapter 3. The slope of the Arrhenius plot changed near 170 K. The temperature dependence for NiO(1.1) was characteristic of NiO, which is discussed in Chapter 6.

The resistances for NiO(1.0)-1 and NiO(0.9) are shown in Fig. 5.16 (b) and (c), respectively. The resistances in both samples decreased linearly with an increasing temperature, exhibiting a negative temperature coefficient of resistance (TCR). Since the temperature dependences for the resistance of NiO(1.0)-1 and NiO(0.9) were different from that of NiO(1.1), their temperature dependences originated from the resistance of the Ni segregation. The TCR was determined to be -2.1×10^{-3} K^{-1} for NiO(1.0)-1 and -2.4×10^{-3} K^{-1} for NiO(0.9) from the slope of the $R-T$ plot. The TCR value for each NiO film is tabulated in Table 5.4, where the resistivity measured at 300 K is also described. The TCR was comparable between NiO(1.0)-1 and NiO(0.9), indicating that the conduction properties for the Ni segregation were similar between NiO(0.9) and NiO(1.0)-1. Therefore, the difference in the resistivity between NiO(1.0)-1 and NiO(0.9) originated from the volume of the Ni segregation, not the change in the conduction properties for the Ni segregation. If the Ni segregations were composed for pure Ni, the TCR should become positive [20], which is opposite to the results in this thesis, indicating that the Ni segregation in both NiO(1.0)-1 and NiO(0.9) did not only consist of pure metallic components. The reason why these NiO films exhibited negative TCRs will be discussed later.

A clear difference in the temperature dependence of the resistance was observed between NiO(1.0)-1 and NiO(1.0)-2. As described above, the resistance in NiO(1.0)-1, which occurred before the irreversible resistance decrease, exhibited a negative TCR. NiO(1.0)-2 exhibited a positive TCR after the irreversible resistance decrease, indicating that the conduction properties of the Ni segregation in NiO(1.0)-2 were closer to a pure metal than that in NiO(1.0)-1. The TCR was calculated to be about 9.3×10^{-4} K^{-1}, which was much lower than that of pure Ni (5.3×10^{-2} K^{-1} [20]). Therefore, the Ni segregation in NiO(1.0)-2 may contain components other than the pure metallic components.

Discussion

It has been reported that the TCR of metal films decreased, even becoming negative, with an increase in the amount of oxygen in the atmosphere during deposition [24]. Gerstenberg and Cal-

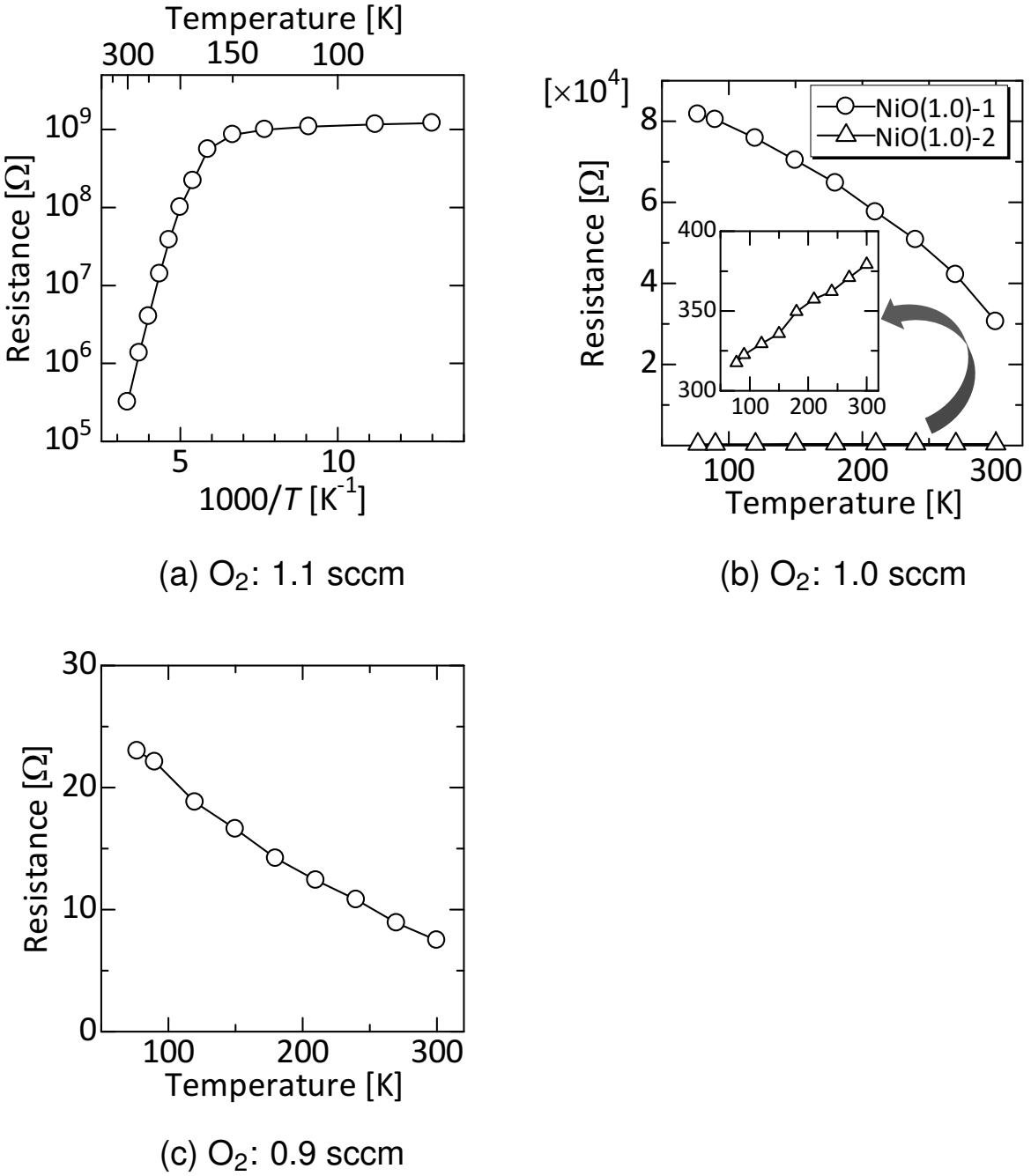

Figure 5.16: Temperature dependence of the resistance in the initial state of the RS cells. The NiO films for RS cells were deposited with O_2-flow rates of (a) 1.1 sccm, (b) 1.0 sccm, and (c) 0.9 sccm.

Table 5.4: Resistivity at 300 K and the temperature coefficient of resistance α in each NiO film.

	Ni [20]	NiO(0.9)	NiO(1.0)-1	NiO(1.0)-2	NiO(1.1)
ρ(300 K) Ωcm]	7.2×10^{-6}	16	6.7×10^{4}	830	7.0×10^{5}
α [$\times 10^{-3}$ K^{-1}]	52	−2.5	−2.1	0.93	–

bick attributed the negative TCR in tantalum films, in which an oxide phase was not recognized, to oxygen interstitials [24]. Tunneling conduction between metal islands separated by an insulating medium (an oxide in this study) was proposed as another mechanism, giving rise to the negative TCR [25]. The resistance in both NiO(1.0)-1 and NiO(0.9) decreased linearly with an increasing temperature. In addition, the resistance of NiO(1.0) decreased continuously when a voltage bias larger than 1.5 V was applied (Fig. 5.15 (b)). According to Ref. 24, when a metallic and an oxide phase coexisted, the TCR changed with temperature. Hence, the $R - T$ plot exhibited nonlinear characteristics, which does not agree with the linear temperature dependence for NiO(0.9) and Ni(1.0)-1. In addition, if the latter model is valid; that is, the Ni segregation at GBs are separated by oxides along the direction of the thickness, the resistance decrease observed in NiO(1.0) can be attributed to the breakdown of oxides at the GBs. However, the breakdown of oxides may cause the resistance to decrease abruptly, in a similar manner to the forming. Therefore, the negative TCR may have originated from the oxygen in the Ni segregation either as interstitials or as a solid solution, possibly in the form of ions. By applying an electrical field, oxygen ions migrated from the inside of the Ni segregation to the interface at the platinum electrode in a similar manner to the proposed RS mechanism [26]. Note that the sign of the TCR changed after the resistance decreased, which indicated that the conduction properties became closer to a pure metal. Therefore, the decrease in the resistance in NiO(1.0) may have resulted from the decrease in the oxygen concentration in the Ni segregation at the GBs by field-induced migration. The resultant resistance in NiO(1.0) was determined from the concentration of oxygen in the Ni segregation. NiO(1.0) exhibited a much lower TCR than that of pure Ni, even after the resistance decreased, indicating that the substantial oxygen interstitials remained in the Ni segregation after the application of a voltage. Although the conduction properties of the Ni segregation were likely to be explained by the Ni-O solid solution, further investigations on the conduction properties of the Ni segregation at the GBs, as well as its detailed structure is necessary.

5.4 Influences of NiO-Film Properties on Forming Voltage

5.4.1 Experimental procedure

NiO thin films were deposited on Pt (100 nm)/Ti (5 nm)/SiO_2/Si substrates. The conditions for the deposition were the same as described in Section 5.3.1. The NiO films deposited with an O_2-flow rate of X sccm are denoted as NiO(X) in a similar manner to Section 5.3.

The NiO(1.0) and NiO(1.1) films were annealed after deposition for 5 min at 450°C in an Ar atmosphere. For the I–V measurements, Pt/NiO/Pt RS cells with a diameter of 50 μm were used. The oxygen composition and crystalline properties of NiO films were characterized by RBS and XRD, respectively. For the NiO(1.0) and NiO(1.1) films, the microstructural changes in the NiO films that were annealed were analyzed by TEM and EDX. The NiO thickness was about 90 nm for the I–V measurements RBS, and TEM, and 640 nm for XRD.

5.4.2 Relationship between forming voltage and NiO-film properties

Comparison between the forming voltage and the NiO-film properties

Figure 5.17 shows the R_{Ini} and V_{Form} of the RS cells plotted against the O_2-flow rate during NiO deposition. Note that forming did not occur in the RS cells with NiO(0.9) before the current limit was reached because of their low R_{Ini}. Thus, V_{Form} was not plotted in the figure. Now we will discuss NiO(1.0–1.3). V_{Form} varied from 2.2 to 16.4 V, the minimum value of which was obtained in RS cells with NiO(1.1). On the whole, V_{Form} tended to increase with the O_2-flow rate during the NiO deposition, although V_{Form} was the smallest in RS cells with NiO(1.1). As depicted in Fig. 5.9, all of the NiO films in this study were preferentially $\langle 111 \rangle$-oriented. It was revealed that the peak position for the NiO$\{111\}$ planes shifted toward a lower angle with an increasing O_2-flow rate during deposition, as shown in Fig. 5.18. The lattice spacing of the NiO $\{111\}$ planes (d_{111}) was obtained from the peak position in the XRD $2\theta/\omega$-scans. The V_{Form}, oxygen composition of the NiO films and d_{111} are compared in Fig. 5.19, where they are plotted against the O_2-flow rate during the NiO deposition. As described in Section 5.3, the differences in the oxygen composition in the range of O_2-flow from 1.0 to 1.3 sccm were below the precision of quantification. Therefore, it was difficult to determine the dominating factor for V_{Form} from the results of RBS. d_{111} monotonically increased with the O_2-flow rate and showed no saturation trend. In addition, the d_{111} for all the prepared samples were larger than that of the bulk. Comparing the V_{Form}, there was a relationship between the V_{Form} and the d_{111}. In the later sections, the factors that determined the V_{Form} are investigated.

To determine cause of the change in the d_{111}, lattice strain caused by residual stress in the NiO films was considered. In general, thin films involved residual stress, which caused lattice strain. In the next section, the residual stress in the NiO films and its relationship with V_{Form} are investigated in detail.

5.4.3 Analyses of residual stress in NiO films by X-ray diffraction

To estimate the residual stress, strains of the lattice planes with various ψ (ε_ψ) were determined from the XRD measurements, where ψ is the angle between the lattice plane normal and the sample surface normal, as schematically shown in Fig. 5.20. In the cubic system, assuming equi-biaxial stress σ, ε_ψ is expressed as: [27, 28]:

$$\varepsilon_\psi = \frac{d - d_0}{d_0} = \frac{s_{44}}{2}\sigma \sin^2\psi + \frac{2s_{11} + 4s_{12} - s_{44}}{3}\sigma, \tag{5.2}$$

where d_0 is the lattice constant without strain and s_{ij} is the elastic compliance constant of a single crystal. The details of the derivation of equation (5.2) are described in Appendix A. According to equation (5.2), the stress was obtained from the slope of the $\varepsilon_\psi - \sin^2\psi$ plot. Here, d_0 was assumed to be equal to that of the bulk (d_{bulk}). The values of the d_{bulk} for the $\{100\}$ planes [29] and s_{ij} [30] employed in this study are shown in Table 5.5. Note that d_0 was generally not equal to d_{bulk}. Nevertheless, the difference caused a small error in obtaining the residual stress, providing

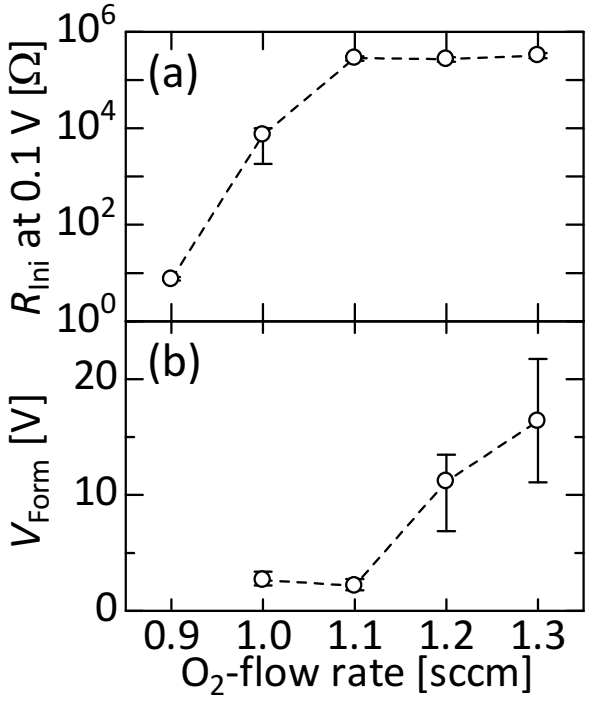

Figure 5.17: Dependence of (a) the initial resistance and (b)the forming voltage on the O_2-flow rate during NiO deposition.

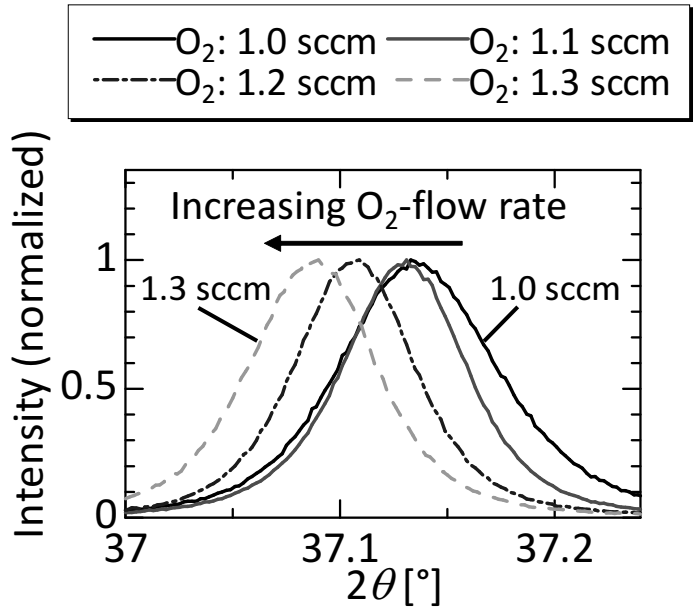

Figure 5.18: XRD $2\theta/\omega$-scans near the NiO{111} peak for NiO films deposited with different O_2-flow rates.

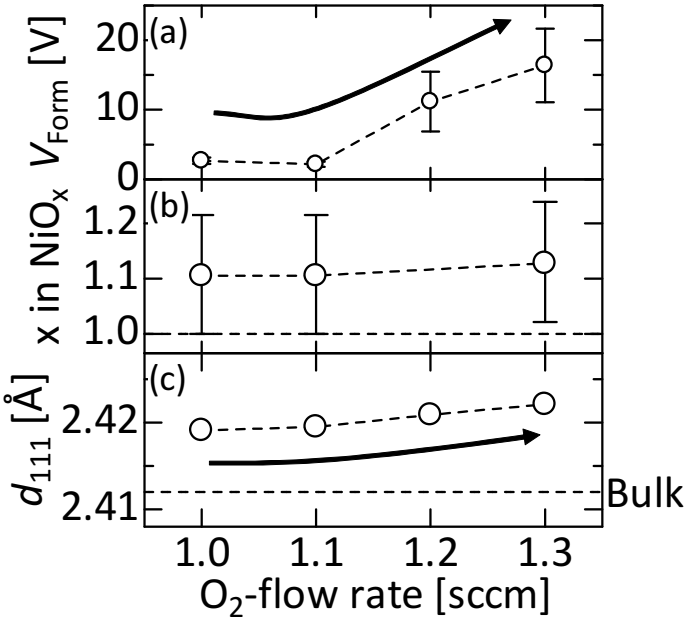

Figure 5.19: Comparison of (a) the forming voltage, (b) the oxygen composition of NiO, and (c) the lattice spacing in the NiO {111} plane. The horizontal axis indicates the O_2-flow rate during NiO deposition.

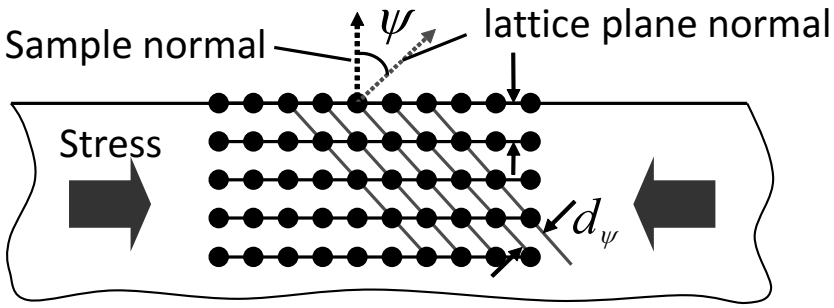

Figure 5.20: A schematic illustration of the strain measurements on the lattice planes, corresponding to various angles ψ.

Table 5.5: Lattice constant and elastic compliance of single crystalline NiO.

Lattice spacing [Å][a]	d_{bulk}	4.177
Elastic compliance[b]	s_{11}	5.2
[$\times 10^{-12}$ Pa]	s_{12}	-1.7
	s_{44}	9.5

a: ref. [29], b: ref. [30]

that the slope of the $\varepsilon_\psi - \sin^2\psi$ plot was used. Figure 5.21 shows the strains determined from the XRD measurements, plotted against $\sin^2\psi$. The relationship was almost linear for all of the NiO films, indicating that the equi-biaxial stress assumption was valid. Furthermore, the slopes changed depending on the sample, which indicated that the residual stress changed depending on the deposition conditions of the NiO films. As a consequence, the expansion of d_{111} was caused by the residual stress in the NiO films.

The residual stress σ was obtained from the slope of the $\varepsilon_\psi - \sin^2\psi$ plot using (5.2). Figure 5.22 shows the residual stress plotted against the O_2-flow rate during the NiO deposition. Negative values were obtained in all of the NiO films. The negative values indicated that there was a compressive stress and their absolute values represented their magnitudes. The residual stress was a minimum in the NiO(1.1) films. V_{Form} was plotted against the residual stress in Fig. 5.23. V_{Form} monotonically increased with the magnitude of the residual stress, showing the correlation between V_{Form} and the magnitude of the residual stress in the NiO films.

5.4.4 Effects of post-deposition annealing

RS characteristics

The NiO(1.0) and NiO(1.1) films were also annealed in Ar at 450°C for 5 min after deposition. The *I–V* characteristics and XRD patterns were measured for the RS cells with annealed NiO films. Figure 5.24 shows the R_{Ini} and V_{Form} before and after the films were annealed. All of the RS cells with annealed NiO(1.0) exhibited a reset transition by applying voltages in the initial state, that is, forming-free behavior, indicating that filaments were generated by annealing. Both the R_{Ini} and V_{Form} significantly increased in the RS cells with NiO(1.1). Several RS cells exhibited forming-free behavior or a low V_{Form} (this is why the V_{Form} distribution in the annealed NiO(1.1) had a large variation). The increase in R_{Ini} may be caused by the increase in the activation energy for conduction, as discussed in Chapter 3.

X-ray diffraction

Figure 5.25 shows the changes in the XRD $2\theta/\omega$-scans near the NiO {111} plane for (a) NiO(1.0) and (b) NiO(1.1) before and after annealing. The peak positions shifted toward a higher angle after both the NiO(1.0) and NiO(1.1) were annealed. Furthermore, an additional peak was observed at the right shoulder of the main peak for the NiO(1.0) after it was annealed. Fig. 5.26 shows the lattice spacing of the NiO {111} plane before and after annealing. The lattice spacing in both samples decreased after the samples were annealed, owing to the partial relaxation of the residual stress (data not shown). Furthermore, the lattice spacing corresponding to the additional peak in the annealed NiO(1.0) was smaller than that of bulk NiO. The existence of a smaller lattice spacing than that of bulk NiO may have been caused by the appearance of regions that had a tensile stress, which was suggested by the change in the stress in the NiO(0.9) films after post-deposition annealing. Figure 5.27 shows the $\varepsilon_\psi - \sin^2\psi$ plot for a NiO(0.9) before and after

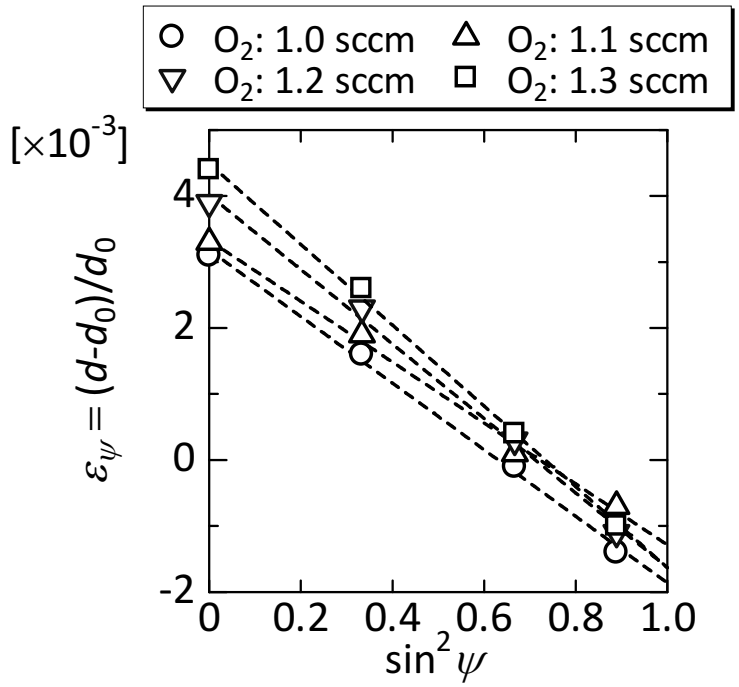

Figure 5.21: Strain of the NiO films measured by XRD plotted against $\sin^2\psi$.

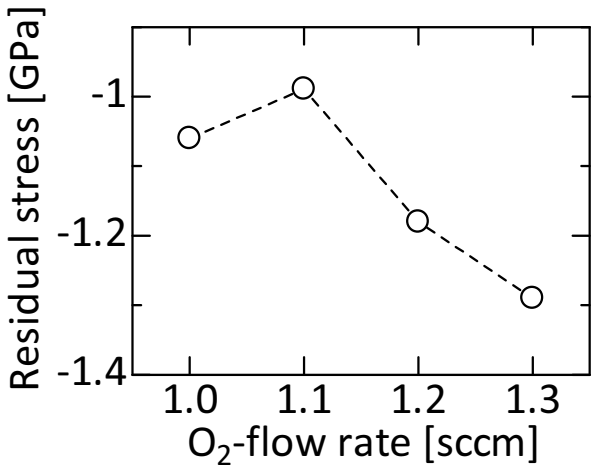

Figure 5.22: Residual stress in the NiO films, plotted against the O_2-flow rate during deposition. The negative signs represent compressive stress.

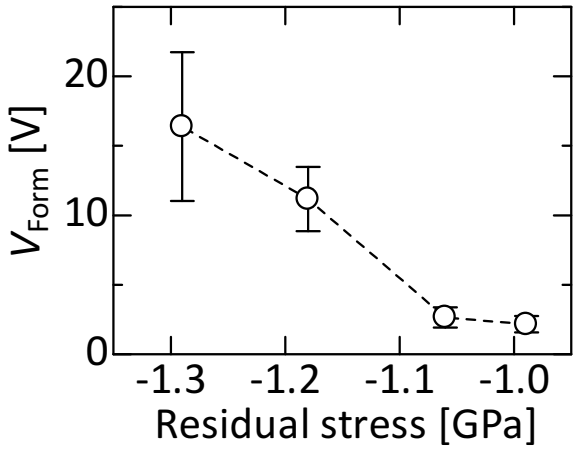

Figure 5.23: The frming voltage plotted against the residual stress in NiO films.

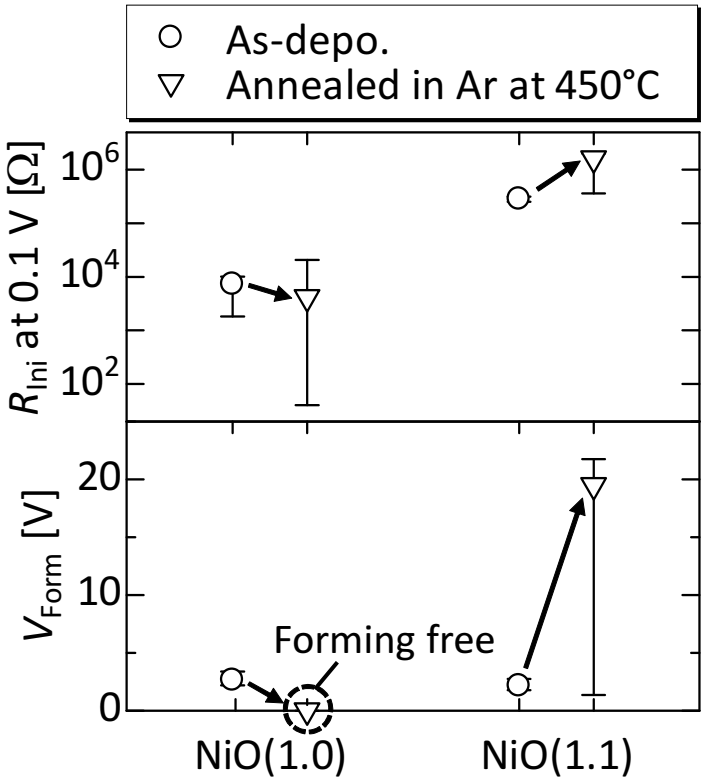

Figure 5.24: Changes in the initial resistance and forming voltage of RS cells by post-deposition annealing.

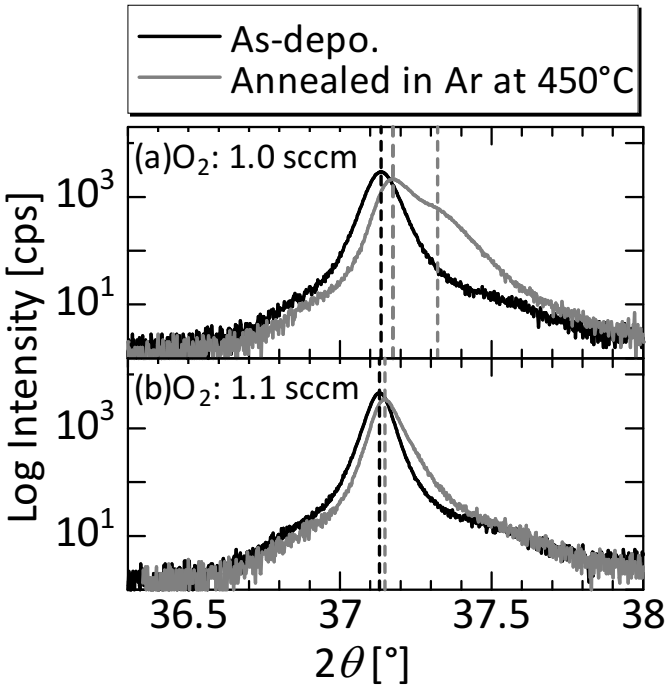

Figure 5.25: XRD $2\theta/\omega$-scans near the NiO{111} peak before and after annealing. Deposited with (a) O_2 = 1.0 sccm, and (b) O_2 = 1.1 sccm.

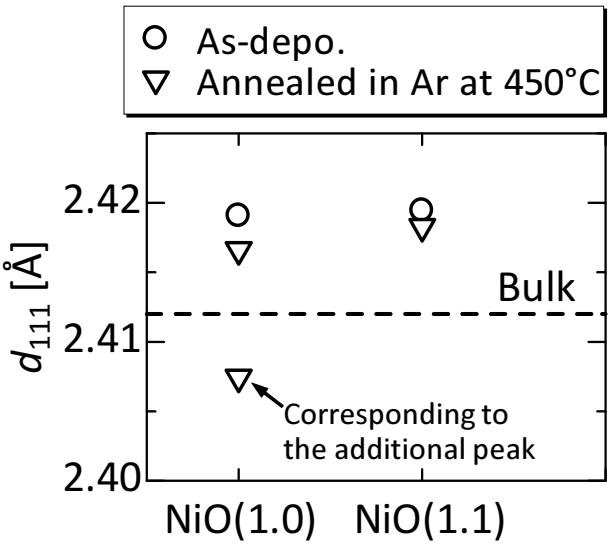

Figure 5.26: Lattice spacing of the NiO{111} plane before and after annealing. In NiO(1.0), after annealing, the lattice spacing corresponded to both the main and an additional peak in the XRD patterns, which are plotted in Fig. 5.25 (a).

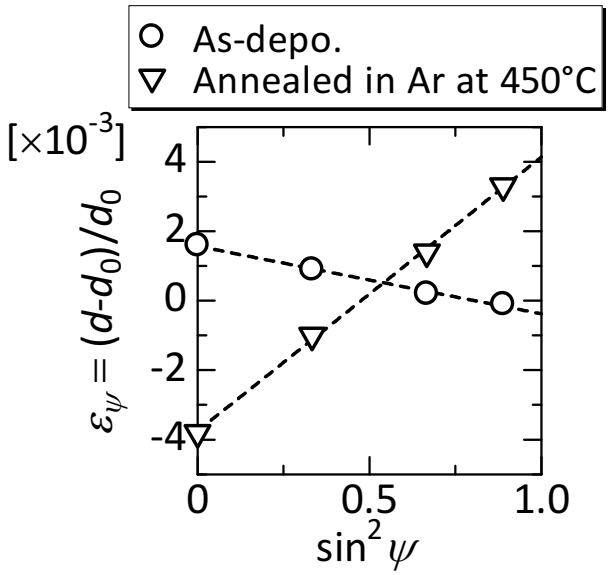

Figure 5.27: $\varepsilon_\psi - \sin^2\psi$ plot of a NiO film at O_2 = 0.9 sccm before and after annealing.

annealing. The slope of the plot became positive after annealing, indicating that the residual stress changed from compressive to tensile.

TEM observations

Figure 5.28 shows the plan-view TEM images of (a), (b) as-deposited and (c), (d) annealed NiO(1.0) films. (a), (c) and (b), (d) are the BF and HAADF images, respectively. In the HAADF images, the GBs in annealed NiO(1.0) films became vague after they were annealed (d), compared with the as-deposited NiO(1.0) films (b). In particular, most of the bright regions at the GBs, which were observed in the as-deposited NiO(1.0) films, disappeared after annealing. EDX point analysis was conducted on annealed NiO(1.0) films near the points indicated in Fig. 5.28 (d) (P1-P6). The chemical compositions are tabulated in Table 5.6. In contrast to the as-deposited NiO(1.0) films, most of the GBs exhibited an O-rich composition. Although Ni-rich regions such as P1 were observed, their areas were small compared with those in the as-deposited NiO(1.0) films. Taking into account that the macroscopic chemical composition of the as-deposited NiO films measured by RBS was O-rich, the Ni segregation formed at the GBs was oxidized during annealing, by the excess oxygen in the grains. There were no significant changes observed in the annealed NiO(1.1) films and Ni segregation did not exist at the GBs (data not shown).

5.4.5 Discussion

The origin of the residual stress and its relationship with V_{Form} for the as-deposited RS cells

The residual stress in thin films was generally caused by (1) thermal stress σ_{th} [28], (2) lattice defects, such as interstitial defects [31], and (3) a decrease in volume by atomic rearrangement during deposition [32]. Among these, (3) generally caused tensile stress. Therefore, the origin of the stress will be discussed by considering (1) and (2). Note that a lattice mismatch was unlikely to be the cause of the residual stress, since the lattice constant along the lateral direction was completely different for the NiO film and the Pt BE. Thermal stress was caused by the difference in the CTE between the films and the substrate, and is expressed as: [28, 33]:

$$\sigma_{th} = \frac{E_f}{1 - \nu_f} \left(\alpha_f - \alpha_s \right) \Delta T, \tag{5.3}$$

where E_f and ν_f are Young's modulus and the Poisson ratio of the film, respectively. α is the CTE of f: for the film and s: for the substrate. ΔT (> 0) is the difference between the deposition temperature and RT. In this study, the substrates for the NiO deposition consisted of a Pt/Ti/SiO_2/Si multilayer. Thus, it was difficult to accurately estimate the CTE of the substrates. The CTE for NiO was the largest of the materials studied, as shown in Table 5.7. Therefore, the effective CTE of the substrates could be smaller than that of NiO films, which caused thermal stress with tension in the NiO films. In addition, the thermal stress could not explain the differences in the stresses in the NiO films deposited at the same temperature. Thermal stress, therefore, was not the origin of the compressive stress. As a consequence, the compressive stress was attributed to the lattice defects in the NiO films.

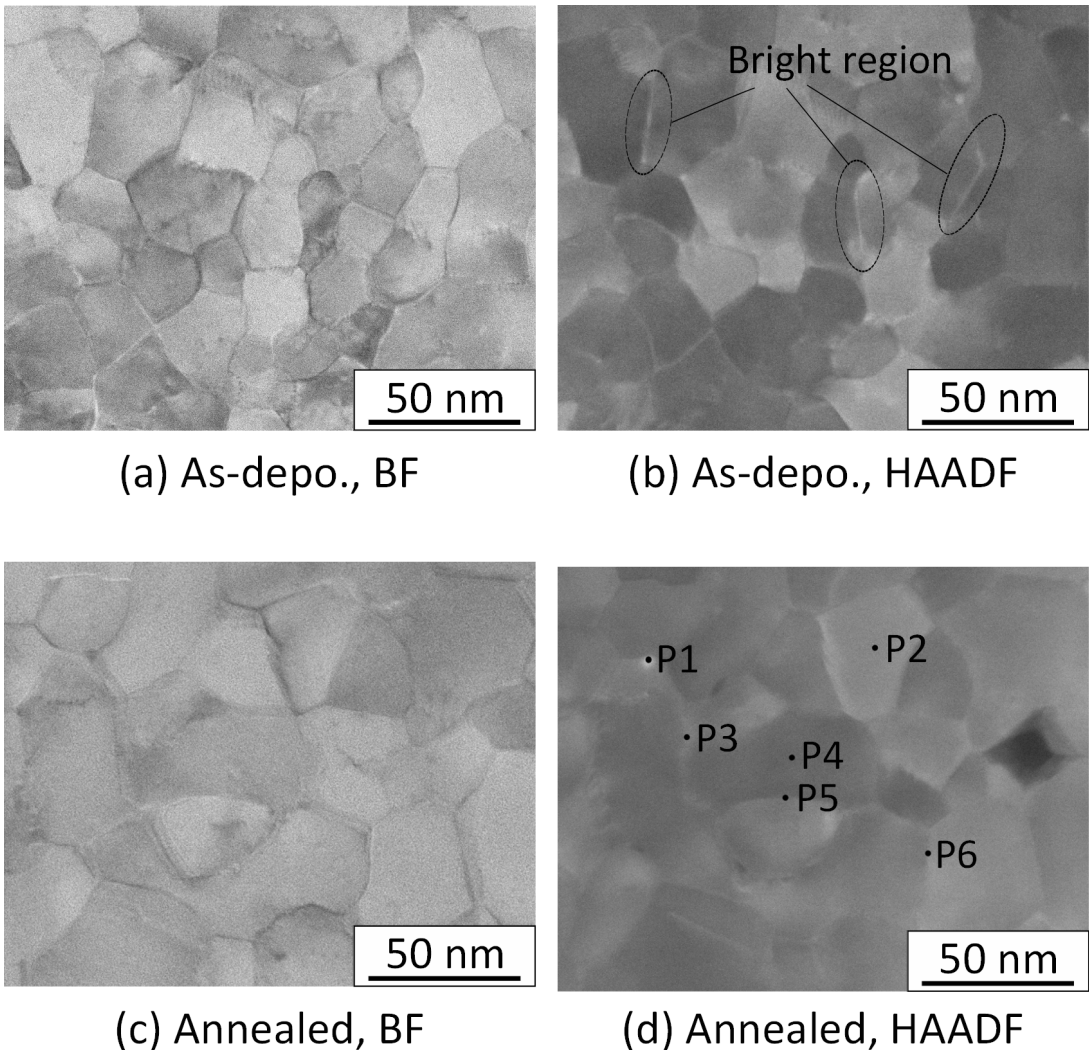

Figure 5.28: Plan-view TEM image of (a) and (b) as-deposited NiO films deposited with O_2 = 1.0 sccm, and (c) and (d) the same films after annealing. (a) and (c) are bright-field and (b) and (d) are high-angle-annular-dark-field images. The points where the chemical composition was analyzed are depicted in (d).

Table 5.6: Chemical composition of an annealed NiO(1.0), near the points indicated in Fig. 5.28 (d), analyzed by EDX.

NiO(1.0): annealed	P1	P2	P3	P4	P5	P6
Ni [at. %]	65.0	47.5	44.4	47.0	46.1	46.0
O [at. %]	35.0	52.5	55.6	53.0	53.9	54.0

Table 5.7: Coefficient of thermal expansion of the materials used in this study.

Material	α [$\times 10^{-6}$ K^{-1}]
NiO[a]	13.9
Pt[b]	9.6
Ti[b]	9.9
Si[b]	3.5
SiO_2[b]	0.55

a: ref. [37], b: ref. [20]

Various defects including, nickel vacancies (V_{Ni}), oxygen vacancies (V_O), nickel interstitials (Ni_i), and oxygen interstitials (O_i) may coexist in the NiO films, because the NiO films were deposited under non-equilibrium conditions. Among these defects, incorporation of a large amount of interstitials can give rise to compressive stress [31]. Taking into account that the NiO films had an O-rich composition, and that the compressive stress increased with an increasing O_2-flow rate during NiO deposition, the origin of the residual compressive stress may be O_i. The incorporation of O atoms as interstitials is speculated to be caused by the exchange of the momentum of the O atoms on the substrate with an energetic species such as sputtered-Ni atoms and recoiled neutral Ar atoms. This effect is known as "atomic peening" [34]. O atoms have a lower atomic mass compared with Ni and Ar atoms. Thus, they may be easier to embed as interstitials during deposition. Part of the incorporated O_i could be annihilate with V_O, as suggested by Ref. 35. Therefore, the increase in the O_i also caused the decrease in the V_O. It was shown with an *ab initio* calculation that a single V_O caused lattice relaxation in such a way that the surrounding atoms were attracted toward the vacancy site [36]. Therefore, the decrease in V_O was not likely to relax the compressive stress. From the above discussion, the increase in the residual compressive stress was attributed to the increase in the amount of O_i, accompanied by the decrease in V_O.

The V_O acted as seeds for the filaments [38]. In addition, considering that the forming process can be described by a percolation model [7, 8], the reduction in the V_O may cause the increase in the V_{Form}. Therefore, the residual stress and V_{Form} are correlated to each other via the density of oxygen vacancies in the NiO films. Further investigations on the lattice defects in the NiO films as well as their effects on the V_{Form} and the residual stress are necessary.

Effects on the forming voltage by post-deposition annealing

It has been revealed that the Ni segregation disappeared by post-deposition annealing the NiO(1.0) films. This is likely caused by oxidation during annealing, as described in Section 5.4.4. An additional peak associated with tensile stress was observed in the XRD pattern for the annealed NiO(1.0). The RS cells with annealed NiO(1.0) exhibited forming-free behavior, indicating that filaments were formed during annealing. Therefore, the formation of the filaments may result from the oxidation of the Ni segregation. Oxidation of the Ni segregation could also cause changes in the volume of NiO. As a result, tensile stress in the annealed NiO(1.0) arose, which caused the non-uniformity in the spatial distribution of the residual stress. This may be the reason why an additional peak appeared after the NiO(1.0) were annealed.

Ni segregation was rarely observed in the as-deposited NiO(1.1), and the changes in the chemical composition after annealing were not detected, even at the GBs. The residual stress was partially relaxed by annealing, indicating that the reduction in the O_i likely caused by annihilation of the O_i and V_O. Therefore, as a result of the reduction in the V_O, V_{Form} increased after the NiO(1.1) were annealed.

5.5 Improvement of RS Characteristics by Reduction of Forming Voltage

It has been pointed out that R_{Ini} and V_{Form} significantly changed with the O_2-flow rate during NiO deposition. As a consequence, a low V_{Form} and a large R_{Ini} were simultaneously obtained in RS cells with NiO deposited with an O_2-flow rate of 1.1 sccm, as shown in Fig. 5.17. Figure 5.29 shows the I–V characteristics of a (a) former (in Chapter 4) and (b) a V_{Form}-reduced RS cell. By reducing V_{Form}, R_{LRS} increased to about 40 kΩ, which is about three orders of magnitude larger than that of the former RS cell ($R_{\mathrm{LRS}} \approx 30$ Ω). The reset current was also reduced to tens of μA, which is comparable to the value of state-of-the-art RS cells [38].

Figure 5.30 shows a Nomarski microscope images of an RS cell. The I–V characteristics are represented in Fig. 5.29 (b). In each figure, the circular region at the center was a TE, which was a part of the RS cell. No deformation was observed, even after the forming and resistive switching (b). As a result, deformation accompanying forming could be suppressed by reducing V_{Form}.

5.6 Summary

The influences of the microstructure and crystalline properties on the R_{Ini} and V_{Form} have been investigated to reduce the V_{Form} while keeping R_{Ini} sufficiently large. After the T_{sub} and bottom electrode for NiO sputtering were optimized, various NiO films were deposited by varying the O_2-flow rate during sputtering. The influences of the microstructure of the NiO films on the R_{Ini} of the RS cells were investigated. A NiO film was composed of a number of grains with diameters of tens of nm. TEM observations revealed that Ni-segregation appeared at the GBs when the NiO films were sputtered under a low-O_2-flow rate, while the NiO grains had an O-rich composition. Furthermore, C-AFM measurements revealed that the segregated Ni at the GBs acted as electrical leakage paths in the initial state, giving rise to the decrease in the R_{Ini}. The NiO films had a residual compressive stress. The relationship between the residual compressive stress and the V_{Form} was determined. The reason why they are linked was discussed based on lattice defects. V_{Form} became smaller in the NiO films that contained a large number of oxygen vacancies. Furthermore, the Ni segregation observed in the NiO films disappeared after post-deposition annealing. The RS cells containing NiO films exhibited forming-free behavior. Forming-free behavior may have occurred because of the generation of filaments by incomplete oxidation of the Ni segregation, formed at the GBs. In the NiO films without Ni segregation, post-deposition annealing caused an increase in the V_{Form}, which may have originated from annihilation of V_{O} and O_{i}. As a consequence of this investigation, RS cells exhibiting a low V_{Form} and a sufficiently large R_{Ini} were obtained. The RS cells exhibited a R_{LRS} of more than 10 kΩ and a low I_{Reset} of about tens of μA. Compared with the RS cells in Chapter 5, the R_{LRS} was increased by more than two orders of magnitude, and I_{Reset} was lowered by more than two orders of magnitude. Furthermore, no deformation accompanied the forming, and resistive switching was not observed in the low-V_{Form}

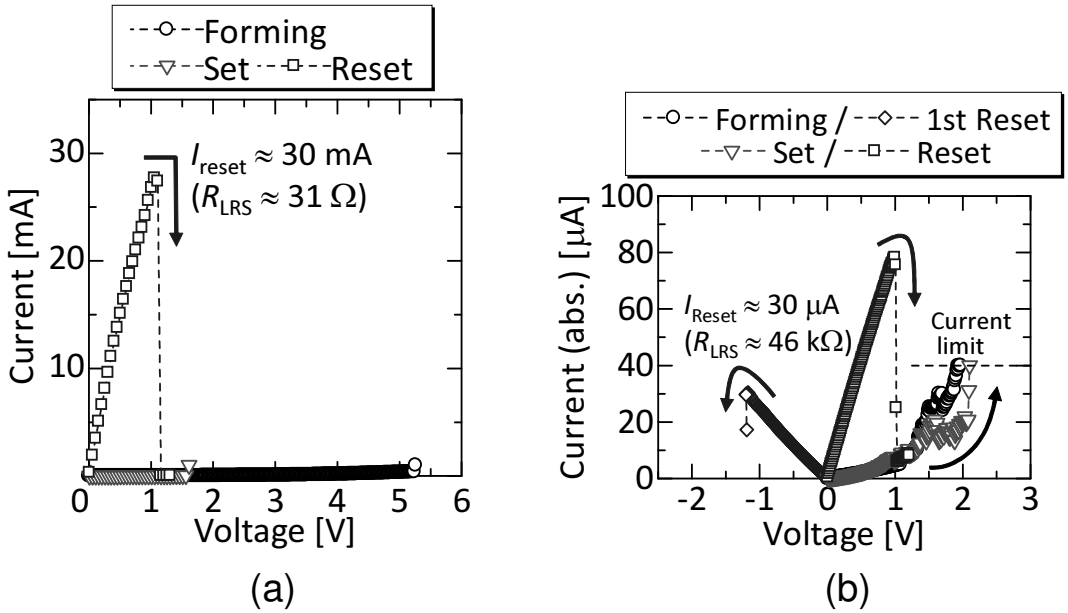

Figure 5.29: *I–V* characteristics of (a) an RS cell fabricated under the same conditions as in Chapter 4 (high-forming voltage) and (b) an RS cell exhibiting a low-forming voltage [NiO(1.1)].

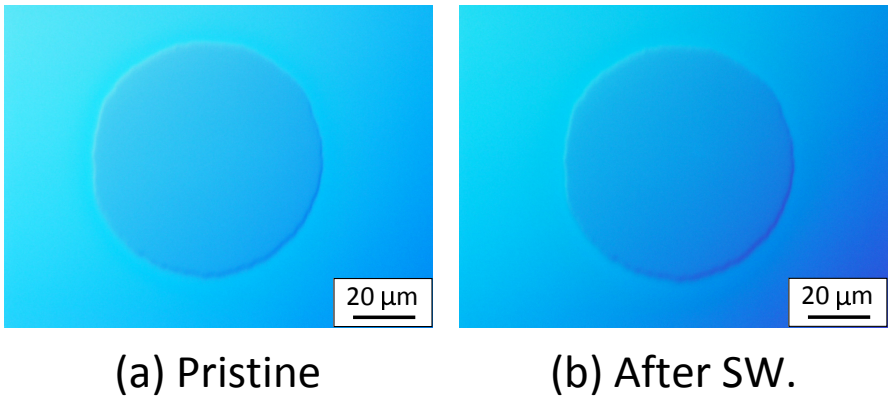

Figure 5.30: (a) A Nomarski microscopy image of a pristine RS cell that exhibited a low-forming voltage. (b) A Nomarski microscopy image of the same RS cell in (a) after switching. No deformation was observed after switching.

RS cells, which allowed the properties of the filaments to be investigated detail.

References

[1] H. Shima, F. Takano, H. Muramatsu, H. Akinaga, Y. Tamai, I. H. Inque, and H. Takagi, Appl. Phys. Lett. **93**, 113504 (2008).

[2] C.-Y. Liu, J.-Y. Ho, J.-J. Huang, and H.-Y. Wang, Jpn. J. Appl. Phys. **51**, 041101 (2012).

[3] A. Kalantarian, G. Bersuker, D. C. Gilmer, D. Veksler, B. Butcher, A. Padovani, O. Pirrotta, L. Larcher, R. Geer, Y. Nishi, and P. Kirsch, *2012 IEEE Int. Reliab. Phys. Symp.* (2012) p. 6C.4.1.

[4] H. Schroeder, R. Pandian, and J. Miao, Phys. Status Solidi (a) **208**, 300 (2011).

[5] D. Ielmini, F. Nardi, and C. Cagli, IEEE Trans. Electron Devices **58**, 3246 (2011).

[6] K. Kinoshita, K. Tsunoda, Y. Sato, H. Noshiro, S. Yagaki, M. Aoki, and Y. Sugiyama, Appl. Phys. Lett. **93**, 033506 (2008).

[7] G. Buh, I. Hwang, and B. H. Park, Appl. Phys. Lett. **95**, 142101 (2009).

[8] Y. Nishi, T. Iwata, D. Horie, and T. Kimoto, *Mater. Res. Soc. Symp. Proc.* **1430** (2012) DOI: 10.1557/opl.2012.1023.

[9] Y.-S. Chen, H.-Y. Lee, P.-S. Chen, T.-Y. Wu, C.-C. Wang, P.-J. Tzeng, F. Chen, M.-J. Tsai, and C. Lien, IEEE Electron Device Lett. **31**, 1473 (2010).

[10] S. Kim, D. Lee, J. Park, S. Jung, W. Lee, J. Shin, J. Woo, G. Choi, and H. Hwang, Nanotechnology **23**, 325702 (2012).

[11] S. Berg, J. Vac. Sci. Technol. A **5**, 202 (1987).

[12] S. Berg and T. Nyberg, Thin Solid Films **476**, 215 (2005).

[13] H.-L. Chen, Y.-M. Lu, J.-Y Wu, and W.-S. Hwang, Materials Transactions **46**, 2530 (2005).

[14] H.-L. Chen and Y.-S. Yang, Thin Solid Films **516**, 5590 (2008).

[15] J. A. Thornton, Annual Review of Materials Science **7**, 239 (1977).

[16] K. Sreenivas, I. Reaney, T. Maeder, N. Setter, C. Jagadish, and R. G. Elliman, J. Appl. Phys. **75**, 232 (1994).

[17] *Hakumaku Kogaku Handbook* edited by M. Mashita and M. Yoshida (Kodansha, Tokyo, 1998).

[18] P. De Wolf, T. Clarysse, W. Vandervorst, J. Snauwaert, and L. Hellemans, J. Vac. Sci. Technol. B **14**, 380 (1996).

[19] R. A. Oliver, Rep. Prog. Phys. **71**, 076501 (2008).

[20] *Rika nenpyo 1993 (Chronological Scientific Tables)* edited by National Astronomical Observatory (Maruzen, Tokyo, 1992).

[21] B. Cappella and G. Dietler, Surf. Sci. Rep. **34**, 1 (1999).

[22] J. Merker, D. Lupton, M. Tpfer, and H. Knake, Platinum Metals Review **45**, 74 (2001).

[23] R. Jung, M.-J. Lee, S. Seo, D. C. Kim, G.-S. Park, K. Kim, S. Ahn, Y. Park, I.-K. Yoo, J. Kim, and B. H. Park, Appl. Phys. Lett. **91**, 022112 (2007).

[24] D. Gerstenberg and C. J. Calbick, J. Appl. Phys. **35**, 402 (1964).

[25] C. A. Neugebauer and M. B. Webb, J. Appl. Phys. **33**, 74 (1962).

[26] H. Akinaga and H. Shima, Proc. IEEE **98**, 2237 (2010).

[27] K. Tanaka, Y. Akiniwa, T. Ito, and K. Inoue, JSME Int. J. Ser. A **42**, 224 (1999).

[28] K. Tanaka, K. Suzuki, and Y. Akiniwa, *Evaluation of Residual Stresses by X-Ray Diffraction —Fundamentals and Applications—* (Yokendo, Japan, 2006).

[29] I. Wakabayashi, H. Kobayashi, H. Nagasaki, and S. Minomura, J. Phys. Soc. Jpn. **25**, 227 (1968).

[30] N. Uchida and S. Saito, J. Acoust. Soc. Am. **51**, 1602 (1972).

[31] F. M. D'Heurle and J. M. E. Harper, Thin Solid Films **171**, 81 (1989).

[32] E. Klokholm and B. S. Berry, J. Electrochem. Soc. **115**, 823 (1968).

[33] *Thin Film Technology, 2nd ed.* edited by S. Yoshida and T. Kondo (Maruzen, Tokyo, 2001).

[34] F. M. D'Heurle, Metall. Trans. **1**, 725 (1970).

[35] K.-H. Müller, J. Appl. Phys. **62**, 1796 (1987).

[36] S. Park, H.-S. Ahn, C. Lee, H. Kim, H. Jin, H.-S. Lee, S. Seo, J. Yu, and S. Han, Phys. Rev. B **77**, 134103 (2008).

[37] E. Gillam and J. P. Holden, J Am Ceram Soc **46**, 601 (1963).

[38] H.-S. P. Wong, H.-Y. Lee, S. Yu, Y.-S. Chen, Y. Wu, P.-S. Chen, B. Lee, F. T. Chen, and M.-J. Tsai, Proc. IEEE **100**, 1951 (2012).

Chapter 6

Conduction Mechanism of Resistive Switching Cells

6.1 Introduction

For nonvolatile memory applications, it is essential to understand the electrical conduction mechanism in the resistance states, including the initial state, the high-resistance state (HRS) and the low-resistance state (LRS). To model the conduction in a resistive switching (RS) cell, a parallel-circuit model has been proposed [1]. In the model, the total resistance of a RS cell (R_{cell}) is expressed as the sum of the resistances of the filament and the remainder of the oxide region. For example, in a nickel oxide (NiO)-based RS cell, an equivalent circuit in the LRS is represented by a parallel connection between the filament resistance (R_{fil}) and the bulk of NiO (R_{bulk}), as shown in Fig. 6.1 (a). The HRS is considered to be a state in which the filament is partially ruptured [2, 3]. Therefore, an equivalent circuit of the filament is represented by a series connection of the resistance of the remaining filament (R'_{fil}) and the ruptured part of the filament (R_{rup}), as shown in Fig. 6.1 (b). If R_{bulk} was much larger than R_{fil} or $R'_{\mathrm{fil}} + R_{\mathrm{rup}}$, resistance was virtually the same as R_{fil} in the LRS and $R'_{\mathrm{fil}} + R_{\mathrm{rup}}$ in the HRS.

In the measurements using an RS cell with a large area, such as a ~ 10 μm diameter and/or at a high temperature, R_{bulk} was comparable to the resistance of the filament (R_{fil} or $R'_{\mathrm{fil}} + R_{\mathrm{rup}}$), and the actual conduction characteristics of the filament were blurred by the R_{bulk} [1]. Therefore, we need to be careful in determining whether R_{bulk} was sufficiently larger than the resistance of the filament in the analysis of the results on the conduction characteristics in the LRS and the HRS.

It has been reported that the conduction in the LRS is metallic [1, 4, 5]. However, the range of the resistance in the LRS (R_{LRS}) is limited to a maximum of several hundreds of ohms. Ielmini *et al.* reported that R_{LRS} had an Arrhenius-type temperature-dependence when R_{LRS} was larger than 1 kΩ [6]. In this report, the activation energy of R_{LRS} increased with an increase in R_{LRS}. However, the origin of the activation energy and the reason for its change has not been investigated in detail.

For the conduction mechanism in the HRS, Jung *et al.* reported metallic-like behavior [4] in

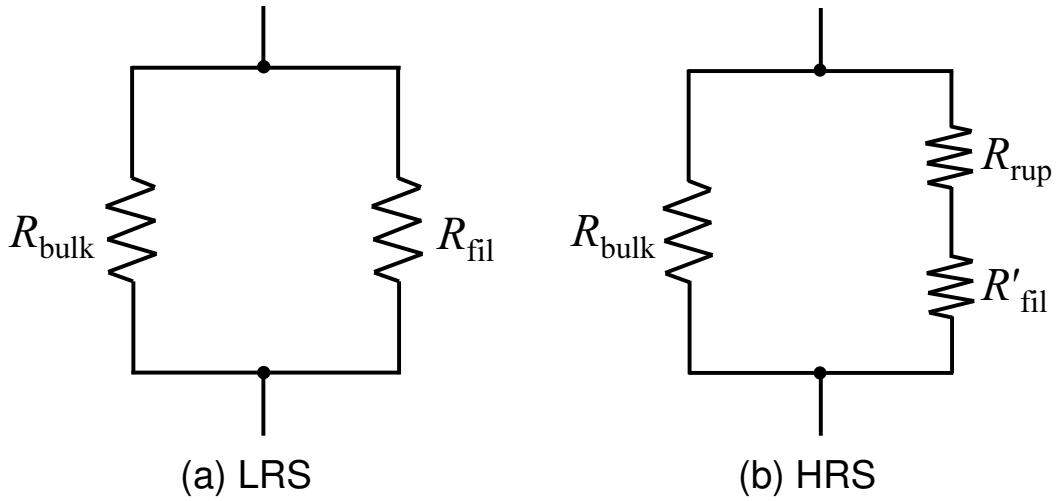

Figure 6.1: Equivalent circuit of an RS cell in (a) the LRS and (b) the HRS.

the early stage. Recently, the conduction mechanism in the HRS has been extensively studied in hafnium dioxide (HfO_2)-based RS cells [7, 8]. These studies claimed that conduction in the HRS was dominated by the resistance of the ruptured filament, where the dominant process for conduction was tunneling [9] or trap-assisted-tunneling [7], similar to that in the bulk [8]. At present, the conduction mechanism is not completely understood and further investigation is still necessary.

In this chapter, the temperature dependence of the DC and AC conduction characteristics of RS cells are analyzed in the temperature range of 77 – 370 K. The conduction mechanism for each resistance state was investigated by setting the RS cells to various resistance states, including the initial state. In particular, the improvement of the RS cell characteristics described in Chapter 5 enabled us to obtain an RS cell with a large R_{LRS} ranging from about 10 kΩ to 150 kΩ. The origin of the difference in the resistance states is also discussed from the point of view of the conduction mechanism.

6.2 Electrical Measurement Setup

A 100-nm-thick platinum (Pt) bottom electrode (BE) was sputtered on a SiO_2/Si substrate with a 5-nm-thick titanium (Ti) insertion layer. The NiO films were deposited at 350°C while the total pressure and a gas-flow rate were maintained at 0.6 Pa and 9 sccm, respectively. The flow rate for oxygen (O_2) during sputtering was either 1.1 or 1.2 sccm, where the NiO films deposited with the respective O_2-flow rate are denoted as NiO(1.1) and NiO(1.2). The thicknesses of NiO films were about 90 nm. To measure the RS cells in the initial state, both the NiO(1.1) and NiO(1.2) were used, while NiO(1.1) was used to measure the LRS and the HRS. The diameters of the RS cells were 50 μm. The detailed conditions for fabricating the RS cells were the same as those in Chapter 5. The RS cells with NiO(1.1) exhibited a low forming voltage (V_{Form}) of about 2 V, while those with NiO(1.2) exhibited a high V_{Form} of about 12 V. The initial resistances (R_{Ini}) of the RS cells were 270 kΩ for NiO(1.1) and 210 kΩ for NiO(1.2). For the measurements with the RS cells in the LRS and the HRS, several RS cells were switched to the LRS or HRS with different resistances to each other. RS cells in the LRS with resistances ranging from about 9 kΩ to 150 kΩ were prepared by controlling the current compliance during the set transition. A single RS cell in the HRS with a resistance of about 250 kΩ was prepared. These resistance values were measured at 300 K at a voltage bias of 0.1 V before the temperature dependence measurements.

The DC resistance and AC conductance were measured for the prepared RS cells. The AC conductance was measured in the frequency range from 40 to 40 MHz, where the oscillation amplitude and bias voltage were 50 mV and 0 V, respectively. Measurements were carried out under a vacuum ($< 1 \times 10^{-3}$ Pa) in the temperature range from 77 to 370 K. During the measurements, the temperature was increased from 77 to 370 K.

6.3 Conduction in the Initial State

6.3.1 Temperature dependence of the resistance

Figure 6.2 shows an Arrhenius plot of the DC resistance at 0.1 V. The data from RS cells with both NiO(1.1) and NiO(1.2) are also plotted. Near room temperature (RT), both the RS cells with NiO(1.1) and NiO(1.2) exhibited almost identical Arrhenius-type temperature dependences $R \sim \exp(E_a/k_B T)$ similar to Chapter 3. The activation energy (E_a) of the DC resistance near RT was about 330 meV. In contrast, below 170 K, a different temperature dependence was observed. The resistance of the RS cell with NiO(1.2) increased to the detection limit (D. L.) of the measuring instrument (1 pA), whereas the slope of the Arrhenius plot for the NiO(1.1) sample changed, exhibiting a low E_a of about 3.1 meV. As discussed in Section 5.4, a low V_{Form} may be associated with a high density of oxygen vacancies (V_O). Since the V_{Form} of the RS cells with NiO(1.1) and NiO(1.2) were about 2 V and 12 V, respectively, NiO(1.1) had a higher density of V_O compared with NiO(1.2). Therefore, conduction with a low E_a of 3.1 meV that was observed only in an RS cell with NiO(1.1) may be related to V_O. The results of the temperature dependence of the DC resistance indicated that different conduction processes dominated the DC conduction in the RS cells with NiO(1.1) depending on the temperature. Hereafter, the conduction characteristics of an RS cell with NiO(1.1) are investigated in detail.

6.3.2 AC conduction characteristics

Figure 6.3 shows the AC conductance of an RS cell with NiO(1.1) at different temperatures plotted against the angular frequency (ω). The AC conductance increased as the temperature increased, which agrees with the decrease in the DC resistance. In addition, the conductance increased with ω, particularly at temperatures below 170 K. The conductance became independent of the frequency in low-frequency range as the temperature approached RT. It has been pointed out that the total AC conductance (G_{tot}) can be separated into frequency-independent and frequency-dependent components, if they arise from different conduction processes [10], namely

$$G_{tot}(\omega) = G_0 + G(\omega), \tag{6.1}$$

where G_0 and $G(\omega)$ are the frequency-independent and frequency-dependent components, respectively. If the same conduction process is responsible for both components, the DC conductance (G_{DC}) is the $\omega \to 0$ limit of $G_{tot}(\omega)$. Here, assuming equation (6.1) was valid, $G(\omega)$ could be extracted by subtracting G_0 from $G_{tot}(\omega)$, where G_0 was determined from the average of the total conductance in the frequency range of $f \approx 40 - 150$ Hz. If the averaged conductance was negative, G_0 was negligible, and was not subtracted from the total conductance. The negative average conductance may have been caused by the noise-induced fluctuations of the conductance. Fig. 6.4 shows temperature dependence of conductance at various frequencies, where the total conductance and $G(\omega)$ (after subtraction) are plotted. Below 170 K, G_0 was negligible. Thus, $G_{tot}(\omega) \approx G(\omega)$, even at the limit $\omega \to 0$, indicating that the dominant process in the

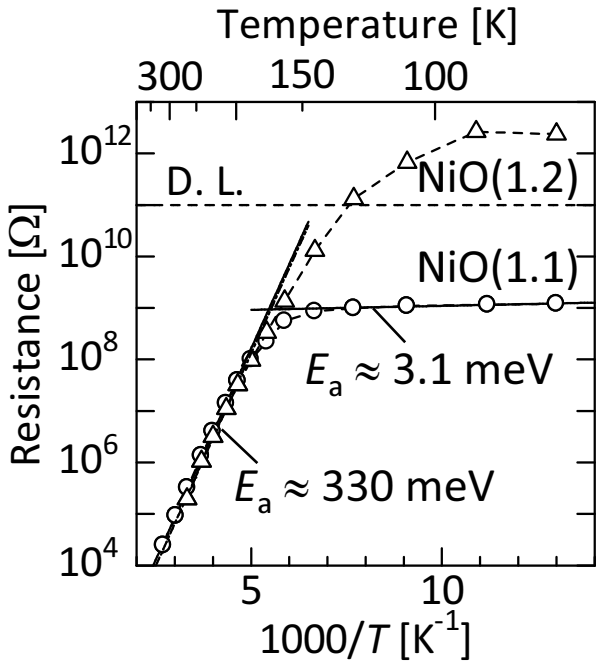

Figure 6.2: Arrhenius plot of RS cells in the initial state with NiO films deposited with O_2 = 1.1 sccm (NiO(1.1)) and 1.2 sccm (NiO(1.2)).

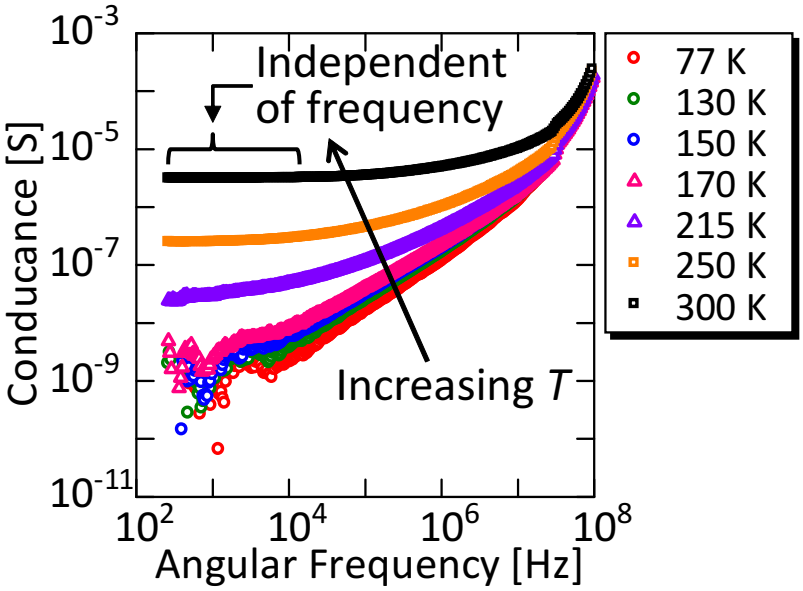

Figure 6.3: AC conductance of an RS cell with NiO(1.1) in the initial state. The conductances is plotted at several temperatures.

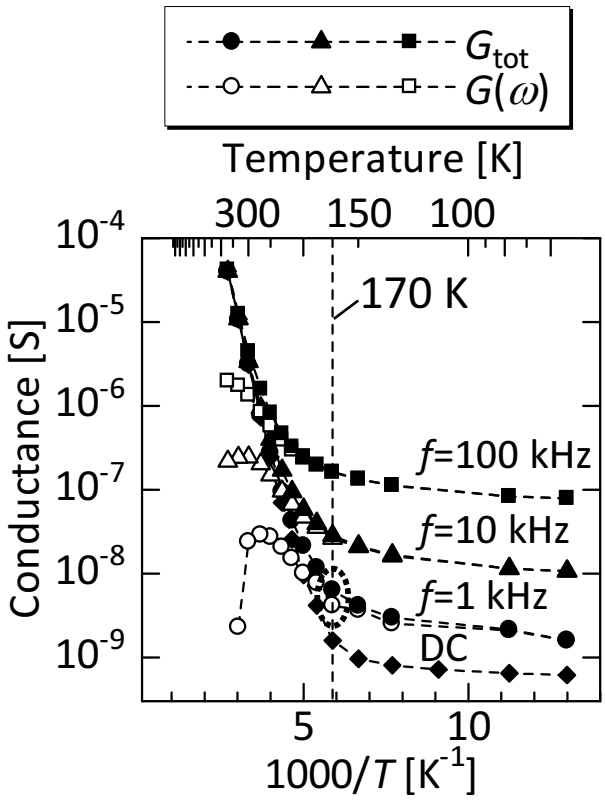

Figure 6.4: Temperature dependence of the conductance at several frequencies. The frequency-dependent component, $G(\omega)$, is also plotted.

DC conduction corresponded to the process responsible for $G(\omega)$. Above 170 K, the frequency-independent component (G_0) increased. Although G_0 was still smaller than $G(\omega)$ at T = 170 K and f = 1 kHz, $G(\omega)$ decreased when the frequency decreased. Thus, G_0 exceeded $G(\omega)$ at the limit $\omega \to 0$ at 170 K and above. To summarize, the conductance at the limit $\omega \to 0$ mainly consisted of $G(\omega)$ below 170 K and G_0 above 170 K.

Considering the DC resistance, the dominant conduction mechanism changed at about 170 K. The E_a of DC resistances was 3.1 meV and 330 meV, below and above 170 K, respectively, as described in Section 6.3.1. Therefore, combining the results of the DC resistance and the AC conductance measurements, the conduction process responsible for $G(\omega)$ was linked to the DC conduction with $E_a \approx 3.1$ meV, while the results for G_0 were linked to the DC conduction with $E_a \approx 330$ meV. This also indicated that $G(\omega)$ and G_0 arose from different conduction processes, validating the application of equation (6.1) for extracting $G(\omega)$ above 170 K.

Next, $G(\omega)$ was obtained by subtracting G_0, as plotted in Fig. 6.5(b). The total conductance before subtraction is shown in Fig. 6.5(a) for comparison. For $T < 250$ K, $\log G(\omega)$ was proportional to $\log \omega$, where $G(\omega)$ can be expressed as:

$$G(\omega) = A'\omega^s \ (s > 0), \tag{6.2}$$

where A' and s are the pre-factor and exponent, respectively. This dependence has been widely observed in chalcogenides [10], amorphous semiconductors [11] and oxides including scandium oxides [12] and NiO [13]. Each curve in Fig. 6.5(b) was fitted by (6.2). When ω was larger than $\sim 10^7$ Hz, $G(\omega)$ was approximately proportional to ω^2 owing to the parasitic impedance originating from the electrodes of the RS cell and the lead lines [11]. Hence, this high-frequency range was excluded from fitting. The fitted curves are also plotted in Fig. 6.5, where s ranged from 0.6 to 0.9. For $T \geq 250$ K, $\log G(\omega)$ was not proportional to $\log \omega$, which originated from the finite carrier relaxation time responsible for the AC conduction and will be described in Section 6.5.

6.4 Conduction in Low- and High-Resistance States

6.4.1 Temperature dependence of the resistance

Figure 6.6 (a) shows the temperature dependence of the DC resistance for RS cells in their the LRS. Two RS cells with different resistances, denoted as LRS-1 and LRS-2, were plotted. The resistances of the LRS-1 and LRS-2 at 300 K were about 30 kΩ and 60 kΩ, respectively. The resistances significantly decreased in both the LRS-1 and LRS-2 above 300 K. The bulk resistance R_{bulk} was either comparable to R_{fil} in the LRS-1 and LRS-2, or even dominant in the LRS-2. Hence, the temperature range ($T \geq 300$ K) was excluded from the analysis. Below 300 K, different temperature dependences were observed depending on the magnitude of R_{LRS}. The resistance in the LRS-1 was almost independent of temperature in the range 77–270 K. That in the LRS-2

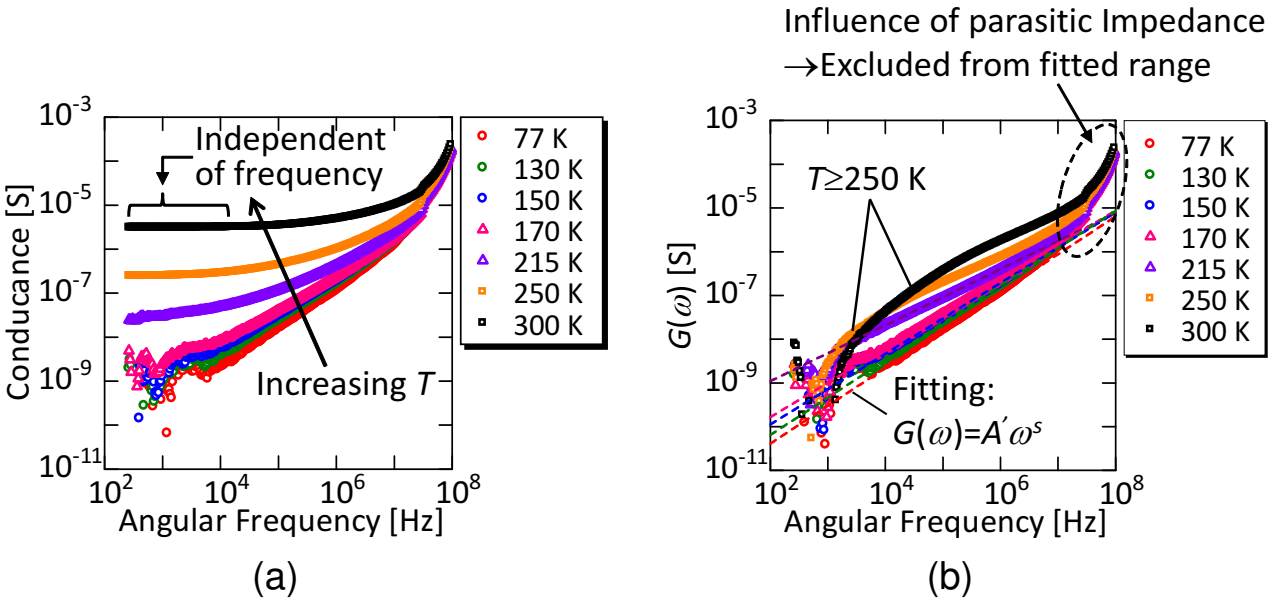

Figure 6.5: (a) AC conductance of an RS cell with NiO(1.1) in the initial state (the same as Fig. 6.3). (b) Frequency-dependent component of the AC conductance, extracted by subtracting the frequency-independent component from the total conductance. Lines fitted by $G(\omega) = A'\omega^s$ are also shown.

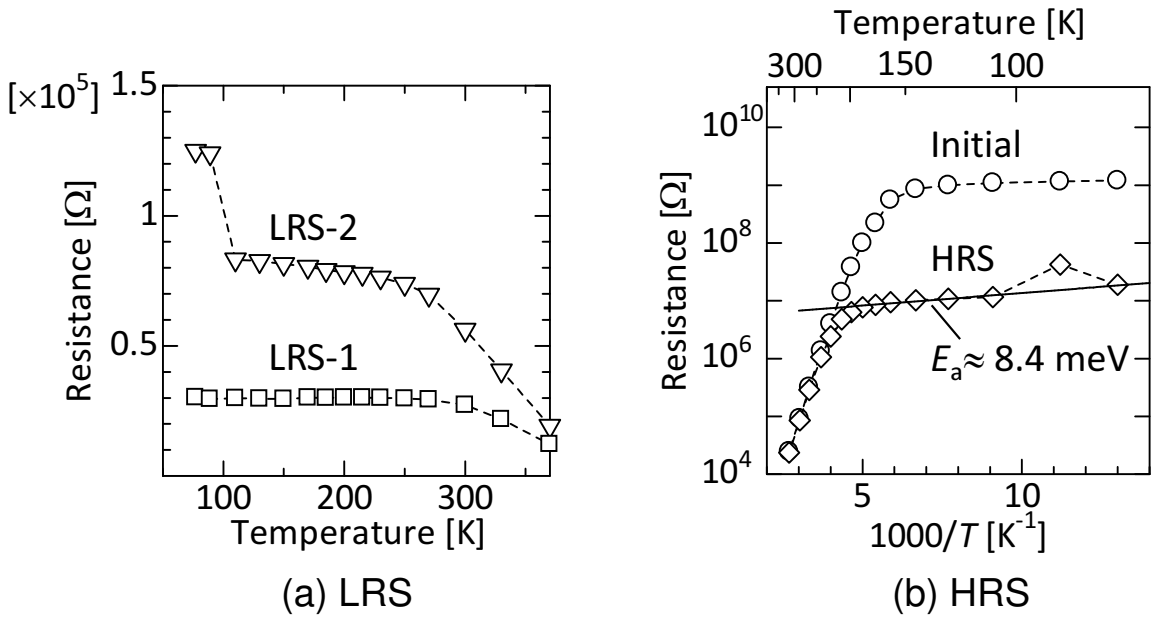

Figure 6.6: Temperature dependence of the resistance in (a) the LRS and (b) the HRS. The resistance in the initial state (NiO(1.1)) is also plotted in (b) for comparison.

exhibited a relatively high resistance, decreasing almost linearly as the temperature increased, exhibiting a negative temperature coefficient of resistance (TCR). The temperature dependence of the resistances in both the LRS-1 and LRS-2 was different from that in the initial state; thus, it was specific to the conduction characteristics of filaments. Besides the LRS-1, when R_{LRS} at 300 K was about 30 kΩ or less, the R_{LRS} was either almost independent of temperature, or exhibited a positive TCR. A negative TCR was observed for 30 kΩ < R_{LRS} < 150 kΩ other than that in the LRS-2. The changes in TCR indicates the conduction characteristics of the filaments changed on the magnitude of R_{LRS}, which is discussed in Section 6.5.3. There was an abrupt decrease in the resistance between 89 K and 110 K in the LRS-2, which was caused by a partial set transition.

Figure 6.6 (b) shows an Arrhenius plot of an RS cell in its HRS. The resistance of an RS cell in the initial state is also plotted for comparison. Above 200 K, the resistance of the RS cells both in their HRS and in their initial state exhibited a similar temperature dependence, and were dominated by R_{bulk}. The HRS exhibited an Arrhenius-type temperature dependence below 200 K with $E_{\mathrm{a}} \approx 8.4$ meV. Although the Arrhenius-type conduction with a low E_{a} at a low temperature was seemingly similar to that in the initial state, the resistance in the HRS was about two orders of magnitude smaller than that of the initial state. Therefore, conduction in the HRS was dominated by a different process than the initial state, and was associated with the resistance of the filament ($R'_{\mathrm{fil}} + R_{\mathrm{rup}}$).

6.4.2 AC conduction characteristics

Figure 6.7 shows the frequency dependence of the conductance in (a) the LRS-2 and (b) the HRS at several temperatures. In both the LRS-2 and the HRS, the conductance increased above about 10^7 Hz, caused by a parasitic impedance. In the LRS-2, as shown in Fig. 6.7 (a), the conductance is almost independent of frequency for $\omega < 10^7$ Hz. This frequency-independent component was linked to DC resistance shown in Fig. 6.6 (a). In a similar manner, most of the conductance in the LRS-1 also consisted of a frequency-independent component (data not shown).

In the HRS, the AC conductance [shown in Fig. 6.7 (b)] mainly consisted of a frequency-independent component in the low-frequency range. It then increased with frequency, similar to that in the initial state [$G(\omega) \propto \omega^s$]. In a similar manner to the initial state, the s values were extracted from the fit after subtraction of the frequency-independent component. The s values ranged from 0.6 to 0.9, being comparable to that in the initial state. The conductance included the conductance of both the bulk and the filament parts, making it difficult to extract the conductance that was intrinsic to the filament. Nevertheless, a significant difference between the HRS and the initial state was observed in the frequency-independent component, G_0. Namely, G_0 was still observed in the HRS even at 77 K, whereas, G_0 was rarely observed below 170 K in the initial state. Therefore, at low temperatures G_0 was linked to the conductance of the filaments ($R'_{\mathrm{fil}} + R_{\mathrm{rup}}$).

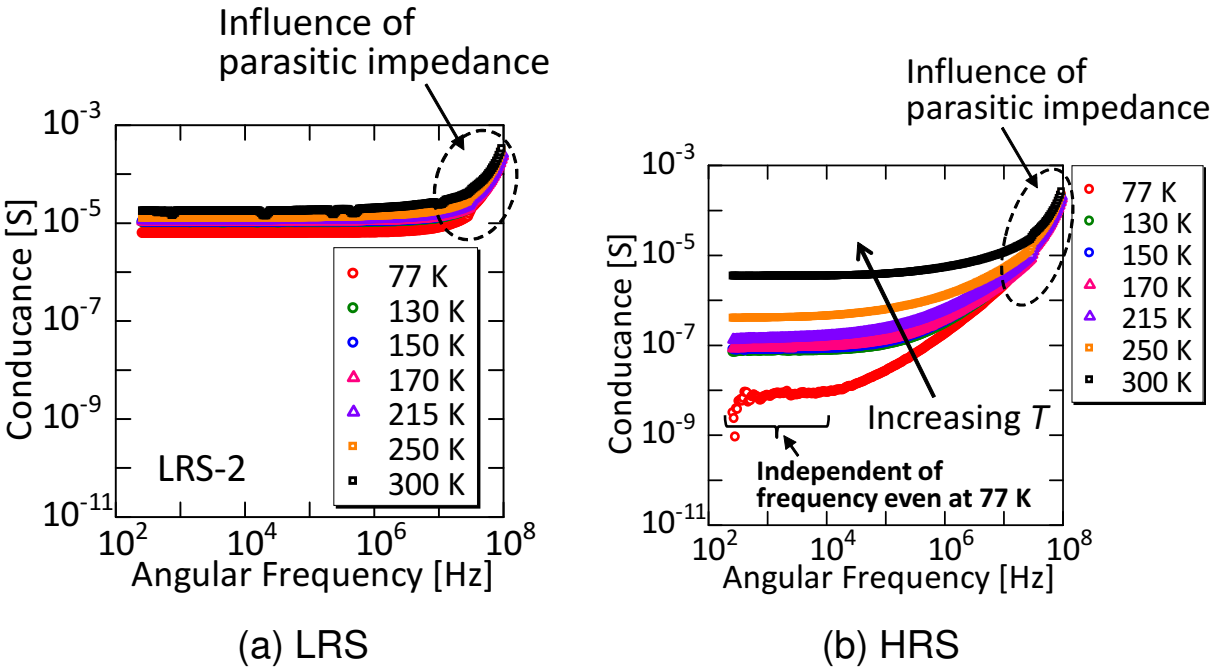

Figure 6.7: AC conductance at different temperatures for (a) the LRS and (b) the HRS.

6.5 Discussion

6.5.1 Models for AC conduction in oxide films

Frequency dependence of AC conductivity in the form:

$$\sigma(\omega) = A\omega^s, \tag{6.3}$$

where s was slightly less than unity, has been observed in amorphous semiconductor and chalcogenides, as described in Section 6.3.2. The origin of the dependence has been ascribed to carrier relaxation between isolated levels as they responded to the applied field. This frequency-dependent behavior was observed in this study. The theoretical treatment for these materials was applied to understand the conduction mechanism in NiO.

According to the treatment, to describe the frequency dependence of the conductivity it was assumed that carrier relaxation occurred between an isolated pair of sites, which is referred to as "pair approximation". This situation is schematically illustrated in Fig. 6.8, where the distance and the energy difference between the site are R_{12} and Δ_{12}, respectively. The expressions are described according to Ref. 11.

The frequency-dependent conductivity is expressed as

$$\sigma(\omega) = \int_0^\infty \bar{\alpha} n(\tau) \frac{\omega^2 \tau}{1 + \omega^2 \tau^2} \, \mathrm{d}\tau, \tag{6.4}$$

where $\bar{\alpha}$ is the polarizability, τ is the relaxation time, and $n(\tau)$ is the density of defects with a relaxation time of τ. For a small electric field, the response was linearized and the polarizability is given by:

$$\bar{\alpha} = \frac{e^2 R_4^2}{12 k_\mathrm{B} T} \frac{1}{\cosh^2 (\Delta_{12}/2k_\mathrm{B}T)} \frac{1}{1 + \mathrm{i}\omega\tau}, \tag{6.5}$$

where the effective relaxation time is given by:

$$\tau = \frac{\tau_0}{2} \left[\cosh \left(\frac{\Delta_{12}}{2k_\mathrm{B}T} \right) \right]^{-1}. \tag{6.6}$$

τ_0 is different among carrier relaxation mechanisms, thus different frequency dependence arises. In this study, three models for the carrier relaxation were considered: tunneling, small-polaron tunneling, and correlated barrier hopping (CBH). τ_0 for these models are described as follows.

For tunneling, τ_0 is given as:

$$\tau_0 = 2\tau_{0\mathrm{t}} \exp(2\alpha R_{12}), \tag{6.7}$$

where α is the decay parameter for the s-like wave functions on the sites. For tunneling, τ_0 varies exponentially with the distance between the sites, R_{12}. For small-polaron tunneling, τ_0 is essentially the same as it is for tunneling, except for an additional component related to the polaron binding energy (W_H). Hence,

$$\tau_0 = 2\tau_{0\mathrm{p}} \exp \left(\frac{W_\mathrm{H}}{k_\mathrm{B}T} \right) \exp(2\alpha R_{12}). \tag{6.8}$$

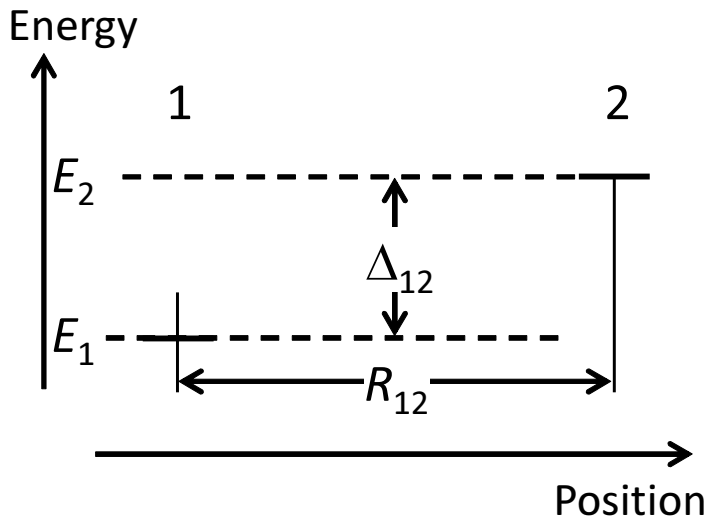

Figure 6.8: A schematic illustration of a pair of sites. [11]

In contrast to the above two models, which are essentially tunneling processes, the CBH is a model for thermally activated hopping over a barrier height (W) between the sites, and τ_0 is described as:

$$\tau_0 = 2\tau_{0\mathrm{h}} \exp\left(\frac{W}{k_\mathrm{B}T}\right), \tag{6.9}$$

where τ_{0i} (i = t, p, h) is on the order of the inverse of the Debye frequency. It is known from equations (6.7)-(6.9), that τ_0 is a function of the distance R_{12} or the barrier height W. In the CBH model, W is also a function of R_{12}, hence τ_0 can be determined by the distance between the sites, even in the CBH model. The frequency exponent (s), introduced in (6.3), is derived from $\partial \ln \sigma / \partial \ln \omega$, and becomes:

$$\text{Tunneling} : s = 1 + \frac{4}{\ln(\omega\tau_{0\mathrm{t}})}, \tag{6.10}$$

$$\text{Small polaron} : s = 1 + \frac{4}{W_\mathrm{H}/k_\mathrm{B}T + \ln(\omega\tau_{0\mathrm{p}})}, \tag{6.11}$$

$$\text{CBH} : s = 1 - \frac{6}{W_\mathrm{M}/k_\mathrm{B}T + \ln(\omega\tau_{0\mathrm{h}})}, \tag{6.12}$$

where W_M is the related the barrier height W, as explained in Section 6.5.2. The frequency-dependent conductivity is described as an imaginary part of the complex capacitance in an equivalent circuit [10, 14]. Therefore, it is proportional to the frequency for $\omega\tau \ll 1$ if τ is constant. The frequency exponent s becomes less than unity because of the distribution of τ, which is dependent on the distance between the sites.

6.5.2 Conduction mechanism in the initial state

As discussed in Section 6.3, different conduction processes were dominant below and above 170 K in the initial state of NiO(1.1). Below 170 K, the DC conduction exhibited an Arrhenius-type temperature dependence with an E_a of 3.1 meV, which was linked to the frequency-dependent component, $G(\omega)$, in the AC conductance. Above 170 K, the DC conduction with an E_a of 330 mV was dominant, which was linked to frequency-independent component G_0.

Below 170 K

Since the conduction process that was dominant below 170 K was linked to $G(\omega)$, the AC conduction characteristics were investigated based on the models described in Section 6.5.1. To examine which model was the most probable, the temperature dependence of the s values was a good criterion. From equations (6.10)-(6.12), it was straightforward to show that s is independent of temperature for tunneling, $\partial s/\partial T > 0$ for small-polaron tunneling, and $\partial s/\partial T < 0$ for CBH, respectively. As shown in Fig. 6.9, s was dependent on temperature. It decreased with temperature, indicating that the CBH model was most probable, which corresponds to a previous study [13].

Here, the CBH model is described in detail. The CBH is a model for carrier relaxation by thermal excitation over the barrier height between a pair of sites, between which the Coulombic

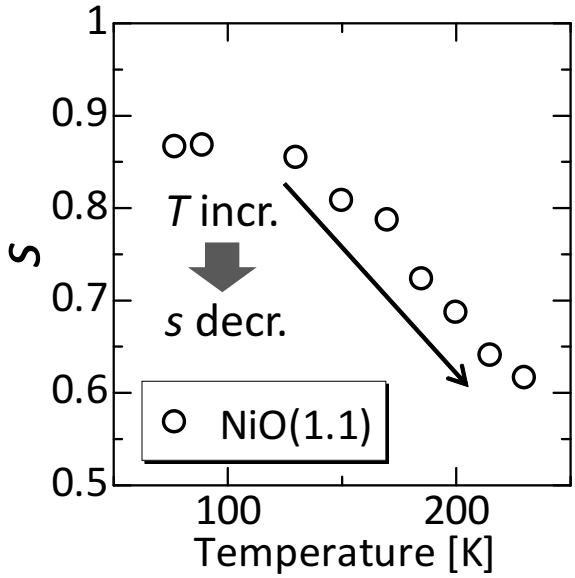

Figure 6.9: Temperature dependence of the s values, the frequency exponent of the AC conductance: $G(\omega) \sim \omega^s$.

forces interact. A schematic illustration of the potential is shown in Fig. 6.10. The barrier height W between a pair of sites separated by the distance R is expressed as

$$W = W_{\mathrm{M}} - \frac{e^2}{\pi\varepsilon\varepsilon_0 R^2}, \tag{6.13}$$

where W_{M} is the ground state energy, and the energy difference between sites (Δ) was assumed to be negligible. The conductivity is given by:

$$\sigma(\omega) = \frac{\pi}{24} N N_{\mathrm{p}} \varepsilon\varepsilon_0 \omega R_\omega^6, \tag{6.14}$$

$$R_\omega = \frac{e^2}{\pi\varepsilon\varepsilon_0 \left[W_{\mathrm{M}} + k_{\mathrm{B}} T \ln(\omega\tau_{0\mathrm{h}})\right]}, \tag{6.15}$$

where N and N_{p} are the densities of the total and occupied sites, respectively [10–12]. s is already given in equation (6.12) as:

$$s = 1 - \frac{6k_{\mathrm{B}}T}{W_{\mathrm{M}} + k_{\mathrm{B}} T \ln(\omega\tau_{0\mathrm{h}})}.$$

Hence, W_{M} was obtained from s using the above equation.

The values of s and A' were obtained by fitting $G(\omega)$ using equation (6.2) (see Fig. 6.5 (b)). A in equation (6.3) was calculated from the relation $A' = AS/t_{\mathrm{NiO}}$ using the cell area, S, and the NiO-film thickness, t_{NiO}. W_{M} was then obtained using a fitted value for s, where τ_{oh} was assumed to be 10^{-12} sec. For ω, an angular frequency corresponding to the median of $\ln\omega$ in the fitted range was adopted. Combining W_{M} and A, NN_{p} was calculated using equation (6.14), where ε is effective dielectric constant estimated from the hydrogen-like energy levels [12]:

$$W_{\mathrm{M}} = \frac{m^* e^4}{2(4\pi\varepsilon\varepsilon_0)^2\hbar^2}. \tag{6.16}$$

The effective mass (m^*) was assumed to be equal to the free electron mass. The density of occupied sites N_{p} must be known to obtain before N can be obtained. Although it was difficult to estimate N_{p}, it was assumed that half of the sites were occupied, namely $N_{\mathrm{p}} = N/2$. N was transformed to R using the relation $N^{-1} = 4/3\pi R^3$, then R was substituted into equation (6.13) to obtain W. The W_{M} and W at the temperatures from 77 to 230 K are tabulated in Table 6.1. Throughout the temperature range, W_M was about 0.4–0.6 eV, while W was negative. The validity of the values obtained and the reason why W was negative will be discussed later in this section. As described in Section 6.3.2, the AC conductance was not proportional to ω^s for $T \geq 250$ K, where fitting was not carried out.

It was discussed that $G(\omega)$ in NiO(1.1) can be described by the CBH model. The DC conduction with low-E_{a} at low temperatures similar to this study, has been reported in lithium (Li)-doped NiO [15, 16]. The mechanism was attributed to impurity hopping via acceptors, Li, compensated by $\mathrm{V_O}$, which generally act as donors in oxides [17]. In this study, nickel vacancies ($\mathrm{V_{Ni}}$) acted as acceptors instead of Li. When $\mathrm{V_O}$ density became higher, more $\mathrm{V_{Ni}}$ was compensated, resulting in a larger density of unoccupied acceptor sites. Therefore, the conductivity may have

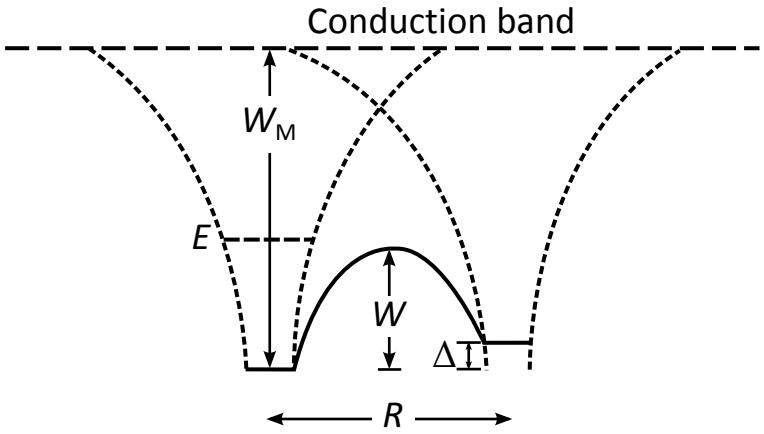

Figure 6.10: Illustration of two Coulombic potentials in the CBH. The potentials are close together, overlapping the potentials and lowering the barrier height. [10]

Table 6.1: Fitted values for s and A and the calculated CBH parameters W_M and W, at each temperature

T [K]	s	A [S/m]	W_M [eV]	W [eV]
77	0.8660	3.47×10^{-11}	0.40	−0.044
89	0.8678	3.54×10^{-11}	0.47	−0.063
130	0.8545	5.77×10^{-11}	0.64	−0.14
150	0.8080	1.25×10^{-10}	0.61	−0.14
170	0.7869	2.02×10^{-10}	0.65	−0.17
185	0.7230	5.65×10^{-10}	0.60	−0.17
200	0.6868	1.13×10^{-9}	0.61	−0.19
215	0.6404	2.63×10^{-9}	0.61	−0.22
230	0.6161	4.80×10^{-9}	0.63	−0.27

been increased with V_O density when the V_O density did not exceed half of the V_{Ni} density. A low-E_a conduction was only observed in NiO(1.1), which may have contained a large number of V_O, supporting that the conduction with E_a = 3.1 meV originated from impurity hopping via compensated V_{Ni}. In addition, AC conductance, $G(\omega)$, which is linked to the DC conduction with E_a = 3.1 meV, has been described by the CBH model. The model is consistent with the impurity hopping mechanism, which also supports the appropriateness of impurity hopping as the dominant conduction process. As a consequence, the conduction below 170 K originated from impurity hopping via V_{Ni} acceptors. This is schematically illustrated in Fig. 6.11.

It is discussed why the CBH parameter W was negative. Taking the above discussion into account, W corresponded to the hopping energy for a hole from an acceptor to another, and may be agree with E_a = 3.1 meV. W_M ranged from 0.4 to 0.6 eV, and the precision of W_M was at most one digit. However, at least three digits of precision are necessary to obtain meaningful values of W from W_M. In addition, several assumptions were involved for obtaining W, such as N_p and $m*$. In consequence, it was difficult to obtain W from W_M with sufficient precision, causing W to become negative.

Above 170 K

For the DC conduction, band conduction or small-polaron hopping (SPH) need to be considered. However, it is unlikely that SPH was responsible for the DC conduction above 170 K, because it should have an effect on the frequency-dependent component of the AC conductance. This was opposite to the results where the process responsible for the DC conduction above 170 K was associated with the frequency-independent component of the AC conductance. In addition, SPH was also excluded from the dominant mechanism for DC conduction near RT and above in Bosman and Crevecoeur's [18]. Hence, band conduction was more likely to occur. The results supporting the above reasoning are described below.

As depicted in Fig. 6.5 (b), $G(\omega)$ was not proportional to ω^s for $T \geq 250$ K. This was because the upper limit of the relaxation time τ was a finite value τ_{max}, while the range for τ was regarded as $0 \sim \infty$ in equation (6.4). Equation (6.4) had the Debye form, $\omega\tau/(1 + \omega^2\tau^2)$. Thus, the contribution from the pairs sites with $\tau \sim \omega^{-1}$ was the most significant contribution. Therefore, as long as $\omega\tau_{max} \gg 1$, τ_{max} may be regarded as infinity. In the case that τ_{max} cannot be considered to be infinity, equation (6.4) includes the form $\omega^2\tau_{max}/(1 + \omega^2\tau_{max}^2)$, and, $\sigma(\omega)/\omega$ has a peak at the angular frequency $\omega_m = \tau_{max}^{-1}$. In the CBH model, τ is described by the equation (6.9). It is clear that τ decreased as temperature increases. Therefore, τ_{max} could not be regarded as infinity for $T \geq 250$ K. As a result, $G(\omega)$ was not proportional to ω^s. Figure 6.12 shows plots of $G(\omega)/\omega$ against ω at temperatures from 250 to 370 K. A conductance peak was clearly observed at each temperature, The peak shifted toward higher frequency as the temperature increased. Since the peak frequency ω_m corresponds to the inverse of τ_{max}, the temperature dependence of ω_m becomes:

$$\omega_m \sim \exp\left(-\frac{W_{max}}{k_B T}\right), \tag{6.17}$$

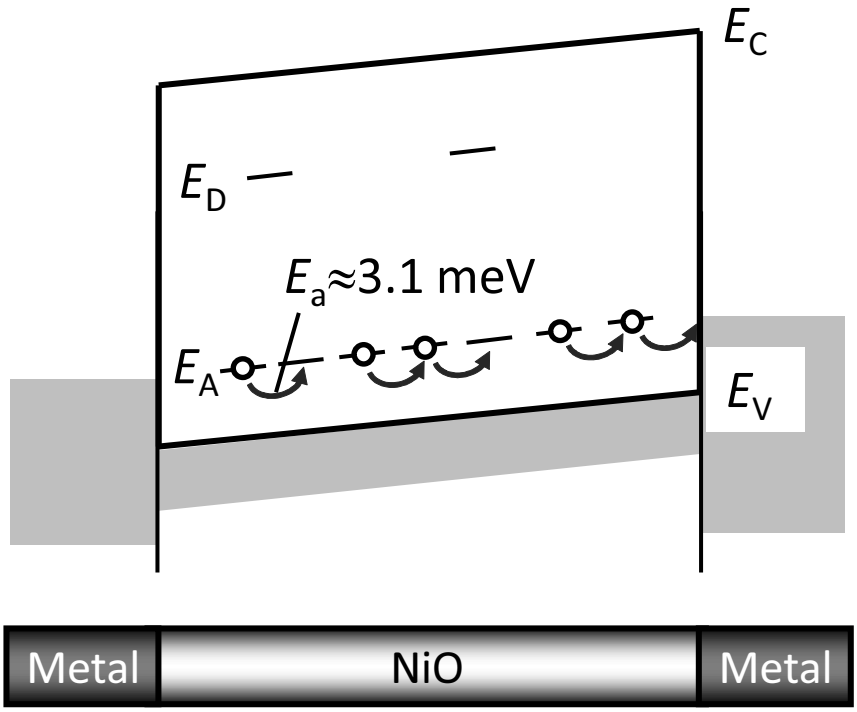

Figure 6.11: Schematic of hopping conduction, which dominated the conduction in the initial state below 170 K.

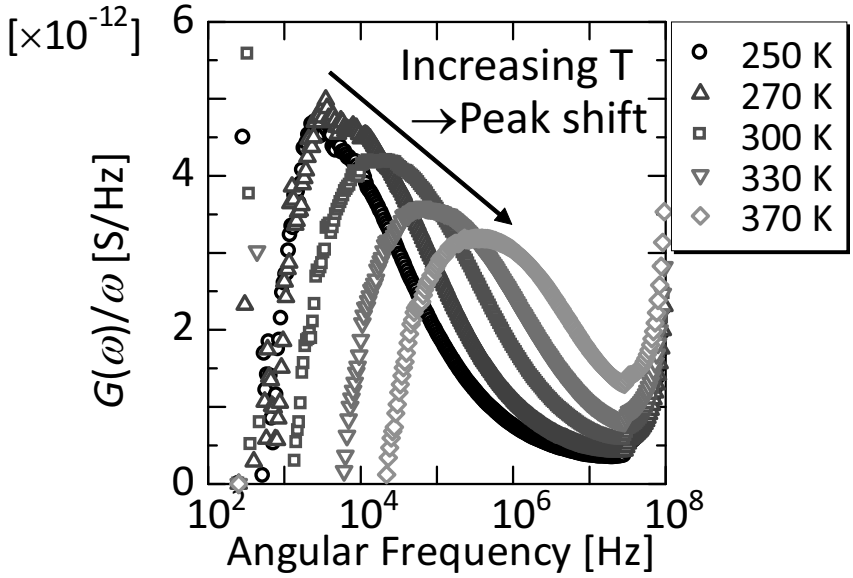

Figure 6.12: $G(\omega)/\omega$ plotted against the angular frequency ω. A conductance peak was observed and the peak frequency shifted toward higher frequencies with an increasing temperature.

where W_{max} corresponds to the maximum barrier height for hopping. From the shift in the peak frequency with temperature, represented in Fig. 6.13, W_{max} was estimated to be about 0.3 eV, which was roughly the same as the E_a for the DC resistance above 170 K.

If the energy for a hole to be excited from an acceptor level or a hole-trap level was ΔE_A, then W_{max} was limited by ΔE_A. This occurred because a carrier contributed to band conduction rather than hopping for a pair of sites with W larger than ΔE_A, as schematically depicted in Fig. 6.14. Therefore, the fact that W_{max} and E_a roughly agreed with each other indicated that E_a corresponded to ΔE_A, and that band conduction was the dominant process for DC conduction above 170 K. The DC conduction above 170 K was linked to the frequency-independent component of the AC conductance, demonstrating that band conduction only contributed to the frequency-independent component of the AC conductance.

6.5.3 Comprehensive explanation on the difference in resistance states

The AC conductance in the LRS mostly consisted of the frequency-independent component at every temperature, as shown in Fig. 6.7 (a). Since the frequency-independent conductance was observed below 170 K, this component did not originate from bulk conductance. Therefore, the conduction in the LRS originated from conduction in the filament R_{fil} [see Fig. 6.1 (a)], consistent with the widely accepted picture of RS phenomenon. Since band conduction contributed to the frequency-independent component, as discussed in Section 6.5.2, conduction in the filaments originated from band conduction, not carrier transfer among the isolated energy levels.

As described in Section 6.4, the DC resistance in the HRS was two orders of magnitude lower than that in the initial state, at low temperatures. The resistance was dominated by $R'_{fil} + R_{rup}$ in the temperature range. In the literature, the conduction in the HRS is believed to be dominated by the filament-ruptured region R_{rup}, which is similar to bulk conduction [7, 9]. Hence, if the conduction in the HRS was determined by R_{rup}, the AC conduction characteristics in the HRS should be similar to the initial state. In this study, conduction in the initial state below 170 K was caused by hopping via V_{Ni}, and the frequency-independent component of the AC conductance was rarely observed. Nevertheless, the frequency-independent component of the AC conductance was observed below 170 K in the HRS. Since the frequency-independence of the AC conductance originated from band conduction, this reflects the conduction characteristics of the filaments in a similar manner to the LRS. Therefore, the conduction in the HRS was dominated by the conduction of the remaining filaments, R'_{fil}, not R_{rup}. To summarize, the transition in the resistance state mainly originated from the change in the conduction characteristics of the filament, not from their rupture and formation. This is an important consequence because it modifies the present description for the mechanism of the changes in the resistance. The discussion above does not exclude the possibility of rupture of the filaments. Instead, it argues that the resistance of the remaining filament, R'_{fil}, was much larger than that of the ruptured part of the filament R_{rup}, and that R_{rup} was negligible. Similar frequency-independent AC conductance of the HRS has been observed in HfO_2-based RS cells [9, 19, 20]. Therefore, the AC conduction characteristics may

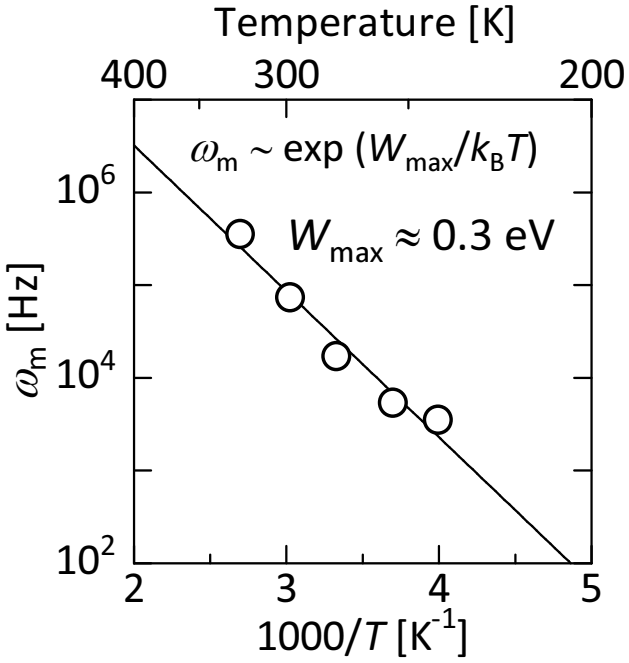

Figure 6.13: Arrhenius plot of ω_m, which is the peak frequency of the $G(\omega)/\omega - \omega$ plot shown in Fig. 6.12.

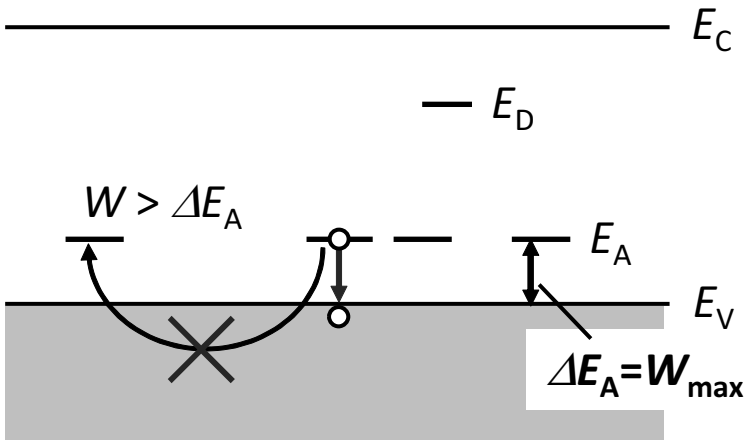

Figure 6.14: Schematic image of excitation of a hole to the valence band. The hole excitation to the band occurs rather than hopping between a pair of acceptor sites if the hopping energy W is larger than the energy for a hole excitation, ΔE_A.

be universal and independent of the RS materials. Nevertheless, a sufficient explanation has not yet been given. This is the first time that it has been suggested that the frequency-independent component originated from the conduction characteristics of the filaments.

Next, it is discussed why the filaments had an activation energy for conduction in the HRS, as shown in Fig. 6.6 (b). A filament can be described as a chain of V_O, which may form a band [21, 22]. The switching mechanism is considered to be partial oxidation and reduction of the filament [23, 24]. Therefore, the reset and set transition may be accompanied by a change in the V_O density, composing a filament as suggested by previous studies [2, 3]. In addition, considering that a filament is generated by the forming similar to oxide breakdown, a generated filament may involve more or less randomness in the spatial distribution of V_O. Taking the knowledge on filaments into consideration, the changes in the conduction characteristics of the filaments have considerable similarities to the impurity band conduction in semiconductors [25, 26]. The change in the conduction characteristics of the filaments can be understood based on the similarities, where the V_O density corresponded to the impurity density in semiconductors. When the V_O density was increased, it formed a band corresponding to a filament. However, because of the randomness in the spatial distribution of V_O, the energy states near the bottom of the conduction band[1] may have been localized, known as Anderson localization [26, 27]. When the V_O density was sufficiently large, the Fermi energy (E_F) was located above mobility edge (E_{cm}) and the filaments exhibited conduction without an activation energy, which may correspond to the LRS-1 and LRS-2. However, when the V_O density of the filaments decreased, E_F was below E_{cm} and most of the carriers were localized. As a result, it was necessary to excite the carriers above E_{cm}, and, the conductivity had an activation energy corresponding to $E_{cm} - E_F$. This situation may correspond to the HRS. Ielmini *et al.* reported that activation energy for the R_{LRS} increased with an increase in the R_{LRS} [6]. The changes in activation energy may have been caused by E_{cm} and E_F, resulting from the change in the V_O density. Therefore, changes in the conduction characteristics between the LRS and the HRS can be understood as the localization and delocalization of the energy levels near E_F, which resulted from changes in the V_O density of the filaments.

The differences in the TCR depending on the R_{LRS} described in Section 6.3.1 may be also explained by the difference in the V_O density of the filaments. The positive TCR observed in the LRS-1 indicates the metallic nature of the delocalized electrons in the filaments [25, 26]. On the other hand, a negative TCR was observed in the LRS-2, the resistance for which was larger than that for the LRS-1. Negative TCR was reported in disordered titanium-aluminum alloys [28]. The negative TCR in the alloys was attributed to the short mean free path of electrons comparable to interatomic distances owing to the random distribution of the elements or amorphous structure [28, 29]. In a similar manner, the negative TCR in the LRS-2 was ascribed to the increase in the randomness of the distribution of V_O owing to the decrease in the V_O density of the filaments. It was also reported that the negative TCR was related to high resistivity of the alloys [28, 30]. This is consistent with the results of this study, where the resistances with negative TCR (30 kΩ < R_{LRS}

[1]The carrier type of the filaments might be the same as that of metallic elements. Hence, it was assumed to be *n*-type. However, this can also holds for *p*-type conduction.

< 150 kΩ) were larger than those with positive TCR ($R_{\mathrm{LRS}} < 30$ kΩ). Therefore, the decrease in the V_O density of the filaments also caused the increase in the resistance of the filaments, even when the electrons near the E_F in the filaments were still delocalized. As a result, the different TCR was observed depending on the magnitude of the R_{LRS} among the RS cells in the LRS.

In conclusion, the conduction in both the LRS and the HRS was dominated by filaments themselves, not by their ruptured region. Therefore, the differences in the resistance between the LRS and the HRS, or even among the LRS, can be understood to be merely relative, originating from the difference in the conduction characteristics of the filaments, which may be attributed to the difference in the V_O density of the filaments.

6.6 Summary

The DC and AC conduction properties of RS cells in each resistance state, including the initial state, were systematically investigated. In the initial state, the DC resistance of the RS cells exhibited an Arrhenius-type temperature dependence near RT, where E_a was about 330 meV. In addition, NiO films containing a large amount of V_O exhibited conduction with a low-E_a of 3.1 meV below 170 K. Combining the analyses for the AC conduction characteristics, it was revealed that the low-E_a conduction originated from hopping conduction via compensated acceptors V_{Ni}. A conductance peak was observed in the $G(\omega)/\omega - \omega$ characteristics at 250 K and above. The activation energy for the peak-frequency shift roughly agreed with the E_a for the DC resistance near RT. Based on these results, it is concluded that band conduction was dominant above 170 K. For the LRS and HRS, the temperature dependence of the DC resistance was different depending on the the magnitude of the resistance. Resistance in the HRS at low temperatures exhibited an Arrhenius-type temperature dependence, while it varied linearly in the LRS. Furthermore, the sign of TCR in the LRS changed from positive to negative one as the R_{LRS} increased. The AC conductance in both states mostly consisted of a frequency-independent component at low frequencies even below 170 K, while the frequency-independent component was rarely observed in the initial state. From the discussion on the AC conductance, it was deduced that the conduction in filaments was dominant in both the LRS and the HRS, This conclusion modifies the previous interpretation on the changes in the resistance states, where conduction in the HRS was limited by the filament-ruptured region. Furthermore, it has been revealed that the difference in the resistance may arose from the difference in the conduction characteristics of the filaments both in the LRS and the HRS. The origin of the difference in the conduction characteristics of the filaments may be explained by the difference in V_O density of the filaments in a similar manner to impurity band conduction in semiconductors.

References

[1] K. Kinoshita, H. Noshiro, C. Yoshida, Y. Sato, M. Aoki, and Y. Sugiyama, J. Mater. Res. **23**, 812 (2008).

[2] H. Akinaga and H. Shima, Proc. IEEE **98**, 2237 (2010).

[3] H.-S. P. Wong, H.-Y. Lee, S. Yu, Y.-S. Chen, Y. Wu, P.-S. Chen, B. Lee, F. T. Chen, and M.-J. Tsai, Proc. IEEE **100**, 1951 (2012).

[4] K. Jung, H. Seo, Y. Kim, H. Im, J. P. Hong, J.-W. Park, and J.-K. Lee, Appl. Phys. Lett. **90**, 052104 (2007).

[5] U. Russo, D. Ielmini, C. Cagli, and A. L. Lacaita, IEEE Trans. Electron Devices **56**, 186 (2009).

[6] D. Ielmini, S. Spiga, F. Nardi, C. Cagli, A. Lamperti, E. Cianci, and M. Fanciulli, J. Appl. Phys. **109**, 034506 (2011).

[7] G. Bersuker, D. C. Gilmer, D. Veksler, P. Kirsch, L. Vandelli, A. Padovani, L. Larcher, K. McKenna, A. Shluger, V. Iglesias, M. Porti, and M. Nafria, J. Appl. Phys. **110**, 124518 (2011).

[8] S. Yu, X. Guan, and H.-S. P. Wong, Appl. Phys. Lett. **99**, 063507 (2011).

[9] S. Yu, R. Jeyasingh, Y. Wu, and H.-S. P. Wong, Appl. Phys. Lett. **99**, 232105 (2011).

[10] S. R. Elliott, Adv. Phys. **36**, 135 (1987).

[11] A. R. Long, Adv. Phys. **31**, 553 (1982).

[12] G. E. Pike, Phys. Rev. B **6**, 1572 (1972).

[13] P. Lunkenheimer, A. Loidl, C. R. Ottermann, and K. Bange, Phys. Rev. B **44**, 5927 (1991).

[14] D. S. Jeong, H. Schroeder, and R. Waser, Appl. Phys. Lett. **89**, 082909 (2006).

[15] A. J. Springthorpe, I. G. Austin, and B. A. Austin, Solid State Commun. **3**, 143 (1965).

[16] I. G. Austin and N. F. Mott, Adv. Phys. **50**, 757 (2001).

[17] P. A. Cox, *Transition Metal Oxides —An introduction to their electronic structure and properties* (Oxford University Press, New York, 2010).

[18] A. J. Bosman and C. Crevecoeur, Phys. Rev. **144**, 763 (1966).

[19] X. A. Tran, H. Y. Yu, Y. C. Yeo, L. Wu, W. J. Liu, Z. R. Wang, Z. Fang, K. L. Pey, X. W. Sun, A. Y. Du, B. Y. Nguyen, and M. F. Li, IEEE Electron Device Lett. **32**, 396 (2011).

[20] Z. Wang, H. Yu, X. A. Tran, Z. Fang, J. Wang, and H. Su, Phys. Rev. B **85**, 195322 (2012).

[21] S.-G. Park, B. Magyari-Köpe, and Y. Nishi, IEEE Electron Device Lett. **32**, 197 (2011).

[22] B. Magyari-Köpe, S. G. Park, H.-D. Lee, and Y. Nishi, J. Mater. Sci. **47**, 7498 (2012).

[23] L. Goux, R. Degraeve, B. Govoreanu, H. Chou, V. V. Afanas'ev, J. Meersschaut, M. Toeller, X. P. Wang, S. Kubicek, and O. Richard, *2011 Symp. on VLSI Technol.* (2011) p. 24.

[24] Y. Sato, K. Kinoshita, M. Aoki, and Y. Sugiyama, Appl. Phys. Lett. **90**, 033503 (2007).

[25] Sir N. Mott, Rev. Mod. Phys. **50**, 203 (1978).

[26] N. Mikoshiba, *Physics of Semiconductors* (Baifukan, Tokyo, 1991), Chapter 12.

[27] Y. Nagaoka, The Nihon Butsuri Gakkaishi **40**, 489 (1985).

[28] J. H. Mooij, Phys. Status Solidi (A) **17**, 521 (1973).

[29] F. J. Ohkawa, J. Phys. Soc. Jpn. **44**, 1112 (1978).

[30] A. K. Sinha, Phys. Rev. B **1**, 4541 (1970).

Chapter 7

Conclusions

7.1 Conclusions

In this study, the mechanism of a resistive switching (RS) phenomenon has been investigated for high-performance resistive random access memory (ReRAM). In particular, this study focused mainly on the properties of conductive filaments including their origin and electrical properties. Influences of the structural properties of nickel oxide (NiO) films on the forming characteristics, namely the initial resistance (R_{Ini}) and the forming voltage (V_{Form}), were also investigated. The main conclusions obtained in this study are summarized as follows.

In Chapter 2, selection of materials for RS cells and the fabrication procedure for the RS cells were presented. From the viewpoint of elucidation of the mechanism of RS phenomenon, NiO and platinum (Pt) were employed as an RS material and an electrode material, respectively. NiO films were deposited by reactive sputtering using a Ni target and the mixture of argon (Ar) and oxygen (O_2) as a process gas. Reactive sputtering using a Ni target allowed us to vary the properties of NiO films systematically, which is beneficial to investigation of the influences of the NiO-film properties on an RS phenomenon. The fabricated RS cells consisted of Pt/NiO/Pt stack structure with diameters ranging from 50 to 300 μm. The thickness of NiO and Pt films was typically 100 nm.

In Chapter 3, the origin of the filaments was investigated from the view point of chemical composition of the NiO films, where heat treatment was employed to alter the NiO-film properties. Dominant factors determining the R_{Ini} were also investigated. After the heat treatment, under which the chemical composition of the NiO films was rarely changed, the R_{Ini} significantly increased with good uniformity among RS cells. The R_{Ini} after the heat treatment was a maximum of 100 MΩ, which was about three orders of magnitude larger than that for the as-deposited RS cells ($R_{\mathrm{Ini}} \approx 3.5$ kΩ). The increase in the R_{Ini} can be attributed to the change in the bulk properties of the NiO films, not a change at the Pt/NiO interface. It was revealed that the R_{Ini} exhibited an Arrhenius-type temperature dependence with the activation energy in the range 250–450 meV, and that the increase in the R_{Ini} was linked to the increase in its activation energy. In contrast, after the heat treatment in vacuum at 300°C, by which oxygen composition of NiO films (x in NiO_x)

was significantly decreased from 0.94 to 0.90, R_{Ini} exhibited large variation among the RS cells, and was even smaller than that for the as-deposited RS cells. The initial state of the RS cells, which exhibited such small R_{Ini}, was equivalent to the low-resistance state (LRS). The RS cells initially in the LRS may result from the formation of filaments by oxygen desorption, indicating that the origin of the filaments may be defects related to oxygen vacancies ($\mathrm{V_O}$).

In Chapter 4, direct observation of conductive filaments were conducted by conductive-atomic force microscopy (C-AFM). It was found that a part of a RS cell in the neighborhood of filaments was deformed during the forming, which enabled to identify the rough location of filaments. The area and current of the filaments were investigated in detail by C-AFM after the removal of a top electrode (TE). There are several kinds of filaments that show a significant difference in current, and the area of the most conductive filaments were of the order of 10^5 nm^2 in the RS cell with R_{LRS} of 10 Ω. By measuring RS cells with various resistances in the LRS (R_{LRS}), it was revealed that the variation in the R_{LRS} in the range 10–220 Ω arose principally from the differences in the size and shape of the filaments. The resistivity of the filaments mainly determining R_{LRS} was estimated to be about 40 $\mu\Omega$cm. From the relationship between the areas of the filaments and the R_{LRS}, the shape of the filaments was also discussed. It was suggested that the area of the filaments can vary along the depth direction depending on their location.

Cross-sectional transmission electron microscopy (XTEM) and energy-dispersive X-ray spectrometry (EDX) analyses were also carried out near a filament that dominantly determines the R_{LRS}. The cross-sectional area of the filament significantly varied along the depth direction, as speculated from the C-AFM analysis. The filaments observed in this chapter consisted of reduced NiO, into which a TE material (Pt) was incorporated. The inclusion of Pt may be caused by Joule heating generated by the current during the forming. The author also pointed out that the suppression of the cell deformation and the larger R_{LRS} are necessary for the detailed investigation of the filaments.

In Chapter 5, influences of microstructure and crystalline properties of NiO films on R_{Ini} and V_{Form} were investigated to reduce V_{Form} while keeping R_{Ini} sufficiently large. First, the substrate temperature (T_{sub}) and the bottom electrodes (BEs) for NiO deposition were optimized, where the T_{sub} of 623 K and the sputter-deposited BEs were employed. After that, various NiO films were prepared by varying the $\mathrm{O_2}$-flow rate in the range 0.9–1.3 sccm during deposition. The resistivity of the NiO films in the initial state determined from the resistance of the RS cells, was about 7×10^5 Ωcm and nearly constant for NiO films deposited with the $\mathrm{O_2}$-flow rate of 1.1 sccm and above. When the $\mathrm{O_2}$-flow rate was 1.0 sccm, the resistivity of NiO films was about 7×10^4 Ωcm, which is one order of magnitude smaller than that with the NiO films deposited with 1.1 sccm. TEM observation revealed that the NiO films were composed of a number of grains a diameter of tens of nm. The TEM observation also clarified that Ni-segregation was formed at grain boundaries (GBs) when NiO films were deposited under the $\mathrm{O_2}$-flow rate of 1.0 sccm, while the NiO grains had O-rich composition. It was demonstrated by C-AFM measurements that the Ni segregation formed at GBs acted as electrical leakage paths in the initial state, giving rise to the decrease in the R_{Ini}.

V_{Form} of the RS cells significantly varied from 2.2 V to 16 V depending on the O_2-flow rate during the NiO deposition, where the minimum V_{Form} of 2.2 V was obtained when the O_2-flow rate was 1.1 sccm. It was revealed that the NiO films had residual compressive stress, and the correlation between the residual compressive stress and the V_{Form} was found. The reason why they are linked to each other was discussed based on lattice defects contained in the NiO films, where the increase in the residual compressive stress was ascribed to the increase in oxygen interstitials (O_i) and the decrease in V_O. The V_{Form} was turned out to be smaller in NiO films containing a larger amount of V_O. The residual stress and the V_{Form} may have been linked to each other via the amount of V_O. Furthermore, the Ni segregation observed in the NiO films deposited under the O_2-deficient condition disappeared after the post-deposition annealing in an Ar atmosphere at 450°C. The RS cells with those annealed-NiO films exhibited forming-free behavior, while the V_{Form} in the RS cells significantly increased when the NiO films without Ni segregation were annealed. The forming-free behavior may be owing to the generation of filaments by the incomplete oxidation of the Ni segregation formed at GBs by excess oxygen inside the NiO grains. The increase in the V_{Form} for the NiO films without Ni segregation after the annealing was inferred to be caused by the decrease in the V_O density by annihilation of the O_i and the V_O during the annealing, which was suggested by stress relaxation by the annealing. It has been concluded from the results that V_O plays an important role in determining the V_{Form}.

As a consequence, RS cells with low V_{Form} (2.2 V) and large R_{Ini} of about 300 kΩ was obtained, when NiO films were deposited with the O_2-flow rate of 1.1 sccm were used. In those RS cells, the R_{LRS} was more than 10 kΩ and the I_{Reset} of about tens of μA. Compared with the RS cells in Chapters 3 and 4, where the V_{Form} of RS cells was about 6 V, the R_{LRS} was more than two orders of magnitude larger and the I_{Reset} was more than two orders of magnitude smaller, demonstrating that the reduction in V_{Form} is effective at reducing the operation current. Furthermore, deformation was not created in the low-V_{Form} RS cells by the forming and the following resistive switching, which allows for the investigation of the properties of the filaments in detail.

In Chapter 6, the DC and AC conduction characteristics of the RS cells in each resistance state including the initial state were investigated. In the initial state, the DC resistance of the RS cells exhibited an Arrhenius-type temperature dependence above 170 K, where the E_a was about 330 meV. In addition, the NiO films containing a large amount of V_O clearly exhibited conduction with a low E_a of 3.1 meV below 170 K. Taking account of the analyses of the AC conductance characteristics, it was revealed that the low-E_a conduction may originate from hopping conduction via compensated acceptors, nickel vacancies (V_{Ni}). The hopping conduction caused the frequency-dependent AC conductance. On the other hand, it has been deduced that conduction above 170 K is dominated by band conduction, which contributed the frequency-independent component in the AC conductance.

Different temperature dependences of the DC resistance were observed depending on the magnitude of the resistance of the RS cells with respect to the LRS and the high-resistance state (HRS). The DC resistance in the LRS varied linearly with temperature. The temperature coefficient of resistance (TCR) was positive when R_{LRS} at room temperature (RT) was $\leq$ 30 kΩ, and negative

when 30 kΩ < R_{LRS} at RT < 150 kΩ. An Arrhenius-type conduction with an E_a of 8.4 meV was observed in the HRS, where the resistance at RT was about 250 kΩ. The AC conductance at low frequencies was almost frequency-independent in both the LRS and the HRS even below 170 K. Since the AC conductance in the initial state was mainly composed of the frequency-dependent component below 170 K, the frequency-independent AC conductance both in the LRS and the HRS can be ascribed to the conduction in the filaments. In addition, the frequency-independent component in the AC conductance indicates that the conduction in the filaments is attributed to band conduction. From these results, it was deduced that conduction in both the LRS and the HRS is dominated by the conduction in the filaments. Furthermore, the different temperature dependences of the DC resistance depending on the resistance of the RS cells may arise from the difference in the conduction characteristics of the filaments. As a consequence, the difference in the resistance of the RS cells between the LRS and the HRS or even among the LRS can be understood to be merely relative, originating from the difference in the conduction characteristics of the filaments. Since it has been considered in previous studies that conduction in HRS is limited by the ruptured part of filaments, where conduction characteristics is similar to that of the initial state, the conclusion in this chapter modifies the previous interpretation on the change in the resistance state. The origin of difference in the conduction characteristics of the filaments may be explained by the difference in the density of V_O composing the filaments in a similar manner to impurity band conduction in semiconductors.

7.2 Future Work

This study focused on the structural and physical properties of the filaments and the influences of the structural properties of NiO films on the V_{Form} and the R_{Ini}. Several issues concerning them have been clarified. In the future, besides the more complete elucidation of the properties of the filaments, investigation on an RS phenomenon from broader viewpoints including the switching speed and the stability of resistance states is necessary. Based on the perspective, the author offers several suggestions for detailed understanding of an RS phenomenon toward the realization of high-performance ReRAM.

Quantification of the density of oxygen vacancies and modeling of a forming process

It was pointed out that V_O plays a key role in the formation of the filaments. On the other hand, the contribution of the V_O to conduction in the initial state was observed as hopping conduction via compensated V_{Ni} at low temperature as described in Chapter 6. Nevertheless, a direct evidence of the existence of V_O is still lacking. Therefore, it is important to verify the existence of V_O by other techniques. Park *et al.* showed by *ab initio* calculation that a single V_O in NiO generates an occupied level at about 1 eV above the top of valence band and two empty levels at about 0.3 eV below the conduction band [1]. Hence, the existence of V_O may be detected by optical emission from the defect levels such as cathodoluminescence (CL) and photoluminescence (PL),

as they suggested. In addition, the quantification of V_O in NiO films is necessary to elucidate the relationship between the V_O density and the V_{Form}. The quantitative relation between the V_O density and V_{Form} can help us establish a new model for V_{Form} or the modification of the present model for the forming [2]. As a result, the quantitative relation can be utilized as a guiding principle to control and prediction of the V_{Form}.

It is necessary that NiO films are prepared with systematically varying V_O density to evaluate the influence of the V_O density on the V_{Form}. This may be achieved by controlling the conditions for NiO deposition or post-deposition annealing. One of the methods to quantify the V_O density is electron-spin resonance (ESR) measurements. ESR can detect spins of unpaired electrons, and has been applied to detect defects in various materials such as SiC [3]. Hence, it may also be possible to detect spins originating from unpaired electrons in NiO. Another candidate is an electrical technique. As described in Chapter 6, the difference in V_O density was observed as hopping conduction at low temperature. Therefore, the conductivity of the hopping conduction might become an useful way to evaluate the V_O density. Combining these measurements may enable to quantify the V_O density.

Influences of the content of pre-existing oxygen vacancies on RS characteristics

It has been suggested that resistance change arises from the change in V_O density composing the filaments. Therefore, it is possible that the density of pre-existing V_O in the initial state also influence RS characteristics such as the switching speed and the data retention. Investigation of the density of the pre-existing V_O on RS characteristics may be an effective approach to determine the density of pre-existing V_O which maximizes the performance RS cells. When the influences of the density of pre-existing V_O on RS characteristics are evaluated, they should be compared among RS cells with similar R_{LRS}. The density of pre-existing V_O also varies the magnitude of the V_{Form}, which can affect R_{LRS} due to current overshooting during the forming, as described in Chapter 5. Therefore, the current overshooting needs to be suppressed by employing an appropriate current limiter during the forming.

Investigation on the properties of filaments in large-R_{LRS} cells

As described in Chapter 5, the reduction in V_{Form} was highly effective in improving RS characteristics, realizing a large R_{LRS} cell. The achieved R_{LRS} is comparable to that in state-of-the-art devices. Structural properties of filaments in the large-R_{LRS} cells such as diameters and shapes can provide important information for the more sophisticated modeling of an RS phenomenon. In addition, clarifying the differences in their shape and chemical composition between LRS and HRS gives us more detailed insights into RS phenomenon.

However, several issues must be solved to investigate the properties of the filaments in large-R_{LRS} cells. Since cell deformation during the forming was suppressed in these RS cells, methods should be established to identify the location of filaments. C-AFM as well as electron-beam-absorption current measurements [4] may be promising tools for the purpose. However, it is

difficult to scan the whole cell area with enough resolution to detect filaments in the RS cell with large area (50 μm in diameter). Therefore, the cell size must be shrunk to about 1×1 μm^2 or below to enable to scan the whole cell area with sufficient resolution. On the other hand, methods for electrode removal should be also established. For this purpose, scratching by AFM probes may be useful [5].

Electrical properties of filaments should be also investigated in more detail to understand conduction mechanism. It was proposed in Chapter 6 that the changes in the conduction characteristics of the filaments originate from Anderson localization. Mott pointed out that electrons under such localization are transferred by variable-range hopping in the limit of low temperature, where the conductivity, σ follows as:

$$\sigma = A \exp\left(-\frac{B}{T^{1/4}}\right), \tag{7.1}$$

while σ approaches so called "minimum metallic conductivity" σ_{min} in the limit of high temperature [6]. Therefore, it may be corroborated whether Anderson localization occurs or not by conductivity measurements in the temperature range broader than that in this study. For the measurements, it is necessary to avoid the influence of R_{Ini} during the measurements. Analyses of the current-voltage (I–V) characteristics of filaments based on the model proposed in this study may also give us further insights into their conduction mechanism.

References

[1] S. Park, H.-S. Ahn, C. Lee, H. Kim, H. Jin, H.-S. Lee, S. Seo, J. Yu, and S. Han, Phys. Rev. B **77**, 134103 (2008).

[2] G. Bersuker, D. C. Gilmer, D. Veksler, P. Kirsch, L. Vandelli, A. Padovani, L. Larcher, K. McKenna, A. Shluger, V. Iglesias, M. Porti, and M. Nafria, J. Appl. Phys. **110**, 124518 (2011).

[3] K. Kawahara, Dr. Thesis, Faculty of Engineering, Kyoto University, Kyoto, 2013.

[4] Z. Wei, T. Takagi, Y. Kanzawa, Y. Katoh, T. Ninomiya, K. Kawai, S. Muraoka, S. Mitani, K. Katayama, S. Fujii, R. Miyanaga, Y. Kawashima, T. Mikawa, K. Shimakawa, and K. Aono, *2011 IEEE Int. Electron Devices Meet.* (2011) p. 31.4.1.

[5] U. Celano, Y. Yin Chen, D. J. Wouters, G. Groeseneken, M. Jurczak, and W. Vandervorst, Appl. Phys. Lett. **102**, 121602 (2013).

[6] Sir N. Mott, Rev. Mod. Phys. **50**, 203 (1978).

Appendix A

Determination of Stress from X-ray Strain in ⟨111⟩-Oriented Polycrystalline Cubic Structure

Relation between stress and strain in ⟨111⟩-oriented cubic structures is derived according to Refs. 1, 2. Here, the case of equi-biaxial stress is considered.

A.1 General Expression of a Relation between Stress and Strain

Transformation of coordinates

Crystal coordinates are transformed from the original X_i to X'_i as shown in Fig. A.1, where X'_3 is preferential orientation (⟨111⟩ in this study). The transformation matrix α_{ij} ($X'_i = \alpha_{ij} X_j$) is:

$$(\alpha_{ij}) = \begin{pmatrix} \cos\chi_1 \cos\chi_2 & \cos\chi_1 \sin\chi_2 & -\sin\chi_1 \\ -\sin\chi_2 & \cos\chi_2 & 0 \\ \sin\chi_1 \cos\chi_2 & \sin\chi_1 \sin\chi_2 & \cos\chi_1 \end{pmatrix}, \tag{A.1}$$

where χ_1 and χ_2 are the angles shown in Fig. A.2.

Figure A.2 shows specimen coordinates (P_i) and laboratory coordinates X'_i taken on the specimen, where P_3 is perpendicular to the film surface. The crystal axis X'_3 is coincident with P_3 axis, and the X'_1 axis is rotated from the P_1 axis by orientation angle β as shown in Fig. A.2. The L_3 axis is the direction along which the strain is measured by X-ray diffraction (XRD). The transformation matrix β_{ij} from X'_j coordinates to P_i is:

$$(\beta_{ij}) = \begin{pmatrix} \cos\beta & \sin\beta & 0 \\ -\sin\beta & \cos\beta & 0 \\ 0 & 0 & 1 \end{pmatrix}. \tag{A.2}$$

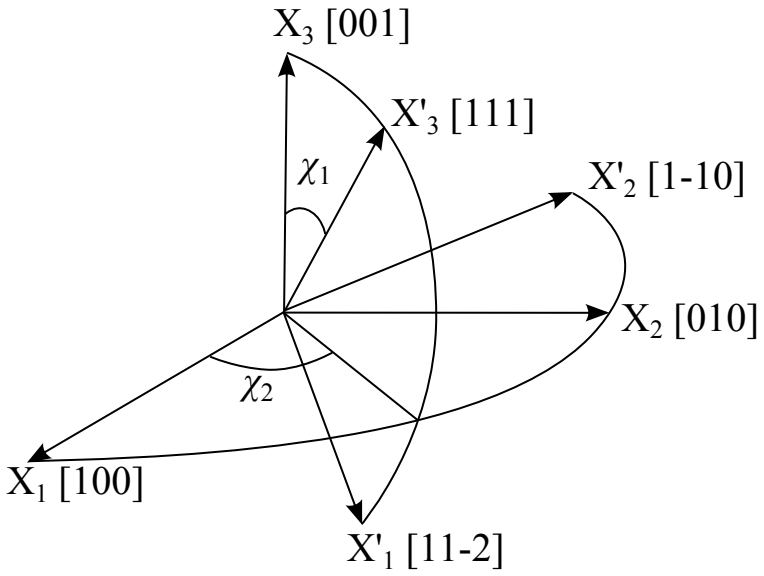

Figure A.1: Transformation of cubic crystal axes.

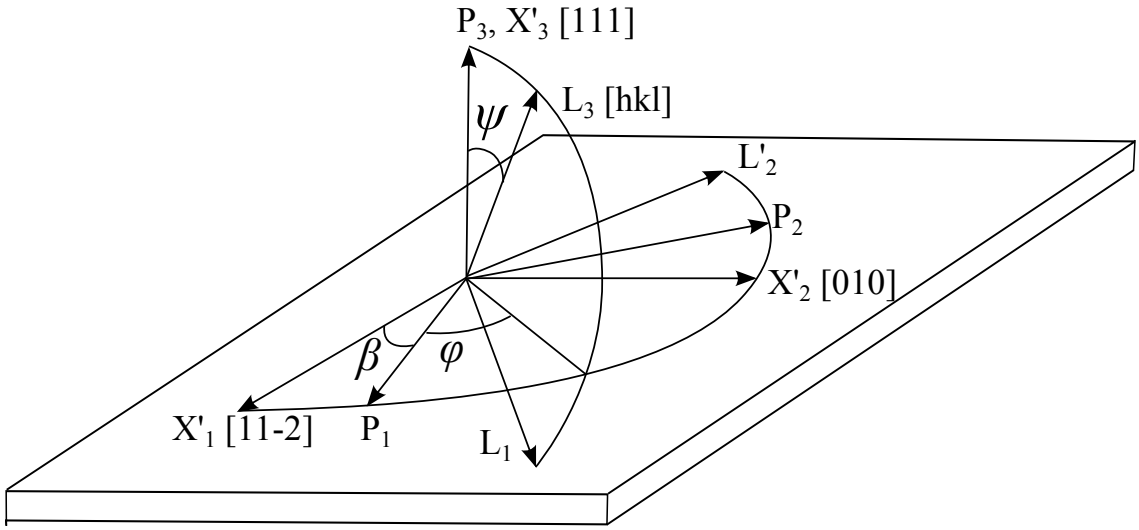

Figure A.2: Coordinated of specimen P_i, laboratory system L_i, and crystal system X_i'.

The angle β indicates the in-plane rotation of crystalline grains. The transformation from X_j to P_i is expressed by the matrix π_{ij}, which is given by the product of β_{ik} and α_{kj} as:

$$\pi_{ij} = \beta_{ik}\alpha_{kj}, \tag{A.3}$$

where repeated indices mean the summation convention from 1 to 3. From Fig. A.2, the transformation matrix from the specimen coordinates P_j from the laboratory coordinates L_i is given by:

$$(\omega_{ij}) = \begin{pmatrix} \cos\psi\cos\phi & \cos\psi\sin\phi & -\sin\psi \\ -\sin\phi & \cos\phi & 0 \\ \sin\psi\cos\phi & \sin\psi\sin\phi & \cos\psi \end{pmatrix}. \tag{A.4}$$

The relation between strain ε_{ij} and stress σ_{ij} of a crystal with orientation β (namely, a crystal rotated by angle β from coordinates X_i) expressed in specimen coordinates P_i is given by:

$$\varepsilon_{ij} = s^P_{ijkl}\sigma_{kl}, \tag{A.5}$$

where s^P_{ijkl} is the elastic compliance of a crystal in specimen coordinates. The compliance s^P_{ijkl} is obtained by tensor transformation from the elastic compliance s_{ijkl} expressed in the original crystal coordinate, namely known values that of single crystal, as follows:

$$s^P_{ijkl} = \pi_{ip}\pi_{jq}\pi_{kr}\pi_{ls}s_{pqrs}. \tag{A.6}$$

Elastic compliance in cubic structures is represented in the following matrix form:

$$(s_{ij}) = \begin{pmatrix} s_{11} & s_{12} & s_{13} & 0 & 0 & 0 \\ s_{12} & s_{22} & s_{13} & 0 & 0 & 0 \\ s_{13} & s_{13} & s_{33} & 0 & 0 & 0 \\ 0 & 0 & 0 & s_{44} & 0 & 0 \\ 0 & 0 & 0 & 0 & s_{44} & 0 \\ 0 & 0 & 0 & 0 & 0 & 2(s_{11}-s_{12}) \end{pmatrix}. \tag{A.7}$$

Note that ε_{ij} and σ_{ij} is the value of one crystal composing a polycrystalline structure. They generally differs among crystals, and thus differed from strain measured by XRD (X-ray strain), which is an average value of crystals satisfying diffraction condition. Hence, appropriate assumptions are necessary to obtain the relationship between stress and X-ray strain. Ruess model and Voigt model are frequently used models, and are explained in the following paragraphs.

Reuss model

In Reuss model, it is assumed that the stress in each crystal σ_{ij} is equivalent to the macrostress $\widetilde{\sigma}_{kl}$: $\sigma_{ij} = \widetilde{\sigma}_{ij}$. The strain in the L_3 direction ε^L_{33} is derived from the strain in specimen coordinate by transforming the coordinate and using (A.5) as:

$$\varepsilon^L_{33} = \omega_{3i}\omega_{3j}\varepsilon_{ij} = \omega_{3i}\omega_{3j}s^P_{ijkl}\sigma_{kl}. \tag{A.8}$$

The strain measured by X-ray diffraction is an average of the strain ε^L_{33} of crystals satisfying diffraction condition, which is expressed as:

$$\overline{\varepsilon}^L_{33} = \omega_{3i}\omega_{3j}\overline{s}^P_{ijkl}\sigma_{kl}. \tag{A.9}$$

Since $\sigma_{ij} = \widetilde{\sigma}_{ij}$, the stress is determined from the measurement of $\overline{\varepsilon}^L_{33}$.

Voigt model

Voigt model assumes that the strain in each crystal is uniform and equal to the macrostrain. The stress in the specimen coordinate is related to the strain by the following equation:

$$\sigma_{ijkl} = c^P_{ijkl}\varepsilon_{kl}, \tag{A.10}$$

where c^P_{ijkl} is elastic stiffness in the specimen coordinate transformed from the crystal elastic stiffness c^P_{ijkl} as:

$$c^P_{ijkl} = \pi_{ip}\pi_{jq}\pi_{kr}\pi_{ls}c_{pqrs}. \tag{A.11}$$

Since ε_{ij} is equal to the macrostrain $\widetilde{\varepsilon}_{ij}$, the stress averaged from $\beta = 0$ to 2π is

$$\widetilde{\sigma}_{ij} = \widetilde{c^P_{ijkl}\varepsilon_{kl}} = \widetilde{c}^P_{ijkl}\varepsilon_{kl}. \tag{A.12}$$

The matrix representation of $\widetilde{c}^P_{ijkl}$ is expressed by:

$$(\widetilde{c}^P_{ij}) = \begin{pmatrix} \widetilde{c}^P_{11} & \widetilde{c}^P_{12} & \widetilde{c}^P_{13} & 0 & 0 & 0 \\ \widetilde{c}^P_{12} & \widetilde{c}^P_{22} & \widetilde{c}^P_{13} & 0 & 0 & 0 \\ \widetilde{c}^P_{13} & \widetilde{c}^P_{13} & \widetilde{c}^P_{33} & 0 & 0 & 0 \\ 0 & 0 & 0 & \widetilde{c}^P_{44} & 0 & 0 \\ 0 & 0 & 0 & 0 & \widetilde{c}^P_{44} & 0 \\ 0 & 0 & 0 & 0 & 0 & (\widetilde{c}^P_{11} - \widetilde{c}^P_{12})/2 \end{pmatrix}. \tag{A.13}$$

The inverse matrix of $(\widetilde{c}^P_{ij})$ is denoted by $(s''_{ij}) = (\widetilde{c}^P_{ij})^{-1}$, which relates the macrostress $\widetilde{\sigma}_{ij}$ to the X-ray strain ε^L_{ij} as:

$$\overline{\varepsilon}^L_{33} = \varepsilon^L_{33} = \omega_{3i}\omega_{3j}s''_{ijkl}\widetilde{\sigma}_{kl}. \tag{A.14}$$

A.2 Relation between Stress and Strain in ⟨111⟩-Oriented Structures

Ruess model

In ⟨111⟩-oriented structures, by substituting $\chi_1 = \cos^{-1}(1/\sqrt{3})$ and $\chi_2 = \pi/4$ into equation (A.1), the transformation matrix (α_{ij}) becomes:

$$(\alpha_{ij}) = \begin{pmatrix} 1/\sqrt{6} & 1/\sqrt{6} & -\sqrt{2/3} \\ -1/\sqrt{2} & 1/\sqrt{2} & 0 \\ 1/\sqrt{3} & 1/\sqrt{3} & 1/\sqrt{3} \end{pmatrix}. \tag{A.15}$$

The strain in a crystal ε_{33}^{L} is written down using equations (A.2), (A.4), (A.6)-(A.8), and (A.15) as:

$$\begin{aligned}\varepsilon_{33}^{L} &= \Big[\frac{1}{4}s_{44}(\sigma_{11}+\sigma_{22}-\sigma_{33}) + \frac{1}{12}(3s_{44}+2s_{s0})\{(\sigma_{11}-\sigma_{22})\cos 2\phi + 2\sigma_{12}\sin 2\phi\} \\ &\quad - \frac{\sqrt{2}}{3}s_0\{\sigma_{31}\cos(2\phi+3\beta) - \sigma_{32}\sin(2\phi+2\beta)\}\Big]\sin^2\psi \\ &\quad + \Big[-\frac{\sqrt{2}}{6}(\sigma_{11}+\sigma_{22})\cos(\phi+3\beta) - 2\sigma_{12}\sin(\phi+3\beta)\} \\ &\quad + \frac{1}{6}(2s_{44}+4s_0)(\sigma_{31}\cos\phi + \sigma_{32}\sin\phi)\Big] \\ &\quad + \frac{1}{3}(3s_{12}+s_0)(\sigma_{11}+\sigma_{22}) + \frac{1}{3}(3s_{11}-2s_0)\sigma_{33}, \end{aligned} \tag{A.16}$$

where s_{ij} is single crystalline elastic compliance, and s_0 is anisotropy index defined by:

$$s_0 = s_{11} - s_{12} - s_{44}/2. \tag{A.17}$$

In the case of the plane and equi-biaxial stress state, *i.e.* $\sigma_{31} = \sigma_{32} = \sigma_{33} = \sigma_{12} = 0$ and $\sigma_{11} = \sigma_{22} = \sigma$, the equation reduces to:

$$\varepsilon_{33}^{L} = \frac{1}{2}s_{44}\sigma\sin^2\psi + \frac{2}{3}(3s_{12}+s_0)\sigma. \tag{A.18}$$

Equation (A.18) indicates that in the case where the stress is in-plane equi-biaxial one, ε_{33}^{L} does not depend on β, and thus is equal to $\overline{\varepsilon}_{33}^{L}$. Therefore, the macrostress can be determined from the linear relationship between $\overline{\varepsilon}_{33}^{L}$ and $\sin^2\psi$.

Voigt model

The elastic stiffness $\widetilde{c}_{ij}^{P}$ is given by:

$$\left.\begin{aligned} &\widetilde{c}_{11}^{P} = c_{11} - c_0/2, \quad \widetilde{c}_{12}^{P} = c_{12} + c_0/2, \quad \widetilde{c}_{13}^{P} = c_{12} - c_0/3 \\ &\widetilde{c}_{33}^{P} = c_{11} - 2c_0/3, \quad \widetilde{c}_{44}^{P} = c_{44} - c_0/3 \end{aligned}\right\} \tag{A.19}$$

where c_{ij} is single crystalline elastic stiffness, and c_0 is anisotropy index defined by:

$$c_0 = c_{11} - c_{12} - 2c_{44}. \tag{A.20}$$

The inverse of the elastic stiffness matrix $(s_{ij}^{''})$ is given by:

$$\left.\begin{aligned} s_{11}^{''} &= \frac{1}{3}s_{11} + \frac{2}{3}s_{12} + \frac{11}{24}s_{44} - \frac{3s_{44}^2}{6(4s_0+3s_{44})} \\ s_{12}^{''} &= \frac{1}{3}s_{11} + \frac{2}{3}s_{12} - \frac{7}{24}s_{44} + \frac{3s_{44}^2}{6(4s_0+3s_{44})} \\ s_{13}^{''} &= s_{12} + \frac{1}{3}s_0, \qquad s_{33}^{''} = s_{11} - \frac{2}{3}s_0 \\ s_{44}^{''} &= \frac{6s_{44}\,(s_{11}-s_{12})}{2s_0+3s_{44}} \end{aligned}\right\} \tag{A.21}$$

The X-ray strain $\overline{\varepsilon}_{33}^{L}$ is related to the macrostress by (A.14) and is independent of angle β. By using elastic compliance $s_{ij}^{''}$, $\overline{\varepsilon}_{33}^{L}$ is written as:

$$\begin{aligned}\overline{\varepsilon}_{33}^{L} &= \left[\frac{1}{2}\left(s_{11}^{''}+s_{12}^{''}-2s_{13}^{''}\right)(\sigma_{11}+\sigma_{22})+\left(s_{13}^{''}-s_{33}^{''}\right)\sigma_{33}\right.\\ &\quad\left.+\frac{1}{2}\left(s_{11}^{''}-s_{22}^{''}\right)\{(\sigma_{11}-\sigma_{22})\cos 2\phi+2\sigma_{12}\sin 2\phi\}\right]\sin^2\psi\\ &\quad+s_{44}^{''}(\sigma_{23}\sin\phi+\sigma_{31}\cos\phi)\sin\psi\cos\psi+s_{13}^{''}(\sigma_{11}+\sigma_{22})+s_{33}^{''}\sigma_{33}, \qquad \text{(A.22)}\end{aligned}$$

where the macrostress $\widetilde{\sigma}_{ij}$ is denoted as σ_{ij} for simplicity. For the in-plane, equi-biaxial stress state, equation (A.22) reduces to:

$$\begin{aligned}\overline{\varepsilon}_{33}^{L} &= \left(s_{11}^{''}+s_{12}^{''}-2s_{13}^{''}\right)\sigma\sin^2\psi+2s_{13}^{''}\sigma\\ &= \frac{1}{2}s_{44}\sigma\sin^2\psi+\frac{2}{3}(3s_{12}+s_0)\,. \qquad \text{(A.23)}\end{aligned}$$

As a consequence, the same expression as equation (A.18) is obtained.

References

[1] K. Tanaka, Y. Akiniwa, T. Ito, and K. Inoue, JSME Int. J. Ser. A **42**, 224 (1999).

[2] K. Tanaka, K. Suzuki, and Y. Akiniwa, *Evaluation of Residual Stresses by X-Ray Diffraction —Fundamentals and Applications—* (Yokendo, Japan, 2006).

List of Publications

A. Full Length Papers and Letters

1. T. Iwata, Y. Nishi, and T. Kimoto
"Effects of Heat Treatment on the Resistive Switching Characteristics of Pt/NiO/Pt Stack Structures,"
Jpn. J. Appl. Phys. **50**, 081102 (2011).

2. T. Iwata, Y. Nishi, and T. Kimoto
"Microscopic Investigation of the Electrical and Structural Properties of Conductive Filaments Formed in Pt/NiO/Pt Resistive Switching Cells,"
Jpn. J. Appl. Phys. **52**, 041801 (2013).

3. T. Iwata, Y. Nishi, and T. Kimoto
"Microstructure and Their Impact on the Electrical Properties of Sputtered NiO Films,"
in preparation.

4. T. Iwata, Y. Nishi, and T. Kimoto
"Conduction Mechanism of NiO-Based Resistive Switching Cells,"
in preparation.

B. Proceedings of International Conference

1. T. Iwata, Y. Nishi, and T. Kimoto
"Identification of the Location of Conductive Filaments Formed in Pt/NiO/Pt Resistive Switching Cells and Investigation on Their Properties,"
Mater. Res. Soc. Symp. Proc. **1430**, 159 (2012).
(*MRS Spring Meeting*, San Francisco, CA, USA, 2012.)

2. T. Iwata, Y. Nishi, and T. Kimoto
"Impact of the Oxygen Amount of an Oxide Layer and Post Annealing on Forming Voltage and Initial Resistance of NiO-based Resistive Switching Cells,"
Mater. Res. Soc. Symp. Proc. **1562** (2013), DOI: 10.1557/opl.2013.719.
(*MRS Spring Meeting*, San Francisco, CA, USA, 2013.)

C. International Conferences

1. T. Iwata, Y. Nishi, and T. Kimoto
   "The Effect of Annealing under Vacuum on the Electrical Characteristics of Pt/NiO/Pt Stack Structures,"
   17th International Workshop on Oxide Electronics, Awaji, Japan, 2010, 20-P-18.

2. T. Iwata, Y. Nishi, and T. Kimoto
   "Identification of the Location of Conductive Filaments Formed in Pt/NiO/Pt Resistive Switching Cells and Investigation on Their Properties,"
   MRS Spring Meeting, San Francisco, CA, USA, 2012, E6.7.

3. T. Iwata, Y. Nishi, and T. Kimoto
   "Impact of the Oxygen Amount of an Oxide Layer and Post Annealing on Forming Voltage and Initial Resistance of NiO-based Resistive Switching Cells,"
   MRS Spring Meeting, San Francisco, CA, USA, 2013, DD14.11.